University of Alberta

Effects of a natural windbreak on dust dispersion in the neutral surface layer

by

Yiwen Mao

A thesis submitted to the Faculty of Graduate Studies and Research
in partial fulfillment of the requirements for the degree of

Master of Science

Department of Earth and Atmospheric Sciences

Spring 2013
Edmonton, Alberta

Abstract

Field experiments were conducted in Indian Head, Saskatchewan in order to study the effects of a natural shelterbelt (width-to-height ratio $W/H = 0.5$) on dust dispersion from a gravel road. Transects of dust concentration sensors running normal to the road were placed both in the lee of the windbreak and in an adjacent unsheltered region. A Lagrangian stochastic (LS) model was developed to compute the theoretical ratio (c/Q) of concentration to emission rate and infer time average concentration ($\overline{c}$) and the ensemble mean concentration transient. In about 69% of cases the inferred time average concentration lay within a factor of two of the corresponding observations (FAC2 = 69%). The modeled and experimental results suggest that the natural windbreak is not effective in filtering small dust particles ($D \leq 20\,\mu$m), but that windbreak entrapment can be a significant mechanism to remove large dust particles ($D \geq 50\,\mu$m).

Acknowledgements

This work was funded by the Agroforesty Developement Centre (ADC) of Agriculture and Agri-Food Canada through the Research Affiliate Program. I'd like to acknowledge comprehensive support from ADC in terms of equipment and personnel. I thank the following ADC employees for their help in conducting the field work: John Kort, Garth Inouye, Chris Stefner, Renee Howard, Jeremy Morris, Kathy Ringdal and Jerry Haid. Both Renee and Jeremy were student interns at the time. Other ADC employees also offered assistance during and after the field experiment. I am grateful to Ms Janet Howden and her husband Mr Don Howden for allowing us to conduct the field experiment on their land, and to cut down a number of trees of their windbreak for the purpose of research. Finally, the work benefited substantially from the advice of Dr. John Wilson of the University of Alberta and Dr. John Kort of ADC.

Contents

List of Tables

List of Figures

Chapter 1

Micrometeorological theory relating to dispersion of road dust

1.1 Research objectives and purpose of this chapter

The objective of this M.Sc. research is to clarify the effectiveness of roadside shelterbelts for the control of rural road dust. This study focused on a specific type of natural windbreak with an aspect ratio (width to height) of 0.5 characterizing the geometric properties of the windbreak and a resistance coefficent of 2.5 characterizing the aerodynamic properties. Field trials undertaken in Indian Head, Saskatchewan employed matching sheltered and unsheltered transects of dust sensors, arrayed perpendicular to a country road; these dust sensors, along with cup anemometers and a sonic anemometer, were operated during periods when a strong wind blew perpendicular to the road. An understanding of shelterbelt efficacy can be sought in terms of differences in the patterns of dust concentration and dust deposition along the sheltered and unsheltered (or “reference”) transects, and to the extent that it is “causal”, must be framed in terms of the micrometeorology affecting those differences. Bearing in mind the complex pattern of wind and turbulence around a shelterbelt, this is a challenging problem. From the theoretical perspective, it is described by a set of coupled partial differential equations that together constitute a numerical model of the active processes. The thesis research compares such a model with the observations, with two main questions in mind: (1) to what extent is the model consistent with the measurements? and (2) what qualitative deductions can be extracted from the available information in its entirety, i.e. the experimental data and the intercomparison with the numerical model?

The purpose of this chapter is to provide some theoretical background to the thesis research. In a broad sense, airborne particulates (i.e. soils, sand, dust particles, pollens, etc.) have been a popular subject of study in atmospheric science. Many experiments have been conducted to study the size distribution of naturally occurring airborne particles, their mechanisms of formation and their life cycle. Loss of immense quantities of soil eroded from farms during dry, windy periods has stimulated much research on soil erosion and means for its control (shelterbelts being one of the methods recommended). In many countries drifting snow is a winter road hazard, and highway fences are commonly utilized to control snow drift. Research on atmospheric particulates also embraces artificial aerosols, e.g. those formed from pollutant gases which result in haze and air quality problems and affect the Earth's radiative energy balance.

Broadly speaking, the processes of aerosol emission and transport are affected by two groups of factors. Firstly, there are the meteorological conditions, viz. not only the wind itself, the agent directly moving the aerosols, but also the temperature distribution, which defines the atmospheric stratification and thus the intensity and scale of turbulent velocity fluctuations, by regulating the vertical dispersion of all admixtures (Oke 1987). Precipitation, should it occur, will cleanse particulates from the air ("scavenging") and by wetting the ground may shut off particulate emission (Oke 1987). The second set of factors characterizes the physical properties of the airborne particles themselves, e.g. particle size and density and shape, and these factors collectively control the gravitational settling of the particles relative to the air.

At a first glance, movements of airborne particles seem to be erratic — this being due to ubiquitous turbulence in the atmospheric boundary layer; furthermore, the issue is more complex in the region close to the ground where obstructions (i.e. windbreaks, buildings, hills, etc.) can influence the wind field around them and thereby alter the trajectories of particles. Particles emitted into the air may eventually be removed from the atmosphere by processes such as gravitational settling, scavenging by precipitation, and surface impaction.

Many attempts have been made to model particle dispersion in the atmosphere along with experimental investigations to provide data for validating models. In this thesis, a few such investigations, namely Bouvet et al. (2006, 2007), Raupach et al. (2001) and Wilson (2000) are introduced in Section 1.5. Essentially, particulates are carried by the host air flow in the atmosphere; thus, understanding the physics of the air movement is a prerequisite to studying the dispersion of airborne substances. In this chapter background theory pertinent to studying the airborne particulates is reviewed. First, some key aspects of atmospheric flow are introduced. Since windbreaks disturb the ambient wind field, it is necessary to study some basic theories pertinent to windbreaks. Fundamentals of atmospheric dispersion are reviewed afterwards. Finally, a brief overview of the project on the topic of studying the effects of a natural windbreak on the dispersion of gravel road dust is given.

1.2 The atmospheric boundary layer

The air flow in the atmosphere acts as a medium to transport airborne particulates, and such transportation is strongly influenced by the interaction between the atmosphere and the Earth's surface. The influence of the Earth's surface is felt most directly in the troposphere (Oke 1987), which is the lowest approximately $10-12\,\mathrm{km}$ of the atmosphere. Over time periods of about one day this influence is limited to a shallower, more intensely mixed layer adjacent to the Earth's surface, known as the atmospheric boundary layer (ABL). Stull (1988) defines the ABL as

"the part of the troposphere that is directly influenced by the presence of the earths surface, and responds to surface forcings with a time scale of about an hour or less".

The vigorous turbulent mixing of the ABL owes to two causes, viz. the vertical shear of the mean wind induced by frictional drag on the uneven, rigid surface of the Earth, and the unstable buoyancy forces that result from the release of thermodynamic energy (sensible and latent heat) at the surface.

The depth (δ) of the ABL is not stationary, because the height of the ABL grows and shrinks on a daily basis in response to the diurnal solar cycle; moreover, δ depends on the strength of turbulence generated near the ground. During daytime the surface of the Earth is heated, and warmer air parcels rise upward to mix with the cooler air parcels throughout the ABL in the presence of buoyancy forces. This type of mixing motion allows the ABL in summer to extend to a depth of about 1 to 2 km by late afternoon. Nocturnally, unless cloud cover prevents the process, the surface of the Earth cools radiatively at a faster rate than the atmosphere, producing a thermal inversion (warm air overlying cold air). Any residual wind transfers heat towards the surface, chilling the ABL. The radiative inversion tends to deepen and strengthen as time progresses overnight, and the resulting stable buoyancy forces tend to suppress turbulent mixing, except in the surface layer where wind shear is strong and continues to supply energy to the motion. For this reason, the ABL shrinks nightly to a shallow depth (δ) of the order of $100 - 300\,\mathrm{m}$.

In this thesis we will be concerned with the motion of dust in the lowest few tens of metres of the ABL, thus it is that layer which is of primary interest.

The atmospheric surface layer

In general, the atmospheric surface layer (ASL) can be defined as a shallow layer adjacent to the ground, having a depth of about $\delta/10$ (its exact depth is not well defined, and not important for present purposes). The ASL is characterized by strong vertical gradients in mean wind speed, mean temperature, mean humidity, etc., because the proximity to the ground limits the efficiency of mixing; moreover, over the depth of the layer the fractional changes in the corresponding vertical fluxes are small relative to their surface values. For example, over a height of about $20\,\mathrm{m}$, the change in the horizontal shearing stress is only about 10% of the surface value. Similarly small changes occur in the mean vertical fluxes of heat and water vapour. For this reason the ASL is often called the “constant flux layer” or “constant stress layer.”

Statistical approach

Due to the ever-present fluctuations of the wind in the ABL and ASL, fluctuations that occur on a wide range of spatial and temporal scales, it is necessary to describe the state (and state of motion) of the atmosphere in terms of *statistics.* There is no sharply optimal choice of averaging time, periods from about 15 to about 60 min being common. The notion is to use an averaging time long enough to capture many "cycles" of even the slowest eddies, without averaging over intervals so long as to entail significant changes in driving boundary conditions, such as solar elevation.

In this thesis I shall assume readers are somewhat conversant with the terminology and conventions relevant to the study of atmospheric turbulence, and give only a very basic review. The term "horizontally-homogeneous" can be applied to any field (i.e. variable) whose statistics are *invariant with respect to position along horizontal planes.* One speaks of a "horizontally-homogeneous flow"
or a "horizontally-homogeneous surface layer", meaning that wind statistics (as well as statistics of the meteorological scalars, such as temperature, humidity, etc.) are independent of the horizontal (x, y) coordinates, whereas generally they must vary with height z. In *fully* homogeneous turbulence, statistics are (by definition) invariant w.r.t. (with respect to) all three spatial coordinates. A second (though less important) term that needs clarification is "stationarity." A system is

"stationary" if its statistics do not change from one averaging interval to the next. In micrometeorological models, terms involving the time rate of change of statistics are commonly neglected – not because they truly vanish, but because they are small relative to other terms.

Terminology with respect to averaging

Let $q = q(x, y, z, t)$ be an arbitrary (instantaneous, local) variable. In the analysis of turbulence the universal approach is to decompose the instantaneous value into the sum of an average and a deviation from average, viz.

$$q = \overline{q} + q' \ , \tag{1.1}$$

where in this thesis the overbar notation will be used for the mean (common alternatives are the angle bracket $\langle q \rangle$ or the upper case Q). The average could in principle be a spatial average or a time average, or even an ensemble average[*]. Unless otherwise stated, in this thesis measured averages are time averages.

Now let "q" be the longitudinal component u of the wind vector $\mathbf{u} \equiv (u, v, w)$. In general the mean velocity can be expressed as $\overline{u} = \overline{u}(x, y, z, t)$, but in a stationary, horizontally-homogeneous ASL we have the much simpler situation that $\overline{u} = \overline{u}(z)$, i.e. the mean wind can be described by a "wind profile". Some common types of anemometers

---

[*] An ensemble average, for which we will use the angle bracket, is defined as the average over an ensemble of possible physical states, such as downwind dispersion of dust particles stemming from one vehicle pass along a gravel road for field trails in Indian Head.

measure the "cup" wind speed, i.e. the mean value of the horizontal wind speed $s = \sqrt{u^2 + v^2}$.

A useful characterization of a turbulent system demands more than merely the prescription of average wind speed. Next in importance are standard deviations, such as $\sigma_u \equiv \sqrt{\overline{u'^2}}$ or (more generally) covariances such as $\overline{u'u'}$ ($\equiv \sigma_u^2$) or $\overline{u'w'}$ or $\overline{w'T'}$. The latter, the covariance of vertical velocity fluctuations and temperature fluctuations, is named the "kinematic heat flux" and is closely related to the sensible heat flux density

$$Q_H = \rho c_p \overline{w'T'} \ , \tag{1.2}$$

where ρ is average air density and $c_p (\approx 10^3\,\mathrm{J\,kg^{-1}\,K^{-1}})$ is the specific heat of air at constant pressure (the units of Q_H are $\mathrm{J\,m^{-2}\,s^{-1}}$, i.e. $\mathrm{W\,m^{-2}}$). Technically (and pedantically) speaking, Q_H is the mean vertical convective eddy flux density of sensible heat, but in the context of the ASL (and particularly the horizontally-homogeneous ASL, for which it is a useful shorthand to introduce the symbol hh_ASL) one can simply say: "heat flux" or "heat flux density" (i.e. one drops some of the clarifying adjectives). One final velocity statistic that will be mentioned later in the thesis is the "turbulent kinetic energy" (TKE), defined as half the sum of the variances of the three velocity fluctuations, viz.

$$k = \frac{\sigma_u^2 + \sigma_v^2 + \sigma_w^2}{2} \ . \tag{1.3}$$

This is simply the average value of the instantaneous kinetic energy of the velocity fluctuation (Stull 1988)

$$e = \frac{1}{2}\left(u'^2 + v'^2 + w'^2\right) \; . \tag{1.4}$$

The TKE is a convenient diagnostic for the intensity of the turbulent fluctuations, and is governed by a well known equation (that will not be elaborated here). Note that $\sqrt{k}$ has velocity units, so may serve as a "turbulent velocity scale" (c.f. u_* defined below). It is also convenient to think in terms of a length scale of the turbulent eddies, such that the turbulence can be characterized by its velocity and length scales, from whose ratio one may form a time scale.

From here on, any unusual symbols will be named where they first occur; otherwise, appeal to a standard textbook may be helpful. Useful textbooks include *Turbulence in the Atmosphere* by Wyngaard (2010), *Atmospheric Boundary Layer Flows* by Kaimal & Finnigan (1994), *The Atmospheric Boundary Layer* by Garratt (1992), and *An Introduction to Boundary Layer Meteorology* by Stull (1988).

Monin-Obukhov theory for the horizontally homogeneous ASL

Over a sufficiently uniform surface and in the absence of any obstacles to the wind, it is plausible to regard the ASL as being horizontally homogeneous, that is, horizontal gradients of most statistics vanish[†]. More broadly, even within a horizontally-homogeneous surface layer flow there may occur some species that had been introduced,

---

[†] An exception is the mean pressure, which varies with x, y in accordance with synoptic scale weather patterns and ultimately drives the winds.

e.g. from point or line or localized area sources, and whose statistics (e.g. mean concentrations) *cannot* be horizontally-homogeneous. The specific example most relevant to this thesis is that of the dust concentration downwind of a gravel road — although in the absence of nearby windbreaks the flow itself may be horizontally homogeneous, the fact that the dust rises off a road means that the dust distribution is spatially non-uniform, or more technically and precisely speaking, is horizontally-*in*homogeneous.

Now consider a horizontally homogeneous ASL, within which (as noted earlier) the vertical fluxes of momentum, heat, water vapour etc. can be regarded as being constant (i.e. height independent). Monin & Obukhov (1954) developed a similarity theory (MOST), applicable in a layer whose base is sufficiently far above ground and whose top is sufficiently small w.r.t. the depth of the ABL that the flow within it is insensitive both to the specific distribution of surface roughness elements, and to the nature of the flow above it. The basis of MOST is the hypothesis that within the layer ($z_0 \ll z \ll \delta$) the distribution of any transferable property (e.g. momentum, heat, and vapor) is horizontally homogeneous in space and stationary in time. It is assumed, more specifically, that within this layer the regime of flow (statistics of wind, turbulence, humdity etc.) is governed by the following parameters:

- the kinematic vertical heat flux traversing the surface layer $\overline{w'T'} = Q_H/(\rho c_p)$ (this is positive for unstable stratification, and negative for stable stratification)

- the kinematic momentum flux u_*^2 traversing the surface layer. Here u_* is the “friction velocity,” sometimes defined ${u_*}^2 = -\overline{u'w'}$ (which assumes axes chosen to ensure $\bar{v} = 0$) but more generally defined as
$${u_*}^4 = \sqrt{\overline{u'w'}^2 + \overline{v'w'}^2}\ . \tag{1.5}$$
Note that the covariance $\overline{u'w'}$ is normally negative in the ASL (positive u' fluctuations correlate with downdrafts), but the friction velocity u_* is positive. The quantity $\tau = \rho u_*^2$ is the mean shearing stress of the wind upon the underlying surface.

- a buoyancy parameter g/T_0, where T_0 is the mean temperature of the layer in Kelvin units

From the above suppositions, a simple dimensional analysis leads to numerous useful predictions regarding surface layer statistics, including a flux/gradient relation. Again let q be some component of the atmosphere and $\overline{q}$ its mean value. Then the flux-gradient relationship may be expressed in the following (general) form:

$$\frac{\partial \overline{q}}{\partial z} = \frac{q_*}{k_v z} \phi_q(\frac{z}{L})\ , \tag{1.6}$$

where q_* is a “scale” for fluctuations and gradients in q, defined $q_* = -F_q/u_*$ where F_q is the vertical flux of q (i.e. rate of vertical transfer per unit horizontal area).

One similarly defines a temperature scale $T_* = -\frac{Q_H}{\rho c_p u_*}$, and the flux/gradient relations for horizontal wind speed and temperature can be written:

$$\frac{k_v z}{u_*}\frac{\partial \overline{u}}{\partial z} = \phi_m(\frac{z}{L}) \ , \tag{1.7}$$

$$\frac{k_{vh} z}{T_*}\frac{\partial \overline{T}}{\partial z} = \phi_h(\frac{z}{L}) \ . \tag{1.8}$$

In these equations L denotes the Obukhov length

$$L = \frac{-{u_*}^3}{k_v \frac{g}{T_0}\frac{Q_H}{\rho_0 c_p}} \ , \tag{1.9}$$

which serves (in the ratio z/L, i.e. the argument of the dimensionless empirical functions ϕ_m, ϕ_h) to characterize the effects on the ASL of thermal stratification. Regarding the formulation of L, recall that turbulence is sustained by horizontal wind shear and by unstable thermal buoyancy forces. Suppose that winds are relatively light, which means that u_* is rather small. From the definition of the Obukhov length, we see that a large upward transport of heat ($Q_H > 0$, unstable atmosphere) results in a small and negative value of L; on the other hand, in a stable atmosphere with downward transport of heat, the formula gives a small and *positive* value of L. If, however, winds are strong, the factor u_*^3 will dominate, and $|L|$ becomes large. Indeed $|L| \to \infty$ defines a *neutrally-stratified* atmospheric surface layer. In addition, the meaning of L can be viewed in this way; below the height $z = |L|$ mechanical production of turbulence is dominant over buoyant production or destruction of turbulence, while above that height the opposite is true. Thus, z/L is a dimensionless stability parameter important in determining the transportation of airborne particles in the surface layer.

But what is the objective of covering this theory? In any application of meteorological knowledge to the transport and dispersion of aerosols, progress can be made only if one has a quantitative formulation of laws for the mean wind profile, and for statistics of wind variability. MOST provides those laws. Of course, to have specific predictions we need to know the universal functions ϕ_m and ϕ_h. These have been the subject (over the past three decades) of several micrometeorological "flux-gradient" experiments, e.g. the Kansas experiment (Businger et al. 1971) and the International Turbulence Comparison Experiment (Francey & Garratt, 1981; Dyer & Bradley, 1982), with the result that formulae approximating the universal functions of the MOST are available. Given instrumentation able to supply measured values of the friction velocity u_* and the sensible heat flux Q_H (a sonic anemometer being the most convenient option) we may compute the statistics of the wind not only at the location of that instrument, but (by extrapolation using the MOST formulae) at all other heights. The MO theory is well tested, and considered very reliable.

The horizontally inhomogeneous ASL

In the real world it is rare to encounter a surface that can be described as flat and uniform over a vast area. The Earth's surface is a patchwork of surfaces with different physical properties (Oke 1987). For example, a pond could be located just in the middle of a bare agricultural field, and one may see a hill not too far away from the field. In this case the basic prerequisite for validity of MOST, namely existence of a horizontally homogeneous ASL, no longer holds because *horizontal gradients* of property statistics (including the mean fields) are generated, by inhomogeneity in the surface boundary conditions and/or by aerodynamic disturbances. A more complex theory or model is required, if one is to be able to prescribe the fields of property statistics (including mean wind speed) in a horizontally *in*homogeneous ASL. Examples below illustrate the theoretical approach for description of horizontally-inhomogeneous (i.e. "disturbed") ASL winds.

Example: local advection Suppose the surface layer winds blow across a uniform upstream surface onto a different downstream surface: a case of what is called "local advection." Let the boundary between the upstream and downstream surfaces lie along the y axis, at $x = 0$. Over the upstream surface ($x < 0$), not too close to the step change at $x = 0$, MOST applies by definition, but for $x > 0$ (i.e downstream) MOST does not apply. Therefore, the fields of mean horizontal wind velocity $\overline{u}(x, z)$, of mean temperature $\overline{T}(x, z)$ and of mean humidity $\overline{q}(x, z)$ are *not in equilibrium* with the corresponding downstream surface fluxes, which vary with height over the downwind region although constrained at the ground by the surface energy balance,

$$Q^* = Q_H(x,0) + Q_E(x,0) + Q_G + \Delta Q_s \ . \tag{1.10}$$

Here Q^* is the net radiation; (Q_H, Q_E) are the sensible and latent heat flux densities; ΔQ_s represents heat storage in the air or vegetation, and Q_G is the flux of heat to or from the soil substrate. Any of the terms can have either sign, but on a sunny summer afternoon over a moist surface all will be positive.

If meteorology is to have any predictive power to forecast "weather" on this micro-scale, one must progress from qualitative statements like those above, to a mathematical theory. A theory, albeit approximate, does exist, and it stems from the conservation equations for the set of coupled variables (velocity components u, v, w plus temperature and humidity). By applying a formal averaging operation to those equations one may derive the Reynolds equations, an example of which is

$$\frac{\partial \overline{u}}{\partial t} + \overline{u}\frac{\partial \overline{u}}{\partial x} + \overline{v}\frac{\partial \overline{u}}{\partial y} + \overline{w}\frac{\partial \overline{u}}{\partial z} = -\frac{1}{\rho}\frac{\partial \overline{p}}{\partial x} - \frac{\partial \overline{u'u'}}{\partial x} - \frac{\partial \overline{u'v'}}{\partial y} - \frac{\partial \overline{u'w'}}{\partial z} \ . \tag{1.11}$$

Simplifications may apply (e.g. in steady state flow the $\partial/\partial t$ term vanishes; and $\overline{v} = 0$ if the mean wind is perpendicular to the boundary between the two surfaces considered above). However a key point to make here is that the equation "for $\overline{u}$" has turned out to involve higher order statistics (the turbulence covariances on the right hand side). This is the "turbulence closure problem", and it demands that one introduce some supplementary empirical information (equations) to close the problem mathematically. One of the most influential models (Rao et al. 1974) for solving the problem of local advection was based on numerical simulation of the RANS (Reynolds-averaged Navier-Stokes) equations using second order closure. The Rao et al. model consists of 16 coupled partial differential equations, governing all first- and second-order statistical properties of the flow. Eq. 1.11 is (of course) one of those equations, and it is worth remarking that the disturbance to the longitudinal velocity component $\overline{u}$ is coupled with a pressure disturbance, and gradients in components of the Reynolds stress tensor.

Example: Aerodynamic disturbances Besides being caused by boundary-generated inhomogeneities, horizontal gradients of mean properties in the ASL can also be generated by aerodynamic disturbances. Common examples are the disturbance of the wind flow by hills, fences, shelterbelts and so on. Whereas boundary-generated disturbances “diffuse” into the airflow and generate a slowly deepening “internal boundary layer,” aerodynamic disturbances can be more abrupt. That this is so is implied by the equation governing the field of the mean pressure disturbance,

$$\frac{1}{\rho_0}\nabla^2\overline{p} = -\frac{\partial\overline{u_i}}{\partial x_j}\frac{\partial\overline{u_j}}{\partial x_i} - \overline{\frac{\partial u_i'}{\partial x_j}\frac{\partial u_j'}{\partial x_i}} - \frac{g}{T_0}\frac{\partial\overline{T}}{\partial z}\ . \tag{1.12}$$

This equation, which is obtained by differentiating and combining the Reynolds equations for the velocity components, shows that the mean pressure field, which exerts (or can exert) a huge influence on the mean velocity field, responds to gradients in mean velocity and in the velocity fluctuation at *all* points in space. When surface layer winds are disturbed by a windbreak, the disturbed pressure across the windbreak exerts an influence on the location of the point of minimum mean wind speed reduction (point of best shelter), on the mean streamline curvature, the speed-up zone over the top of the windbreak, and the rate of leeward recovery of the wind speed.

Having discussed disturbed flows in the abstract sense, some elements of windbreak flows will be reviewed in the next section.

1.3 Windbreak effects

1.3.1 Effects on wind and turbulence

Windbreaks have been used for centuries to provide shelter or to alter microclimate conditions (i.e temperature, humidity, evaporation, etc.) in the downwind region. A natural windbreak (or shelterbelt) is a plantation, usually comprising one or more rows of trees, to provide a shelter from the wind in its immediate lee. From field experiments and numerical modeling, it has been shown that, downwind of a windbreak, there exists a triangular ground-based "quiet zone," wherein both the mean wind speed and the turbulent kinetic energy are reduced relative to their values at the same height upwind of the shelter. There is evidence to show that eddy diffusivities for turbulent transport of heat, vapor and carbon dioxide are also reduced in the quiet zone (Mc-

Naughton 1988). Above the quiet zone, whose downwind apex contacts the ground at about $8 - 10H$ downwind from the shelter, there lies a jet region where mean wind speed is increased (due to the compression of streamlines lifted over the barrier); and finally, downstream of the quiet zone one finds an extended wake region where flow properties are gradually restored to their original (upwind) levels.

Parameterization of windbreak drag in equations of motion Most theoretical descriptions of shelterbelt flows do not resolve the detailed flow about branches, leaves and trunks, but rather, they treat the obstacle as a sink for streamwise momentum (e.g. Wilson 1985; Wang et al. 2001). The following equations follow Wilson's (1985) approach. The earlier Equation.(1.11), i.e the Reynolds equation for $\overline{u}$, is modified to

$$\overline{u}\frac{\partial \overline{u}}{\partial x} + \overline{w}\frac{\partial \overline{u}}{\partial z} = -\frac{1}{\rho}\frac{\partial \overline{p}}{\partial x} - \frac{\partial \overline{u'u'}}{\partial x} - \frac{\partial \overline{u'w'}}{\partial z} - S_u \tag{1.13}$$

where stationarity and symmetry along the y axis have been supposed. For a natural windbreak the momentum sink takes the form

$$S_u = -\,C_d\,\alpha\,\overline{u}\,\sqrt{\overline{u}^2 + \overline{v}^2 + \overline{w}^2} \approx C_d\,\alpha\,\overline{u}\,|\overline{u}| \tag{1.14}$$

where $C_d = C_d(x, z)$ is the drag coefficient and $\alpha = \alpha(x, z)$ is the (spatially-varying) plant area density (vanishing outside the boundaries of the shelterbelt). Some types of windbreaks can be represented as a thin porous barrier ("fence") and can be characterized by a dimensionless resistance coefficient k_r (Laws & Livesey, 1978) such that

$$S_u = -\,k_r\,\overline{u}\,\sqrt{\overline{u}^2+\overline{v}^2+\overline{w}^2}\;\delta(x{-}0)\,s(z{-}H)\;\approx k_r\,\overline{u}\,|\overline{u}|\,\delta(x{-}0)\,s(z{-}H)\;, \tag{1.15}$$

where $\delta(x-0)$ localizes the barrier to $x = 0$ and the step function $s(z{-}H) = 1$ at $z \leq H$ and vanishes at $z > H$. The resistance coefficient can be measured by blocking a uniform wind tunnel airstream of speed U with a sample of the material, and measuring the resulting pressure drop Δp (across the blockage) which drives the flux of air through the impediment. Then following Laws & Livesey (1978),

$$k_r = \frac{\Delta p}{\rho U^2}\;. \tag{1.16}$$

Knowing the resistance coefficient of a windbreak, one can calculate the force per unit area exerted by the windbreak on the air flow: an element of the barrier with area $\Delta y \Delta z$ exerts a localized drag force $F_{Dx} = k_r \rho \overline{u}\;\sqrt{\overline{u}^2+\overline{v}^2+\overline{w}^2}$, where the velocity is evaluated at the barrier element.

To calculate the velocity statistics in the surroundings of the shelterbelt of the Indian Head dust dispersion experiments, the RANS equations have been solved with the trees parameterized as an effective porous barrier with resistance coefficient $k_r = 2.5$, a value which optimized model agreement with the observed wind speeds (see Section 3.2.2).

Mean velocity field near a windbeak Several previous studies (e.g. Wilson 1985; Cleugh 1998; Wang et al. 2001 as cited by Asman 2005) have explained that loss of momentum to the material of the windbreak or shelterbelt results in a reduced mean velocity, not only downstream but also over a short range upstream, courtesy of the pressure disturbance. A rise in mean pressure upwind of the barrier deflects the mean streamlines upward, resulting in a jet passing over the barrier. Meanwhile the air following streamlines through the barrier, called the "bleed flow," is severely retarded by the drag force and emerges into the quiet zone as a slow-moving current that is further retarded by an adverse mean pressure gradient, so that minimum velocity occurs some $3 - 5H$ downwind from the downwind face of the shelter.

On emerging from the windbreak the (much decelerated) bleed flow is characterized by weak vertical shear, i.e. it is roughly height-independent at $z/H \leq 1$. Raupach et al. (2001) defined a harmonic mean bleed velocity

$$U_b = \left(\frac{1}{H} \int_0^H U^2(0,z)\, dz \right)^{1/2}, \tag{1.17}$$

and showed that this is related to the resistance coefficient of the windbreak by the equation

$$U_b = U_H (\frac{\Gamma_b}{k_r})^{1/2}, \tag{1.18}$$

where Γ_b is defined as the bulk windbreak drag coefficient and U_H is an upwind reference wind speed at the windbreak height $z = H$. The bleed velocity is important because (as covered below) it carries a convective flux of particulates that may suffer deposition onto the windbreak elements.

Wang et al. (2001) reviewed the patterns of flow and turbulence for windbreaks from nearly solid (porosity = 0) to open (porosity =1). They found that the curvature of mean streamlines increases with decreasing porosity; the upward-curving streamlines become steeper as they compress over the top of the windbreak. The shape of the streamlines forms three distinct zones: the windward wind-reduction zone, the leeward wind-reduction zone where the quiet zone is located, and the accelerating zone over the top of the windbreak. In addition, recirculation (flow reversal) is generated downwind of windbreaks when porosity is to 0.3 or less. Significant decreases in mean wind speed and turbulence are found in the wind-reduction zones (below the height of windbreak) due to drag forces exerted by windbreak elements (i.e. leaves, branches). Wang et al. (2001) explained that the drag force exerted on the air by windbreaks would disturb the ambient pressure field; the disturbed pressure would modify the wind speed, and the modified wind speed would again change the drag force. In this way, the disturbed pressure field is important in determining the effects of windbreaks on the ambient wind field.

Turbulent velocity field When one compares the Reynolds equations for the ASL disturbed by a windbreak with the corresponding equations for the horizontally uniform ASL (no obstacles), additional terms appear not only in the mean momentum equations, but also in the equations for components of the Reynolds stress tensor $R_{ij} \equiv \overline{u_i'u_j'}$ and turbulent kinetic energy (TKE). Nevertheless despite strong production of TKE at the windbreak, a quiet zone with *reduced* TKE is observed in the near lee of a windbreak, possibly because motion with small time and length scales is subject to rapid dissipation to heat. The quiet zone is bounded by increased TKE in the wake where TKE is generated by the increased shear production in the strong shear zone.

1.3.2 Effects on a transported plume of particles

Raupach et al. (2001) gave a general overview of what happens when a particle-bearing air layer encounters a transverse windbreak. In their theory the depth of the particle-laden layer is assumed to be much deeper than the height of the windbreak (H), so that the incident particle concentration is uniform in the vertical direction. As the layer of particle-laden air approaches the windbreak, some of the incident air passes over the top of the windbreak and some passes through it as the bleed flow. Particles embedded in the bleed flow are subject to deposition onto windbreak elements, so that the bleed flow may emerge carrying a reduced burden of particulates; on the other hand, particle concentration would not change (during the upwind/downwind transition) in the air flow passing over the *top* of the windbreak. Therefore, the reduction of particle concentration *directly attributable to the wind-*

break itself is achieved by deposition onto the surface of the windbreak. Of course with increasing downwind distance (x) particle concentration is further reduced by other removal processes, e.g. gravitational settling or eventually (in the case of particles small enough to remain suspended) precipitation scavenging (washout). The windbreak has a secondary or indirect effect on particle deposition out of the flow in that its effects on the wind and turbulence perturb the alongwind transect of the deposition flux to ground.

Deposition of particles to windbreak elements According to Raupach et al. (2001) and Asman (2005), the deposition of particles to shelterbelt foliage is controlled by the following processes:

- Inertial impaction: This occurs when the inertia (mass) of the suspended particles prevents their following the streamlines as they are deflected around an object (e.g. leaf), so that they eventually strike the frontal surface of the object.

- Brownian diffusion: This occurs when particles are moved around by collisons with other particles. Smaller particles are more likely to be affected.

- Gravitational settling: This process largely depends on the size of particles. It can be ignored for small particles, but it plays a significant role in determining the effects of deposition of large particles. If w_g is the gravitational settling velocity of a certain class of particles, then settling is significant unless the ratio w_g/u_* is very small.

The deposition rate $D_e(\mathrm{~kg~s^{-1}})$ of particles to a windbreak can be expressed as (Raupach et al. 2001)

$$D_e = A_e\, g_p\, c = A_e\, g_{pi}\, c + \ A_t\, g_{pb}\, c \ , \tag{1.19}$$

where c is the particle concentration in the air flow $(\mathrm{~kg~m^{-3}})$; A_e and A_t $(\mathrm{~m^2})$ are respectively the frontal surface area of the element and the total surface area of the element (inertial impaction occurs only on the frontal surface of the vegetation element while Brownian diffusion takes place over its entire surface); finally $g_p(\mathrm{~m~s^{-1}})$ is a conductance for particle deposition, and can be decomposed into components g_{pi} for inertial impaction and g_{pb} for Brownian diffusion.

Impaction conductance The impaction conductance describes the speed at which particles are deposited onto vegetation frontal surface (Asman, 2005), and it is often formulated as

$$\frac{g_{pi}}{U} = \left(\frac{St}{St + p}\right)^q \ , \tag{1.20}$$

where St is the Stokes number (given below), U is the wind speed in the streamwise direction and p and q are dimensionless coefficients. According to Bache (1981) and Peters & Eiden (1992), $p = 0.8$ and $q = 2$ are suitable values for several element shapes. The Stokes number is given by

$$St = \frac{\rho_p\, {d_p}^2\, U}{9\, \rho\, \nu_a\, d_e} \ , \tag{1.21}$$

where ρ_p and ρ are respectively the particle density and the air density (kg m^{-3}), d_p is the particle diameter, and d_e is the length scale of the vegetation element. The value of g_{pi}/U for small particles increases with wind speed, and g_{pi}/U increases with particle diameter.

Brownian diffusion conductance According to Kays & Crawford (1980), the Brownian-diffusion conductance (g_{pb}) for particles transferring through a laminar boundary layer is

$$g_{pb} = \frac{\kappa_p}{d_e} C_{Pol}\, Re^{1/2} Sc^{1/3}, \tag{1.22}$$

where κ_p is the diffusivity of the particles arising from Brownian motion (Fuchs, 1964); $Re = Ud_e/\nu_a$ is the Reynolds number for flow around the element; $Sc = \nu_a/\kappa_p$ is the Schmidt number; and C_{Pol} is the Polhausen coefficient.

Overall conductance The overall conductance is $g_p = g_{pi} + g_{pb}$, and normalizing by the wind speed we have

$$\frac{g_p}{U} = \left(\frac{St}{St + p}\right)^q + \left(\frac{A_t}{A_e}\right) C_{Pol}\, Re^{-1/2}\, Sc^{-2/3}\ . \tag{1.23}$$

Filtration of particles by a windbreak For their idealized problem – an infinitely deep and uniformly mixed layer of particulates passing an infinitely thin porous windbreak – Raupach et al. (2001) define the transmittance of the windbreak to particles as $\sigma = c_1/c_0$, where c_0 is the upwind particle concentration, and c_1 is the concentration of the downwind flow in the near lee of the windbreak (at height

$z/H \leq 1$). In a Lagrangian reference frame, the particle concentration c (particles m^{-3}) is governed by

$$\frac{dc}{dt} = -\alpha\, g_p\, c\,, \tag{1.24}$$

where α is the frontal area density of the windbreak elements. A relationship between the transmittance (σ) and the optical porosity (τ) of the windbreak can be derived from Equation. (1.24), viz.

$$\sigma = \tau^{m\,E}, \tag{1.25}$$

where m is a factor to account for the meandering of the turbulent flow in its passage through the windbreak, and $E \approx g_P/U$ for particles larger than around $1\,\mu$m (for which Brownian diffusion is negligible). For sufficiently large particles and sufficiently small vegetation elements, both E and m are close to 1. Therefore $\sigma \approx \tau$ would be a practical approximation for particle diameters d_p larger than about $30\,\mu$m with vegetation element length scale d_e smaller than 30 mm (most typical vegetation element sizes).

There is an optimal value of optical porosity for maximum total deposition of particles to a windbreak, whose value is believed to lie in the range $0.1 - 0.2$. As outlined by Raupach et al. (2001) and Asman (2005), the optimal value is determined by a trade-off; specifically, the deposition increases with the density of the windbreak, but particles need to pass the windbreak in the first place to deposit in the downwind direction. Therefore, the windbreak should not be too dense because the speed of the bleed flow *decreases* with increasing density of the windbreak (and fewer particles will be filtered). For particles with diameters larger than 1 μm the number of particles entrapped by the windbreaks increases with the undisturbed wind speed because the inertial impaction is the dominant deposition process for these particles. For smaller particles Brownian motion is the most important mechanism.

1.4 Atmospheric dispersion

After pollutants are injected into the atmosphere from a source, their dispersion is governed by the state of the atmosphere; equivalently put, the spatial fields of the mean wind and of the turbulence statistics exert a strong influence on the trajectories of particles. For this reason, if statistics of the wind field are known, the dispersion of pollutants can be simulated by a number of theoretical approaches, these being of greater or lesser fidelity to the truth of the process.

1.4.1 Statement of mass conservation – Eulerian form

Let $c = c(x, y, z, t)$ be the instantaneous concentration of some species (gas or particulate) in the air, and let $\mathbf{F}$ [$\mathrm{kg\,m^{-2}\,s^{-1}}$] be the instantaneous local vector flux density of this species. If there are no sources or sinks of c within the atmosphere, then conservation of mass demands that

$$\frac{\partial c}{\partial t} = -\,\nabla \cdot \mathbf{F}\ , \tag{1.26}$$

that is, the rate of change of c at any point is given by (minus) the local divergence of the *flux* of c.

To proceed, we identify the flux as

$$\mathbf{F} \equiv \vec{F} \equiv F_i = (u_i - w_g \delta_{3i})\ c - D\,\nabla c\ , \tag{1.27}$$

where the first (and overwhelmingly dominant) component is the convective flux (with a correction for gravitational settling), and the second is the flux due to molecular diffusion (D is the molecular diffusivity). Substituting, we obtain

$$\frac{\partial c}{\partial t} = -\nabla \cdot (\mathbf{u}c - D\nabla c) + \ w_g \frac{\partial c}{\partial z}\ . \tag{1.28}$$

However it is justifiable to neglect molecular transport, so the above equation simplifies to

$$\frac{\partial c}{\partial t} = -\nabla \cdot (\mathbf{u}\,c) + \ w_g \frac{\partial c}{\partial z}\ . \tag{1.29}$$

Now we take the Reynolds average. The resulting equation for the mean concentration, expressed using tensor notation, is

$$\frac{\partial \overline{c}}{\partial t} = -\frac{\partial}{\partial x_i}\,\left(\overline{u}_i\,c + \overline{u_i'\,c'}\right) + \ w_g \frac{\partial \overline{c}}{\partial z}\ , \tag{1.30}$$

and (using the fact that, to a good approximation, the wind vector in the ABL is non-divergent) it is easy to transform this to

$$\frac{\partial \bar{c}}{\partial t} + \bar{u}\frac{\partial \bar{c}}{\partial x} + \bar{v}\frac{\partial \bar{c}}{\partial y} + (\bar{w} - w_g)\,\frac{\partial \bar{c}}{\partial z} = -\frac{\partial \overline{u'c'}}{\partial x} - \frac{\partial \overline{v'c'}}{\partial y} - \frac{\partial \overline{w'c'}}{\partial z}\ . \tag{1.31}$$

The immediate point is that we have an unclosed system of equations — even if we knew the mean velocity vector, we would be left with one equation in several unknowns, viz., the mean concentration and the eddy fluxes. To progress, a closure approximation is needed.

Gradient transfer approach

The simplest closure, known as the eddy diffusion closure (or alternatively as gradient transfer closure, or K-theory, or first-order closure) assumes that airborne species are moved down the mean gradient of material concentration by turbulence, at a rate proportional to the magnitude of the gradient (Pasquill & Smith 1983). Temporarily switching the terminology so as to refer to a generic species q in the atmosphere, the general equation of gradient transfer, here expressed for the flux along direction i, is

$$F_i = -K_{q(i)} \frac{\partial \overline{q}}{\partial x_i}, \tag{1.32}$$

(the bracket (i) on K indicates that i is *not* to be interpreted as a repeated subscript, so that no summation over i is implied). Here $K_{q(i)}$ is the eddy diffusivity for q along the axis i, most fundamentally defined as the ratio of flux to gradient

$$K_{q(i)} = -\frac{F_i}{\frac{\partial \overline{q}}{\partial x_i}} \ . \tag{1.33}$$

We can use the gradient transfer approach to model the particle eddy fluxes $\overline{u'_i c'}$ appearing in Equation (1.31), viz.

$$\overline{u'c'} = -K_x \frac{\partial \bar{c}}{\partial x} \ , \tag{1.34}$$

$$\overline{v'c'} = -K_y \frac{\partial \bar{c}}{\partial y} \ , \tag{1.35}$$

$$\overline{w'c'} = -K_z \frac{\partial \bar{c}}{\partial z} \ . \tag{1.36}$$

The scalar eddy diffusivities (K's) have the unit $[\,\mathrm{m^2 s^{-1}}]$, and here we have allowed them to be numerically distinct (anisotropic) w.r.t. the three directions of motion, while their values may vary with position. In homogeneous turbulence, the K's are (by definition) independent of position, and in homogeneous isotropic turbulence they are (furthermore) identical for all three directions of transfer.

If we adopt Equations (1.34 - 1.36) and choose coordinates so as to make $\bar{v} = 0$, the earlier derived mass conservation equation (Equation 1.31) becomes

$$\frac{\partial \bar{c}}{\partial t} + \bar{u}\frac{\partial \bar{c}}{\partial x} + (\bar{w} - w_g)\frac{\partial \bar{c}}{\partial z} = \frac{\partial}{\partial x}(K_x \frac{\partial \bar{c}}{\partial x}) + \frac{\partial}{\partial y}(K_y \frac{\partial \bar{c}}{\partial y}) + \frac{\partial}{\partial z}(K_z \frac{\partial \bar{c}}{\partial z}) \ . \tag{1.37}$$

Further simplification of this advection-diffusion equation yields several widely used (but overly simplistic) analytical models of atmospheric dispersion.

Gaussian puff models in a homogeneous field of turbulence

Assume (for the moment) we were considering the motion of particle-laden air in a homogeneous and unsheared field of turbulence on a planet with negligible gravity field, such that $\bar{u}(z) \to U$ (a constant), $w_g \to 0$, and the eddy diffusivities K_x, K_y, K_z also are constants.

Under these assumptions Equation 1.37 simplifies to

$$\frac{\partial \bar{c}}{\partial t} + U\frac{\partial \bar{c}}{\partial x} = K_x\frac{\partial^2 c}{\partial x^2} + K_y\frac{\partial^2 c}{\partial y^2} + K_z\frac{\partial^2 c}{\partial z^2}. \tag{1.38}$$

For the release of $q[\,\mathrm{kg}]$ at $x = y = z = t = 0$ into an unbounded space, the solution for the (time-dependent) ensemble mean concentration field is

$$\bar{c}(x, y, z, t) = \frac{q}{2\pi^{3/2}\sigma_x\sigma_y\sigma_z}\ \exp\left[-\frac{(x - Ut)^2}{2{\sigma_x}^2} - \frac{y^2}{2{\sigma_y}^2} - \frac{z^2}{2{\sigma_z}^2}\right]. \tag{1.39}$$

This represents a Gaussian spread along each of the three axes independently, relative to a drifting puff center point $x = Ut, y = z = 0$. The spread parameters (puff standard deviations) are related to the eddy diffusivities:

$$\sigma_x = \sqrt{2K_x t}\ , \tag{1.40}$$

$$\sigma_y = \sqrt{2K_y t}\ , \tag{1.41}$$

$$\sigma_z = \sqrt{2K_z t}\ . \tag{1.42}$$

These formulae indicate that the puff (or cloud) expands in size at a rate that is proportional to $t^{1/2}$.

Suppose, now, that c was being released continuously from a steady source (i.e. $\frac{\partial \bar{c}}{\partial t} = 0$). The solution for the steady-state spatial field of concentration (still assuming the space to be unbounded) is

$$\bar{c}(x, y, z) = \frac{q}{2\pi^{3/2}\sigma_y\sigma_z U}\ \exp\left[-\frac{y^2}{2{\sigma_y}^2} - \frac{z^2}{2{\sigma_z}^2}\right] \tag{1.43}$$

with

$$\begin{aligned}\sigma_y &= \sqrt{2K_y\frac{x}{U}}\,, &(1.44)\\ \sigma_z &= \sqrt{2K_z\frac{x}{U}}\,. &(1.45)\end{aligned}$$

According to this solution, spatial concentration in a homogeneous field of turbulence can be described as a Gaussian distribution along each cross wind direction. The spread parameters are the standard deviations of the Gaussian distributions, and the plume widths increase parabolically with downwind distance (x) since a 1-1 relation exists between x and t (i.e. $x = Ut$).

Although these solutions are helpful in modeling dispersion in a homogeneous surface layer, these simplistic solutions do not apply to the experimental regime of the Indian Head dust dispersion trials. The weakness of these solutions from the Eulerian (fixed point) view is shown by Taylor's analytic solution for homogeneous turbulence in the next section, which leads to an alternative theoretical approach, taking the Lagrangian (or particle following) point of view.

Taylor's analysis for homogeneous turbulence

G.I Taylor's (1921) rigorous analytical theory for dispersion in homogeneous turbulence provided an important insight into the nature of the eddy diffusivity, revealing that it must be regarded as being a function of elapsed time since the release of a particle. More crucially though, the theory is relevant here in that its subsequent generalization has led to today's "Lagrangian stochastic" model of atmospheric dispersion, which is the most accurate available, and will be used to simulate the Indian Head dust dispersion trials. Furthermore Taylor's theory points up which properties of turbulence are the essentials controlling dispersion.

Suppose a particle is released at $z = t = 0$ into an infinite domain of homogeneous and stationary turbulence (we here focus on particle displacement along the vertical axis, but there is nothing special about this choice/direction). Some time t after the release, the displacement[‡] in the vertical direction is

$$Z = \int_0^{t'=t} W(t')\, dt', \tag{1.46}$$

where $W(t')$ is the vertical velocity *of the particle*

$$W(t') = \left(\frac{dZ}{dt} \right)_{t=t'} .$$

By the chain rule of differentiation

$$\frac{dZ^2}{dt} = 2\, Z(t)\, \frac{dZ}{dt} = 2 \int_0^{t'=t} W(t)\, W(t')\; dt'. \tag{1.47}$$

Now suppose that a sequence of these particles are released, independently, such that one has an ensemble of trajectories in the flow. Ensemble average property values may be defined, and in particular the rate of change of mean square particle displacement follows from

---

[‡] A common convention is to represent Lagrangian variables by way of upper case characters, thus, a particle's position on the vertical axis is Z and its vertical velocity is $W \equiv dZ/dt$.

Equation.(1.47) as

$$\frac{\mathrm{d}\overline{Z^2}}{\mathrm{d}t} = 2\overline{Z\frac{\mathrm{d}Z}{\mathrm{d}t}} = 2\int_0^{t'=t} \overline{W(t)W(t')}\, dt' \ . \tag{1.48}$$

The spread of the plume in the vertical direction can be defined as

$$\sigma_z \ = \ \sqrt{\overline{Z^2}}$$

(root-mean-square vertical displacement) and a Lagrangian velocity autocorrelation can be defined as

$$R(t',\tau) = \frac{\overline{W(t')W(t'+\tau)}}{{\sigma_w}^2}, \tag{1.49}$$

where $\tau = t - t'$. Statistics of stationary turbulence are independent of time, so $R(t',\tau) = R(\tau)$. Therefore, $\mathrm{d}\tau = -\mathrm{d}t'$, $\tau = 0$ when $t' = t$, and $\tau = t$ when $t' = 0$. Equations 1.48 and 1.49 give the analytic solution for the rate of increase of mean square particle displacement,

$$\frac{\mathrm{d}\overline{Z^2}}{\mathrm{d}t} = 2{\sigma_w}^2 \int_0^{\tau=t} R(\tau)\, \mathrm{d}\tau \ . \tag{1.50}$$

This rigorous theoretical result, though applicable only to an idealized regime of turbulence, demonstrates that the time rate of change of the mean square particle displacement depends on the vertical velocity variance, and a time integral of the Lagrangian velocity autocorrelation function. It will be useful to introduce a Lagrangian integral time scale

$$T_L = \int_0^{\tau=\infty} R(\tau)\, \mathrm{d}\tau \ , \tag{1.51}$$

in terms of which clearly

$$\left(\frac{\mathrm{d}\overline{Z^2}}{\mathrm{d}t}\right)_{t \gg T_L} = 2\,\sigma_w^2\, T_L \ \ (= \mathrm{const})\,. \tag{1.52}$$

The earlier Gaussian solution (Equation 1.42) implies that

$$\frac{\partial {\sigma_z}^2}{\partial t} = 2K_z \; , \tag{1.53}$$

which can be reconciled to Equation 1.50 to give

$$K_z = {\sigma_w}^2 \int_0^{\tau=t} R(\tau)\,\mathrm{d}\tau \; . \tag{1.54}$$

This establishes that the eddy diffusivity is a function of particle travel time, as stated in the beginning of this section. The classical diffusion theory which predicts a plume width σ_z increasing as $\sqrt{t}$ for all t is incorrect. In the so-called "near field," when $t \ll T_L$ and $R(\tau) \approx 1$ by the definition of the Lagrangian velocity autocorrelation (Equation 1.49), Equation (1.50) gives

$$\sigma_z = \sigma_w t \; . \tag{1.55}$$

The plume spreads *linearly* in time shortly after initial release.

Furthermore these results establish that the eddy diffusivity *is* a constant (i.e. independent of time) in the "far field" (i.e. for travel times $t \gg T_L$), with the specific value $K_z = K_\infty = {\sigma_w}^2 T_L$ from Equation (1.54). From Equation (1.50), it follows that in the far field

$$\sigma_z = \sqrt{2\,K_\infty}\,\sqrt{t} \; . \tag{1.56}$$

From these justifiably results, Taylor deduced that:

1. the statistical evolution of concentration in homogenous turbulence is completely governed by two statistical properties of the turbulence, namely σ_w and T_L; and,

2. particles seen at a point z may have different effective diffusivities corresponding to their different times of release (which as Taylor noted, is illogical).

Therefore, though it provides an adequate approximation in the far field of a source, the classical K-theory often used to close the mass conservation equation (Equation 1.37) is fundamentally wrong, representing a serious weakness in the simplest Eulerian approach to modeling atmospheric dispersion. Similar and related difficulties arise with so-called "higher-order" turbulence closures, however the difficulty can be overcome by pursuing the Lagrangian approach and numerically "mimicking" an ensemble of particle trajectories. This approach has flowered since computers became commonly and cheaply available, and it will now be very briefly described. Much more detail will be given in Chapter (3).

1.4.2 Lagrangian stochastic modeling of dispersion

Suppose for the present we restrict our attention to "passive" particles or "fluid elements," i.e. particles that are not subject to buoyancy forces and whose inertia is so small as to allow them to track all motions of the fluid (air). Then Equation.(1.29) reduces to

$$\frac{dc}{dt} \equiv \frac{\partial c}{\partial t} + \mathbf{u} \cdot \nabla c = 0, \tag{1.57}$$

where dc/dt is the parcel following (or "material") derivative. To a satisfactory accuracy, particle concentration does not change along its trajectory, and this is the basis for the Lagrangian approach to turbulent dispersion. If initial concentration is c_0 at $t = 0$ for a tagged fluid element, the concentration for that fluid element will remain constant as time elapses. The Lagrangian approach to solving turbulent dispersion is to calculate the trajectories of a large sample of independent "tagged" fluid elements. Once an ensemble of trajectories are known, the mean concentration in a sampler of volume V can be deduced as

$$\bar{c} = \frac{Q\bar{t}}{V}, \tag{1.58}$$

where $\bar{t}$ is the average time a (model) particle spends in the volume V, and Q is the rate of release of particles from the source.

Single-particle Lagrangian stochastic models

Assuming that flow statistics are known (i.e. given), the modern numerical Lagrangian stochastic (LS) model computes an ensemble of particle trajectories in the given system. Numerical LS models calculate the evolution of particle positions in a sequence of steps, for example, in the vertical direction:

$$Z(t) = Z(0) + \sum W \Delta t \ , \tag{1.59}$$

where Δt is the time step. In order to mimic the trajectories of particles correctly, the generated sequence of Lagrangian velocities W must have the same statistical properties as would real world trajectories, e.g. σ_w and T_L. The "well-mixed condition" (Thompson, 1987) is the most powerful known constraint on the design of an LS model, and (simply put) it states that a set of tracer particles which are initially well-mixed in the flow, must remain so for all later times. I shall elaborate on this below.

LS model in a horizontally uniform atmosphere

It is widely believed to be an adequate approximation to treat surface layer turbulence as *Gaussian*, but vertically-inhomogeneous. Furthermore except very close to the ground, the mean alongwind velocity $\overline{u}$ is large in magnitude w.r.t the typical fluctuations (u'); for this reason, dispersion in the streamwise direction can often be ignored. Thus plausibly the LS model may be one-dimensional, in the sense that only the *vertical* component of the Lagrangian velocity needs to be modeled. Needed wind statistics can be provided to the LS model by applying the Monin Obukhov similarity theory (see Section 1.2).

LS model in a disturbed atmosphere

For regions where the air flow is highly disturbed, such as near a windbreak, MOST does not apply. However RANS computational wind models can be used to obtain necessary statistics used to drive an LS model, and to simulate the Indian Head dust dispersion trials. This was accomplished by numerically solving rigorous budget equations for the turbulent stresses appearing in the momentum equations, which are derived by manipulation of the Navier-Stokes equations using a well known second-order closure scheme (Wilson 1985). The RANS calculation provided the spatial fields of the mean wind vector $\overline{u}_i$, the Reynolds stress tensor τ_{ij}, and the turbulent kinetic energy dissipation rate ϵ.

1.5 Project overview and earlier studies

This thesis is based on a research project studying the effects of a windbreak on the dispersion of road gravel dust in Saskatchewan. Gravel roads are very common in the countryside in Saskatchewan; as people drive vehicles along the dry gravel roads, dust particles are disturbed and transported by the wind, and objects (e.g. buildings) downwind are subjected to passing puffs or plumes of dust, which represents an air pollutant and a nuisance. As mentioned in the previous section, the main function of a windbreak is to provide shelter in its lee, where the magnitude of the wind is reduced, along with the rates of turbulent transport of scalar quantities (i.e. heat, vapor, carbon dioxide). Therefore, it is natural to raise the following question: **is constructing a windbreak an effective means to mitigate the concentration of gravel dust?** To answer the question one must determine the *difference* between the dispersion patterns of dust particles in an area sheltered by a natural windbreak, and in a neighboring unsheltered area.

Several previous studies have studied particle transport and dispersion as disturbed by windbreaks, by means of field experiments and/or numerical models. Raupach et al. (2001) developed a new theoretical model to study entrapment of particles by thin windbreaks (details of the model are described in Section 1.3.2) and to demonstrate the effectiveness of their theoretical model, they conducted experiments in Australia to measure the transmittance of oil-based droplets having a log median diameter of about 80 μm (large particles) as they passed through different windbreaks at different wind speeds, with the wind direction approximately perpendicular to the windbreaks. The number of rows of the experimental windbreaks varied from 1 to 4, and the heights of the windbreaks varied from 7 to 11 m. Their results showed that $80 - 90\%$ of the particles were filtered from the bleed flow; the ratio of downwind to upwind concentrations increased with wind speed in strong winds (over $6\,\mathrm{m\,s^{-1}}$), and decreased with wind speed at low wind speeds (less than $1\,\mathrm{m\,s^{-1}}$).

Wilson (2000) compared heavy particle deposition, simulated by a sequence of the most rudimentary of Lagrangian models and more faithful but time-consuming approach of explicitly modeling particle acceleration using equations of motion, with the observations reported by Hage (1961) and Walker (1965) of surface deposition of glass beads with mean diameters of 49 μm, 56 μm, and 107 μm under neutral atmospheric conditions. The glass beads were released continuously from a height of 7.4 m or 15 m over a field at the Suffield Research station in Alberta, Canada. Wilson found that to compute trajectories of particles in this size range it suffices to add a gravitational settling velocity w_g to a well-mixed first order Lagrangian stochastic model for fluid element trajectories, and to reduce the velocity autocorrelation timescale along the heavy particle trajectory relative to the fluid-Lagrangian timescale. The fidelity of the LS model is not significantly lower than explicitly modeling particle acceleration using the particle equation of motion except in the region very close to the ground where the ratio of particle inertial timescale to turbulence timescale is not small. With the timescale reduction parameter $\beta \sim 2$, the results simulated by the LS model with the superposition of a gravitational settling velocity and reduced velocity autocorrelation timescale showed satisfactory agreement with observation, generally within 20% error.

Bouvet et al. (2006) conducted experiments in France to observe the deposition of heavy particles (glass beads with gravitational settling velocity $8.7\,\mathrm{cm\,s^{-1}}$) in a horizontally-homogeneous wind field, and in a non-uniform wind field disturbed by a fence standing perpendicular to the prevailing wind. A Lagrangian stochastic (LS) particle trajectory model, coupled with a wind model based on a Reynolds stress turbulence closure, was utilized to simulate heavy particle dispersion. A heuristic adjustment based on Wilson's (2000) approach was adopted to account for the inertia of heavy particles. Bouvet et al. found that the modeled deposition rates matched the observations to a degree of accuracy expressed as $E = 30\%$, where E is the root-mean-square error normalized by the peak value of deposition rate along the deposition swath. From the pattern of deposition rate, they concluded that the relative positions of source and fence determined the importance of direct deposition to the windbreak. When the source was positioned just above the height of the fence, entrapment reduced ground deposition. The disturbed wind field affected the deposition in two contrary ways: (1) the positive mean vertical wind near the fence lifted the particle plume, which (acting alone would have) caused the particles to drift further downwind before depositing to ground; but (2), the decreased horizontal wind speed caused the particles to deposit much earlier and the spread of the deposited particles was significantly reduced.

Bouvet et al. (2007) extended their research to study the filtering function of a thick natural windbreak, making measurements of the transport and deposition of artificial particles (again, glass beads) to a thick shelterbelt composed of four rows of maize with an aspect ratio W/H of 1.6. Vertical profiles of particle concentration and wind speed allowed the determination of the streamwise particle fluxes upwind and downwind of the shelterbelt, and the deposition flux to ground within the shelterbelt was also measured. The numerical model (again, a Lagrangian stochastic model coupled with a RANS wind model) was modified to add an algorithm for deposition/rebound onto vegetation within the shelterbelt. Bouvet et al. concluded that the extended LS model provided a satisfactory account of concentration and deposition in the vicinity of the thick natural windbreak for which the ‘thin windbreak’ theory (Raupach et al. 2001) was inapplicable. They found that a considerable proportion of particles that had entered the shelterbelt across its upstream side were lifted by the mean updraft induced by the pressure disturbance just upwind of the shelterbelt. The abrupt change of the concentration profile across the hedge was well captured, with errors no larger than 24%. The match of observed deposition and modeled deposition was accurate within 14% and 35%. The modeling errors were caused by the input horizontal wind velocity and the modeling of particle dispersion. The windbreak preferentially filtered large particles due to their larger gravitational settling velocity, and smaller particles tended to deposit less onto vegetation.

This thesis follows more or less the method adopted in previous studies mentioned above, comparing experimental observations with model simulations in part to examine the accuracy of numerical models but in part (and as main motivation) to identify qualitative/quantitative patterns of atmospheric dispersion. As noted above, Wilson (2000) established that heavy particle trajectories can be effectively modeled by means of a Lagrangian model with superposition of a gravitational settling velocity and reduced velocity autocorrelation timescale along the heavy particle trajectory relative to the fluid-Lagrangian timescale. This thesis adopted this approach to model dust particle trajectories according to the conditions at the experimental site in Indian Head, SK.

Raupach et al. (2001) and Bouvet et al. (2006, 2007) developed theoretical methods to account for the filtering function of a windbreak.

Raupach et al. focused their study on thin windbreaks (i.e $W/H \ll 1$), and Bouvet et al (2007) extended the study to a thick natural shelterbelt ($W/H \geq 1$) by parameterizing the complicated deposition and rebound within the windbreak. The primary purpose of this project is to explore the effects of a natural windbreak with $W/H = 0.5$ on gravel dust dispersion. There is no doubt that intricate particle motion (i.e. deposition, rebound) occurs inside the windbreak. The focus for this thesis is not to develop a new theoretical method to account for the particle motion inside the windbreak, but to utilize existing theories and models, i.e., a theory for particle entrapment by thin windbreaks (Raupach et al. 2001), and a modified Lagrangian model following the description of Wilson (2000), to simulate dust dispersion, specifically concentration downwind of the windbreak as contrasted with that prevailing in an open (unsheltered) area. The model results can be compared with measurements conducted in the field, thereby to deduce the effects of the windbreak. The secondary purpose of the project is to provide new measurements (1) to evaluate the performance of the Lagrangian stochastic model through comparison of modeled data to observations, and (2) to show the usefulness of the existing heuristic approaches to model atmospheric dispersion.

The methodology of the field experiments and their subsequent analysis, along with key experimental results, are described in Chapter (2). Theoretical details of the Lagrangian stochastic model developed for this project are described in Chapter (3), and the modeled results are presented in Chapter (4). Chapter (5) compares the experimental results to modeled results. Finally, a conclusion is provided in Chapter (6).

Chapter 2

Field experiments in Indian Head, SK

Field experiments to study the effect of a natural windbreak on the dispersion of gravel dust were conducted in Indian Head, Saskatchewan, during the summer of 2011. In this Chapter I introduce the methodology of the experiments, describing the field site, the arrangement of sensors, and the meteorological conditions during the experiments. Methods used to process the wind and dust concentration data are introduced. The chapter concludes with an overview of the measured data, and some interpretation.

2.1 Experiment setup

Field surrounding

A gravel road, located 60 m west of a shelterbelt, served as the dust source for the experiments. Gravel is composed of unconsolidated rock fragments having a wide range of particle sizes. Dust particles are blown off easily as vehicles travel along the gravel road. Smaller particles can be carried longer distances by the prevailing wind, whereas larger particles tend to quickly fall out of the air.

The shelterbelt in this experiment consisted of two rows of trees: green ash (*Fraxinus pennsylvanica*) (Gucker 2005) in the west (upwind facing) row, and scots pine (*Pinus sylvestris*) (Sullivan 1993) in the east (downwind facing) row (Figure 2.1). The windbreak was oriented north-south at longitude -103.99237 degrees, and its length spanned the latitude range 50.58810 to 50.59335 degrees (as already noted, the trees were located 60 m east of the gravel road). A 50 m section of trees had been removed from the south end of the (originally, longer) windbreak in order to provide an "unsheltered" area[*] to serve as a reference site for comparison with the area sheltered by the windbreak (Figure 2.2). The bounding dimensions of the windbreak were its height ($H = 10\,\mathrm{m}$) and width ($W = 4.7\,\mathrm{m}$), giving an aspect ratio $W/H \approx 0.5$.

The presence of the windbreak has two consequences. Firstly, it disturbed the ambient wind field which, in the absence of the windbreak, should have been horizontally homogeneous. Secondly, it filtered airborne dust particles carried by the bleed flow as they passed through the windbreak. Therefore, measurements of wind and aerial dust con-

---

[*] The quotes on "unsheltered" are appropriate, because for downwind distances x that are not small compared to the 50 m width of the gap one may well expect an influence of the shelterbelt on the wind speed – and such an influence is suggested by the wind data to be given later in this chapter.

centration in the lee of the windbreak and matching measurements in the unsheltered (i.e. reference) area were the primary purpose of the experiment.

Figure 2.1: The windbreak at the field site, running in the North-South direction.

For clarity, the coordinate system is presented before further description of the experimental setup (see Figure 2.3). The windbreak was located along the positive y axis; the unsheltered area ($y < 0$) stretched for about 50 m along the north south direction; the concentration measured in the unsheltered area is chosen as the reference transect for comparison with concentration measured in the lee of the windbreak. The downwind direction was along the positive x axis, and we define $x = 0$ as the location of the windbreak. In this thesis, position

Figure 2.2: Trees at the south end of the windbreak were removed to create an unsheltered area.

coordinates in the x-z plane are often scaled by H, the height of the windbreak. In other words, a measurement location in the field can be expressed as $(x/H, z/H)_{\mathrm{ref}}$ along the reference measurement transect or $(x/H, z/H)_{\mathrm{lee}}$ along the sheltered measurement transect.

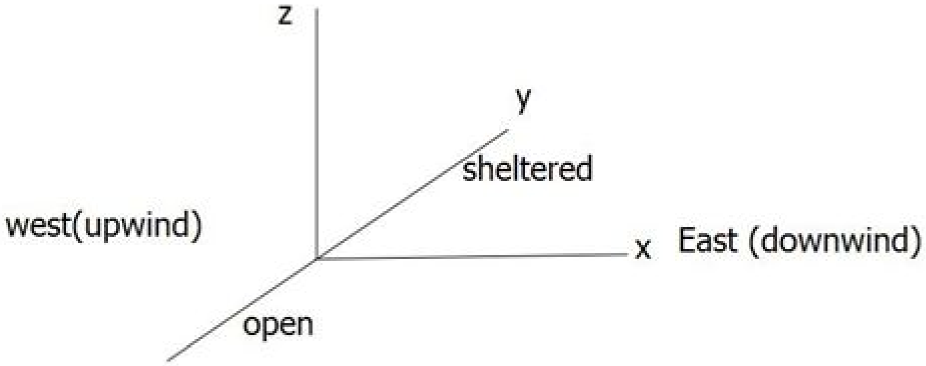

Figure 2.3: The coordinate system of the field site in Indian Head, SK. Downwind direction is along the positive x axis. In the chosen coordinate system, dust was released at $x/H = -6$.

The following two conditions must be met in order to obtain meaningful data:

- The prevailing wind must come from west because the gravel road (dust source) was located west of the windbreak.
- The gravel road must be dry so that dust on the road can be lifted and transported by the mean wind.

These conditions were met during five separate periods of experimentation, conducted in 2011 on Jul 27th, Aug 4th, Aug 10th, Aug 17th and Aug 23rd.

For each day's experiment, and with all sensors switched on, a truck was driven along the gravel road at a speed of about $80\,\mathrm{m\,hr^{-1}}$ from one end to other. As the vehicle travelled along the road, dust particles were lifted and transported by the prevailing wind, and the resulting dust plume was blown downwind. A total of 20 such runs were conducted for each field day, with a time interval of 2 minutes between any two consecutive runs. Therefore, not counting preparation time (erection of masts, etc.) it took about 40 minutes to complete each experiment.

Arrangement of sensors

Dust concentration, wind speed and wind direction were the primary variables measured at the site; other variables such as atmospheric stability, roughness length, and friction velocity can be inferred from wind data. In this experiment, dust concentrations at different downwind locations were measured by several Casella total dust burden monitors and Rotorod spore counters. Data prescribing the upwind (ambient) flow were measured by a three-dimensional sonic anemometer. Several cup anemometers were installed east of the windbreak to measure wind speed.

Casella total dust burden monitors Microdust Pro from Casella was the type of dust monitors used in the field site (Figures 2.4 and 2.5). A Microdust Pro is a real time particulate monitor for measuring instantaneous concentration of suspended particles in the air. The monitor is capable of measuring concentration (total mass of particles in a sample of air) ranging from $0.001\,\mathrm{mg\,m^{-3}}$ to $2500\,\mathrm{mg\,m^{-3}}$ by pumping air through its optical chamber to sense the change of optical refractivity of the dust-laden air.

Two Casella dust monitors were placed at locations $(0.75,\ 0.2)_{\mathrm{lee}}$ and $(10,\ 0.2)_{\mathrm{lee}}$ downwind of the windbreak[†]. Two other Casella monitors were placed at the matching positions $(0.75,\ 0.2)_{\mathrm{ref}}$ and $(10,\ 0.2)_{\mathrm{ref}}$ along the reference transect for comparison.

Rotorod spore counters A Rotorod spore counter consists of a rapidly spinning piece of U-shaped metal, whose opposing arms are coated (on opposite sides) with silicon grease so as to trap particles whose inertia prevents their being washed out of the path of the sampling arms (see Figure 2.6). In addition, the trapping sides were painted with white fingernail polish. The width and length of each rod are 2 mm and 58 mm, and the rods are 4 cm apart. During its operation in the field, a Rotorod was connected with a motor powered by a 12.7 V battery, and spun at 2400 rpm (revolutions per minute) around its central axis. When dust-laden wind passed a spinning Rotorod, dust particles would collide onto the greased sides of the rods owing to their inertia. After the experiment, rods loaded with dust particles were put under a microscope. Six 2 mm × 2 mm sampling areas were chosen on the sur-

---

[†] Position coordinates in the thesis will be denoted $(x/H,\ z/H)$, where H is the height of the windbreak.

Figure 2.4: A casella dust monitor was attached to a tripod at the height of 2 m in the field.

Figure 2.5: Attaching a Casella dust monitor to a tripod at the height of 2 m in the field.

face of each dust-loaded rod. The distance between any two neighboring sampling areas was about 1 cm. In this way, a systematic sampling was achieved in order to account for heterogeneity of dust particle distribution in size. The next step was to take a picture for each sampling area and use image-processing software to count and classify the number of trapped dust particles according to their size (see Figure 2.7). Details are given in Appendix A.

Generally speaking, Rotorods were placed on transects at $z/H = 0.2, 1.2$ at distances $x/H = (0.75, 5, 10)$ downwind of the windbreak, with matching placements in the unsheltered area. In the coordinate system adopted, these locations can be expressed as $(0.75,\ 0.2/1.2)_{\mathrm{ref/lee}}$, $(5,\ 0.2/1.2)_{\mathrm{ref/lee}}$, and $(10,\ 0.2/1.2)_{\mathrm{ref/lee}}$. However, due to some practical problems [‡], the Rotorods' positions were not always consistent for the five days. Figure 2.8 shows that a researcher was placing a Rotorod counter onto a stand at the height of 2 m in the field.

Wind measurement A 3-dimensional sonic anemometer was placed at $(-3, 0.2)_{\mathrm{ref}}$ to measure the mean and fluctuating velocities. Horizontal wind speed downwind over the field site was measured by a number of RM Young 3-cup anemometers. The original idea was to couple each cup anemometer with one Rotorod spore counter for dust concentration. However, due to practical problems, the positions of cup anemometers did not always correspond to the positions of Ro-

---

[‡] For example, a few Rotorods' motors unexpectedly stopped operating, and some Rotorods were blown off by strong winds.

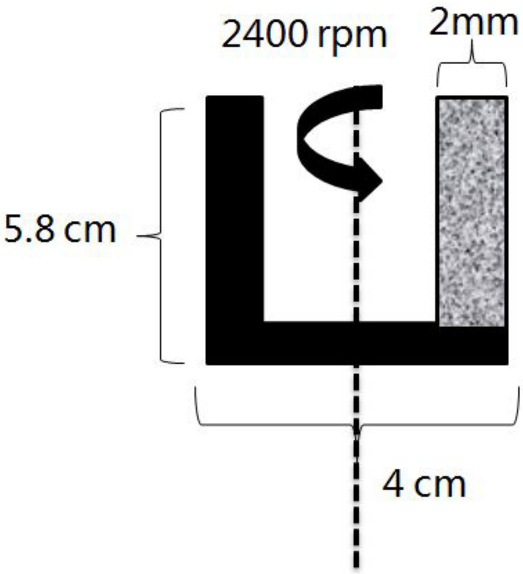

Figure 2.6: Schematic showing the dimension of a Rotorod spore counter. When it is switched on, it spins on the central axis at 2400 rpm. The grey part represents particles stuck onto the greased side of the rod.

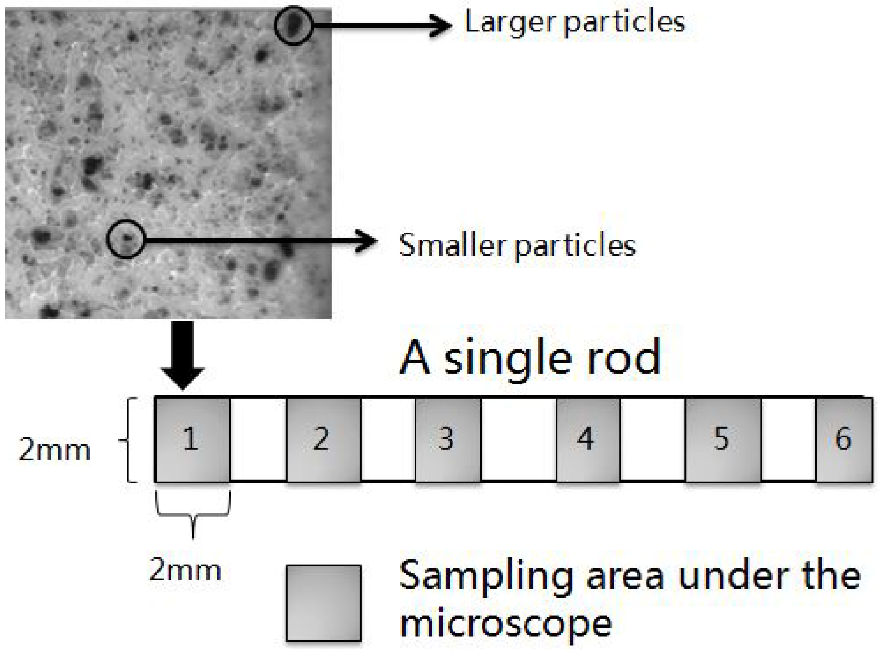

Figure 2.7: Schematic of the sampling areas on a Rotorod. Pictures of 2 mm × 2 mm sampling areas under a microscope were processed by image software to count and classify dust particles in each sampling area.

Figure 2.8: Placing a Rotorod onto a stand at the height of 2 m

torod counters. Generally, the coordinates of cup anemometers were $(0.75, 0.2/1.2)_{\mathrm{ref/lee}}$, $(5, 0.2/1.2)_{\mathrm{ref/lee}}$, $(10, 0.2/1.2)_{\mathrm{ref/lee}}$, as for the Rotorods. Figure 2.9 shows a sonic anemometer, a cup anemomenter and a Rotorod on a stand of 2 m high. Figure 2.10 shows that researchers were attaching a data logger onto a sonic anemometer in the field.

Figure 2.9: A sonic anemometer, a cup anemomenter and a Rotorod on a stand of 2 m high in the field.

Several 12 m poles with exterior arms at the height of 2 m and 12 m respectively were used in the field (Figure 2.11). Cup anemometers and Rotorods were attached onto the exterior arms. Figure 2.12 shows researchers were standing a pole in the field.

Figure 2.10: Attaching a data logger onto a sonic anemometer.

Figure 2.11: A 12 m measurement pole in the field.

Figure 2.12: Standing a measurement pole in the field.

2.2 Method of experimental data analysis

2.2.1 Meteorological conditions

The sampling frequency for the 3D sonic anemometer was 10 Hz, allowing to estimate the friction velocity u_* and the Obukhov length L (Equation 1.9). These two parameters can be used to determine wind profile in the unsheltered, flat area where no obstacles impede the wind. According to Monin-Obukhov similarity theory (see Section 1.2), the (normalized) mean wind shear can be represented by a function of z/L

$$\frac{k_v z}{u_*}\frac{\partial \overline{u}}{\partial z} = \phi_m(\frac{z}{L}) = (1 - 28\frac{z}{L})^{-1/4} \tag{2.1}$$

where the specific form given here for ϕ_m was given by Dyer & Bradley (1982) and applies in an unstably stratified atmosphere ($L < 0$).

Upon integration (Paulson 1970), the mean wind profile

$$\overline{u}(z) = \frac{u_*}{k_v}[\ln\frac{z}{z_0} - \psi_m(\frac{z}{L}) + \psi_m(\frac{z_0}{L})] \tag{2.2}$$

where

$$\psi_m = 2\ln(\frac{1+{\phi_m}^{-1}}{2}) + \ln(\frac{1+{\phi_m}^{-2}}{2}) - 2\arctan({\phi_m}^{-1}) + \frac{\pi}{2}. \tag{2.3}$$

Equations 2.1 to 2.3 together with the wind speed at $z/H = 0.2$ measured by a 3D sonic anemometer can be used to estimate the mean wind speed at $(-3,\ 1.2)_{\mathrm{ref}}$ upwind, a value which was chosen as the reference wind speed (least affected by the windbreak) to characterize the strength of the undisturbed upwind flow. By fitting the wind profile, one can estimate the roughness length z_0, characterizing the surface upwind.

The cup anemometers output average wind speed every one minute during field experiments as shown in Figure 2.13. A mean wind speed for each experimental period (40 minutes) was calculated to represent the wind speed at each measurement location.

2.2.2 Dust concentration

Rotorod data

Rotorod spore counters are specialized in measuring time average dust concentration with size discrimination over a period of time (i.e.

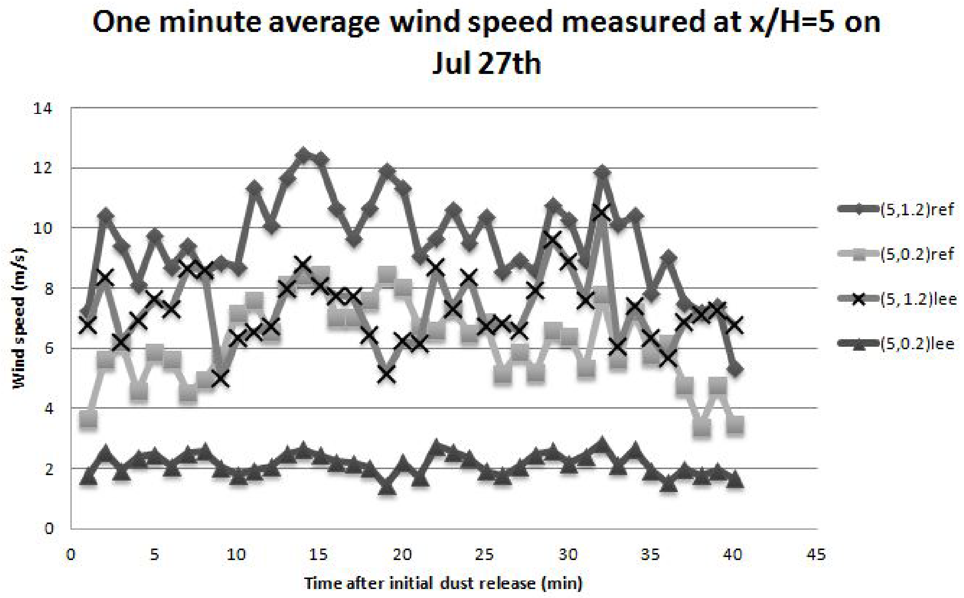

Figure 2.13: An example to show that the one minute average wind speed ($\mathrm{m\,s^{-1}}$) measured by cup anemometers fluctuated around a mean wind speed at each measurement location. "Open" stands for the unsheltered area.

40 minutes for field experiments in Indian Head, SK). By analyzing pictures of Rotorod samples using image processing software, I was able to identify dust particles of diameters from 1μm to 100μm and to classify them into 100 size bins whose centres span the range $D = 1\mu$m to $D = 100\mu$m with equal bin widths of 1μm. Concentration of dust particles in each size bin (indexed k) can be calculated by counting the number of particles in the size bin (see Equation. 2.4). In summary, the size bins are characterized by

D_{min}	1μm
D_{max}	100μm
ΔD	1μm

Theoretical basis for calculating time average dust concentration The time average concentration at a location in the field $\overline{c}_k(x, z)$ of dust of a specified size class k can be inferred from counting the number of dust particles belonging to that size class trapped by Rotorods out of the volume of sampling air swept out by the spinning rods according to the following equation (Bouvet et al. 2007)

$$\overline{c}_k(x, z) = \frac{N_k(x, z)}{A\,\Omega\,\pi\,d\,\Delta\,t\,E_I}, \tag{2.4}$$

where $N_k(x, z)$ is the number of particles on Rotorod samples falling into the kth size bin at the measurement position (x, z); A is the area of the sampling surface; $\Omega = 2400\,$rpm is the number of revolutions of the Rotorod per minute; $d = 4\,$cm is the distance of separation between the two rods of a Rotorod; $\Delta t = 40\,$min is the duration of the field experiment; and E_I is the efficiency of impaction of dust particles onto the spinning Rotorod. The latter can be calculated as

$$E_I = \frac{0.86}{1 + 0.442 {S_t}^{-1.967}}, \tag{2.5}$$

(Bouvet et al. 2007) where S_t is the Stokes number, which can be regarded as the ratio of the characteristic stopping time of a particle to the characteristic flow time around the collector (Israel & Rosner 1982). According to Aylor (1993), the Stokes number for a particle interacting with a Rotorod is

$$S_t = \frac{w_g U_t}{gl}, \tag{2.6}$$

where $l = 2\,\mathrm{mm}$ is the Rotorod width, w_g is the gravitational settling velocity of the particles (a function of particle size) and

$$U_t = \frac{\Omega \pi d}{60\,\mathrm{s}} = 5.03\,\mathrm{m\ s}^{-1} \tag{2.7}$$

is the tangential speed of the rotating rod. According to Stokes' law, the settling velocity is

$$w_g = \frac{2}{9} \frac{\rho_p - \rho_f}{\mu} g R^2, \tag{2.8}$$

where R is the radius of the particle, ρ_p and ρ_f are particle density and fluid density respectively.

For this experiment, it is assumed that the density of gravel particles is $\rho_p = 1522\,\mathrm{kg\,m}^{-3}$, and ρ_f is the air density which can be determined by the ideal gas law. In Equation 2.8, μ is the dynamic viscosity of air, which is a function of temperature. Average temperature for the five field days listed was around 300 K; μ for $T = 300\,\mathrm{K}$ is about $1.8665 \times 10^{-5}(\,\mathrm{kg\,m^{-1}\,s^{-1}})$. Figure 2.14 plots gravitational settling velocity versus particle diameter, computed for gravel dust particles having diameters less than 100 μm. Table 2.1 gives numeric values.

Diameter (μm)	$w_g(\mathrm{m\,s^{-1}})$
2	0.0002
6	0.0016
10	0.0044
20	0.0177
50	0.1109
100	0.4436

Table 2.1: Gravitational settling velocity for gravel dust particles calculated for the specified particle sizes according to Stokes' law

Equations (2.5 - 2.8) show that E_I is sensitive to particle size; in order words, the probability of particles being stuck onto the spinning rods varies with particle size. Figure 2.15 shows that efficiency of particle impaction increases as particle sizes increase, and E_I achieves the value of 1 for particle diameters larger than 25 μm when the Rotorod spins at 2400 rpm.

In addition, it is necessary to mention that the time average dust concentration calculated from Equation 2.4 has the unit (number of particles $\mathrm{m^{-3}}$). If the unit (mass $\mathrm{m^{-3}}$) is needed to express concentration, it is necessary to find out the mass of individual dust particles to obtain $\mathrm{mass/m^3} = N_k \times \rho_p \times V_k$, where V_k refers to the volume of an individual dust particle belonging to the kth size bin. For this study,

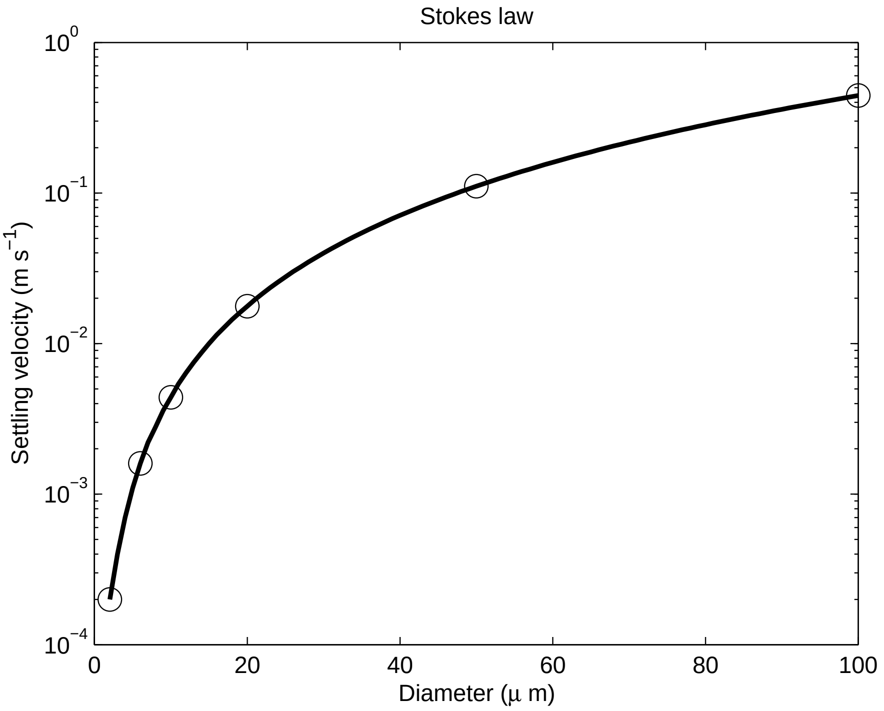

Figure 2.14: Settling velocity of dust particles detected in Indian Head experiment vs diameter, according to Stokes' law.

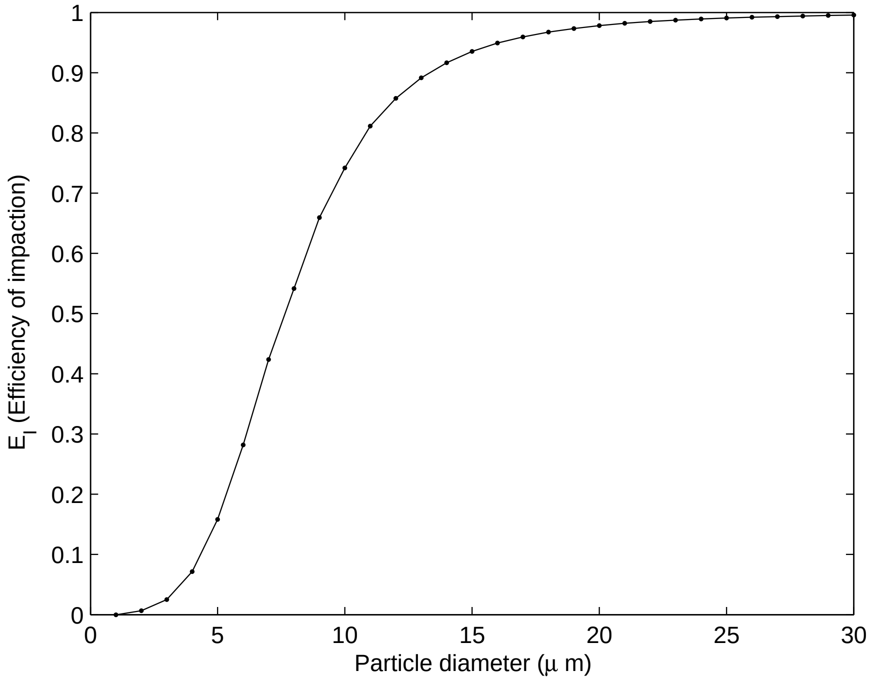

Figure 2.15: Efficiency of impaction vs. diameter, for dust particles drawing close to a Rotorod spore counter spinning at 2400 rpm.

assume dust particles are spherical and all dust particles in one size bin are uniform in size, both of which are oversimplifications. Thus $V_k = (4/3)\pi(D_k/2)^3$ can be regarded as the volume of individual dust particles in the kth size bin, where D_k is the particle diameter associated with the center of each size bin.

Casella data

Unlike Rotorod counters, Casella dust monitors can only output aggregate concentration without distinguishing particle sizes, but they can measure instantaneous dust concentration $c(t)$ at a location $(x/H, z/H)$. The time series of dust concentration obtained by Casella monitors as shown in Figure 2.16 were processed by the following two procedures, first zeroing background concentration and then correcting concentration measurement, in order to reduce measurement errors.

Zero background concentration Ideally, for a given location downwind of the dust source, dust concentration rose gradually from clear air ($c = 0$). However, due to some practical issues (e.g. the accuracy of zero adjustment operation of Casella monitors), the initial concentration was not always zero. To compensate for discrepancies and make measurements easier for comparison, I manually adjusted the background dust concentration prior to the release of dust particles for each dispersion period stemming from one vehicel pass to zero.

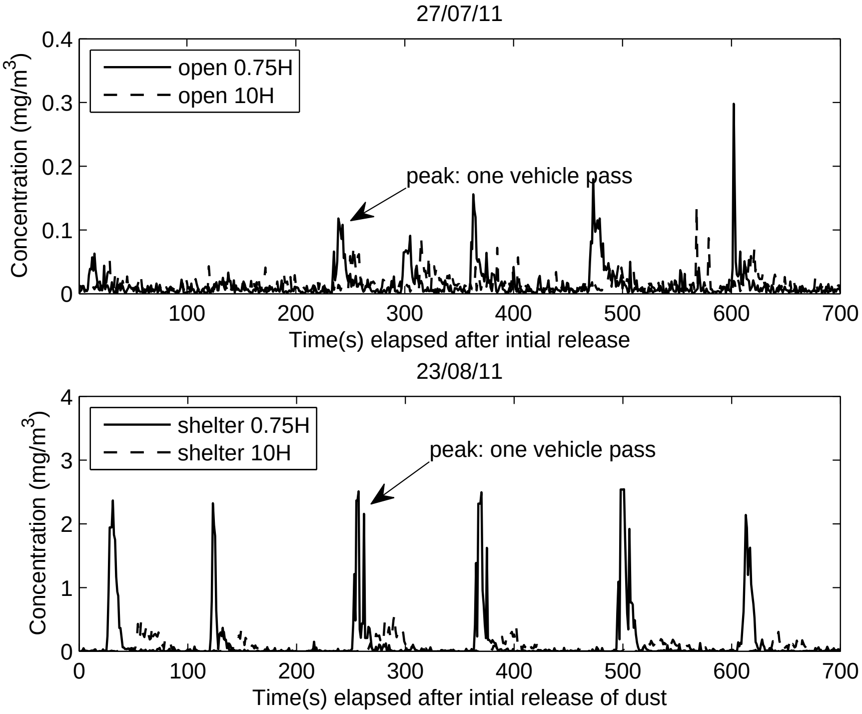

Figure 2.16: Time series of instantaneous dust concentration monitored at various downwind locations on Jul 27th, and Aug 23rd. These records are from Casella monitors placed at $z/H = 0.2$. One peak represents one pass of the vehicle on the gravel road (source of dust).

Correct concentration measurement The quality of field experiments is sensitive to the accuracy of dust concentration measured by Casella monitors. Therefore, concentration measurements need to be corrected before further analysis. In order to find out the correction factor, the four Casella monitors used in regular field days were placed side by side 30 m downwind of the gravel dust road reading instantaneous dust concentration while a vehicle was travelling rapidly from one end to other of the test area to raise dust plumes. 10 such passes with a time interval of 1 minute were conducted on Aug 23rd. Given the arrangement of the sensors, it is expected that the four Casella monitors should give the same concentration readings, hence the ensemble mean concentration for the 10 vehicle passes should overlap exactly. However, minor differences were found.

A correction method was developed to minimize the differences in the following way. First, label curves of ensemble mean concentration using the corresponding Casella monitors. Next, choose the best behaved curve obtained from the readings of Casella monitors. Find the peak value of the chosen curve as a reference value, labeled as $c(max)_0$. Then, find the peak concentration for the remaining 3 curves. The correction factor (r) for each Casella monitor should be

$$r_i = \frac{c(max)_0}{c(max)_i},$$

where i stands for the label of the Casella monitor.

Approximate ensemble mean concentration transient In a turbulent atmosphere, instantaneous concentration (c) at any location as shown in Figure 2.16 can be represented by

$$c = \langle c \rangle + c' \tag{2.9}$$

since an instantaneous property at any point in a turbulent flow is a superposition of a mean value and fluctuations. The mean dust concentration can be approximated by an ensemble average of a large number of realizations, and each passage of a dust plume is called a realization. 20 realizations were obtained for each field experiment. Figure 2.16 shows the first 6 realizations for two field days, Jul 27 and Aug 23. Each realization of dust concentration stems from gravel dust disturbed by the vehicle either moving from the south end to the north end along the gravel road or the other way around.

Before proceeding to introduce the method of ensemble averaging concentration transients in the field, it is essential to review the procedure of the field experiment, briefly outlined earlier in section 2.1 and depicted in Figure 2.17. For each field experiment, a vehicle always started at the south end point on the gravel road and was driven towards the north end on the road to complete its first pass, during which the vehicle would pass the reference transect first and then the sheltered transect. The time interval between any two consecutive passes was two minutes, with an uncertainty of $\pm 2\,\text{sec}$. Starting from the second pass (i.e. vehicle running from the north end towards the south end), the driver would ensure that he arrived at the first transect he encountered along the gravel road at the beginning of the two-minute interval with a speed of $80\,\mathrm{km\,hr^{-1}}$. Specifically, in terms of the actual time line and Figure 2.17, at $t = 0$, the vehicle started at the south end and Casella monitors were turned on at the same moment; at $t = 120\,\mathrm{sec}$, the vehicle had already started its second run towards the south end on the road and just passed the sheltered transect on the gravel road. Since the distance between the sheltered transect and reference transect was $100\,\mathrm{m}$, it took another $5\,\mathrm{sec}$ approximately before the vehicle arrived at the reference transect. The rest of the pass was not very important. The next noticeable event was that the vehicle would pass the reference transect at $t = 240\,\mathrm{sec}$ on its way to complete its third pass towards the north end. The vehicle continued in this way until a total of 20 passes had been completed; 10 of them were South to North (S-N) passes as represented by the solid arrow in Figure 2.17, and the other 10 were North to South (N-S) passes shown as the dotted arrow.

Ideally, downwind transport of gravel dust along the reference/sheltered transect would start at the moment the vehicle passed at transect, so this is the moment when the measurement time of the two Casella monitors on that transect should be set to '0' for the vehicle pass. Obviously, the time origins at each transect were different for S-N and N-S passes, and their values can be gauged from distance between the reference and sheltered transect and vehicle speed (see Figure 2.17). From the earlier description of the experimental procedures, we know that except for the first S-N pass, the vehicle would pass the reference transect at the beginning of a 2-minute S-N pass (i.e. $t = 0$), and at $t \approx 5\,\text{sec}$ for the N-S pass that follows. Conversely, the vehicle would pass the sheltered transect at the beginning of a 2-minute N-S pass, and at $t \approx 5\,\text{sec}$ on the following S-N pass.

For each experiment, the time base of the Casella monitors were synchronized with the driver's clock, which means that time was set to zero at the moment when the vehicle left the south end of gravel road and Casella monitors were switched on. After the experiment, one obtains the unshifted time series of dust concentration $c(t)$ for $0 \le t < 20 \times 120\,\text{sec}$. Because the time point at which the vehicle arrived at the reference and shelter transect on the first S-N pass was not recorded during each experiment and was subject to change due to the time needed for the vehicle to accelerate from 0 to $80\,\text{km}\,\text{hr}^{-1}$ after it started initially during the experiment, the first S-N pass (i.e. $0 \le t < 120$) was not counted for ensemble average of concentration transients. The time series $c(t)$ at $(x/H,\ z/H)_{\text{ref/lee}}$ can be further rearranged into a matrix $c_{ij}(t_i)$, where $i = [1,\ 120]$ stands for index of time points within a single 120-second pass, with $t_1 = 0$ and $t_{120} = 119\,\text{sec}$. $j = [1,\ 20]$ stands for the index of realizations (passes). Odd j's indicate S-N passes and even j's are for N-S passes. After shifting the time origin for realizations with index $j = 2$ to 20 (i.e. disregarding the first realization), concentration matrix $c_{ij}(t_i)$ can be transformed into ${c_{ij}}^{\star}({t_i}^{\star})$, where ${t_i}^{\star} = t_i - t_0$ for $t_i \ge t_0$, and t_0 is the time origin of the transect.

For the reference transect (i.e. measurement location at $(x/H,\ z/H)_{\mathrm{ref}}$),

$$t_0 = \begin{cases} 0, \quad j = 2k+1, k = [1,\ 9] \quad S-N \\ 5, \quad j = 2k, k = [1,\ 10] \quad N-S \ . \end{cases} \tag{2.10}$$

For the sheltered transect (i.e. measurement location at $(x/H,\ z/H)_{\mathrm{lee}}$),

$$t_0 = \begin{cases} 5, \quad j = 2k+1, k = [1,\ 9] \quad S-N \\ 0, \quad j = 2k, k = [1,\ 10] \quad N-S \ . \end{cases} \tag{2.11}$$

After the transformation of $c_{ij}(t_i)$ to ${c_{ij}}^{\star}({t_i}^{\star})$, the concentration transient for each pass was set to incorporate a 115-second period instead of 120 second due to the 5-second lag between the reference and sheltered transect. The ensemble average of dust concentration transient for each field day can be approximated by

$$\langle c(t) \rangle \approx \frac{\sum_{j=2}^{j=20} {c_{ij}}^{\star}({t_i}^{\star})}{19}, \tag{2.12}$$

where $t_i = [0,\ 114]$ sec.

Scaled ensemble mean concentration transient Ensemble mean concentration transient at the same measurement location for different field days varied a lot in magnitude, which makes it difficult to seek general patterns of dust dispersion under similar atmospheric stability conditions (e.g. neutral stratification). Scaling methods can be applied to reduce the variability between different runs. When wind speed is fast, particles move more quickly and the residence time of particles

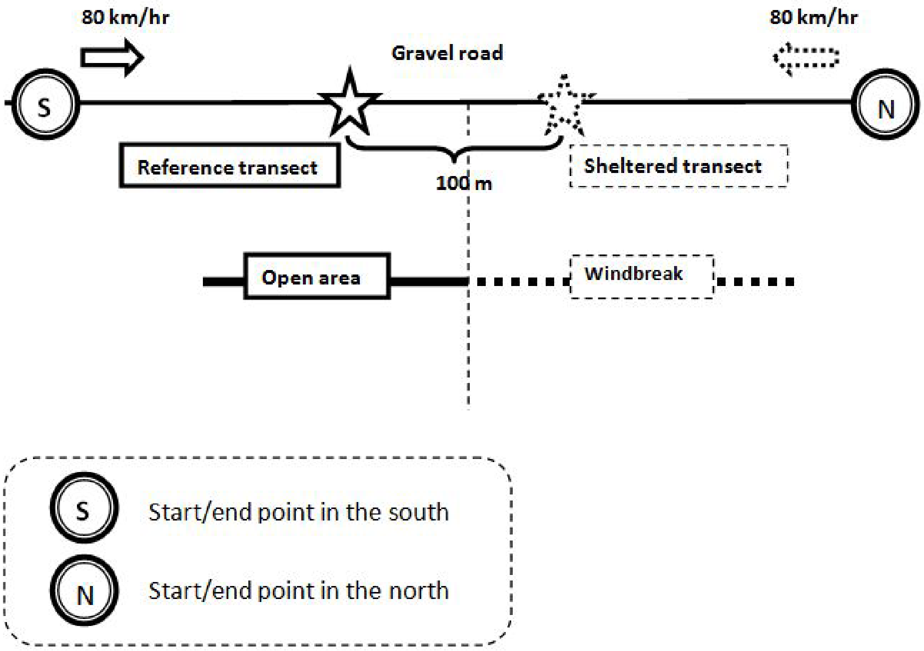

Figure 2.17: Field schematic for estimating time origin of Casella measurement at reference and sheltered transect

at downwind locations is reduced, which results in a sparse spatial distribution of dust particles and lower particle concentration; similarly, slow movement of dust particles resulting longer residence time (higher concentration) may be associated with low wind speed. For this reason, it is expected that higher wind speed is associated with lower concentration and vice versa, which implies the product $U_{\mathrm{ref}} \times \langle c \rangle$ is similar from run to run. The product can be normalized by a chosen reference concentration (c_{ref}) for each field day to minimize variabilities in concentration among different experimental runs. Moreover, the product $U_{\mathrm{ref}} \times t$ is similar from run to run because dust plumes arrive earlier when wind is fast (large U_{ref}) and vice versa. Therefore, the original plot of ensemble mean concentration vs. time can be scaled as follows. The ordinate is expressed as $U_{\mathrm{ref}} \langle c \rangle / c_{\mathrm{ref}}$, and the abscissa is expressed as $U_{\mathrm{ref}}\, t$. Ideally, U_{ref} is the speed of the upwind flow not disturbed by the windbreak; therefore, U_{ref} is chosen as the wind speed at $(-3,\ 1.2)_{\mathrm{ref}}$ (as shown in table 2.2). c_{ref} is chosen as the peak value of the ensemble dust concentration monitored at $(0.75,\ 0.2)_{\mathrm{ref}}$ for each field day. The resulting plots (Figures 2.26 and 2.27) will be shown and discussed in Section 2.3.3.

2.3 Results and discussion

2.3.1 Meteorological conditions

Table 2.2 summarizes the meteorological conditions for the five field days in summer 2011, based on measurements of the sonic anemometer placed at $(-3, 0.2)_{\text{ref}}$ where MOST applies (see Equation 2.2). Table 2.2 shows that the standard deviation of wind direction for the two neutral field days (Jul 27th and Aug 23rd) is much smaller than on the unstable field days. This reflects the known fact that wind direction is more consistent in a neutral surface layer, and the pattern of dust plumes resulted from transportation of gravel dust particles is more straightforward and simpler to interpret than any other atmospheric conditions. Therefore, dust concentration data for the two neutral field days (Jul 27th and Aug 23rd) are used as a preliminary exploration; in other words, this thesis focuses on field experiments conducted on Jul 27 and Aug 23.

The wind speed data (mean wind speed over each field experiment, i.e. 40 minutes) are summarized in Table 2.3 and Table 2.4. Figures 2.18 and 2.19 plot the horizontal mean wind speed at $z/H = 0.2$ and $z/H = 1.2$. It is expected that mean wind speeds should decrease downwind in the sheltered area, and remain constant in the unsheltered area where the wind field is (nominally) homogeneous. Consequently, the mean horizontal velocity of the sheltered downwind air flow is expected to be slower than that at matching positions in the unsheltered

	u_*	$u(-3,\ 1.2)_{\text{ref}}$	L	z_0	Stability	Θ	$\sigma\Theta$
Date	$\text{m}\,\text{s}^{-1}$	$\text{m}\,\text{s}^{-1}$	m	m		degree	degree
27/7/11	0.73	10.09	-184	0.0325	Neutral	225.0	15.9
4/8/11	0.45	4.72	-88	0.1075	Near Neutral	276.3	32.2
10/8/11	0.31	3.17	-18	0.0725	Unstable	295.9	57.8
17/8/11	0.28	3.41	-14	0.0275	Unstable	232.3	34.8
23/8/11	0.65	9.09	-106	0.0275	Neutral	282.5	14.1

Table 2.2: Summary of meteorological conditions (based on measurement by a 3D sonic anemometer placed at $(-3,\ 0.2)_{\text{ref}}$ on field days in 2011; Θ denotes the wind direction of upwind air flow; 0/360 degree indicates wind coming from north, and the reported wind directions are average values over each experimental period, approximately 40 minutes.

area. The measurements contradict that expectation, for they show that mean wind speed decreased with increasing x/H both in the sheltered area (as expected) and in the unsheltered area. This is probably because the alongroad span of the "unsheltered" (reference) area along the y-axis (see Figure 2.3) was not wide to assure the reference transect sampled truly ambient (unsheltered) winds.

	upwind x/H	x/H Sheltered		x/H Unsheltered		
Date	**-3**	**0.75**	**5**	**0.75**	**5**	**10**
27/7/11	7.26	4.56	2.19	7.39	6.29	5.31
4/8/11	3.11	1.98	0.79	3.39	2.78	2.41
10/8/11	2.29	1.17	0.73	2.13	1.19	NA
17/8/11	2.66	NA	1.14	NA	NA	NA
23/8/11	6.69	NA	1.94	NA	NA	NA

Table 2.3: Mean horizontal wind speed ($\text{m}\,\text{s}^{-1}$) measured at $z/H = 0.2$. Wind speed at $(-3, 0.2)_{\text{ref}}$ was measured by a sonic anemomenter, and at other locations, wind speeds were measured by cup anemometers. $x/H = 0$ indicates the position of the windbreak, and H is the height of the windbreak

	upwind x/H	**x/H Sheltered**			**x/H Unsheltered**		
Date	**-3**	**0.75**	**5**	**10**	**0.75**	**5**	**10**
27/7/11	10.09	7.42	7.31	7.47	10.10	9.69	13.15
4/8/11	4.72	3.59	3.32	3.41	4.75	3.61	4.13
10/8/11	3.17	3.21	2.82	3.08	3.42	2.58	3.04
17/8/11	3.41	NA	2.67	NA	NA	NA	NA
23/8/11	9.09	NA	6.34	NA	NA	NA	NA

Table 2.4: Mean horizontal wind speed ($\mathrm{m\,s^{-1}}$) measured at $z/H = 1.2$. Wind speed at $(-3, 1.2)_{\mathrm{ref}}$ was estimated by MOST (Equation 2.2), and at other locations, wind speeds were measured by cup anemometers. $x = 0$ indicates the position of the windbreak, and H is the height of the windbreak.

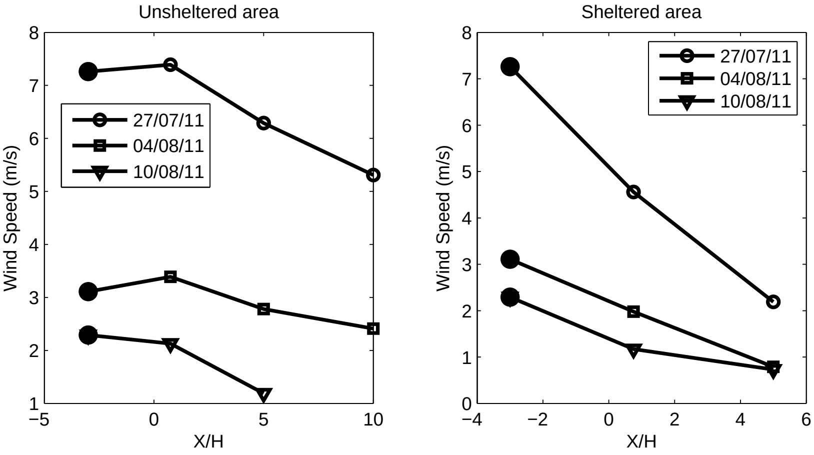

Figure 2.18: Mean horizontal wind speed at $z/H = 0.2$ at various downwind distances for different field days. The solid circles indicate wind speed measured by a sonic anemometer at $(-3,\ 0.2)_{\mathrm{ref}}$.

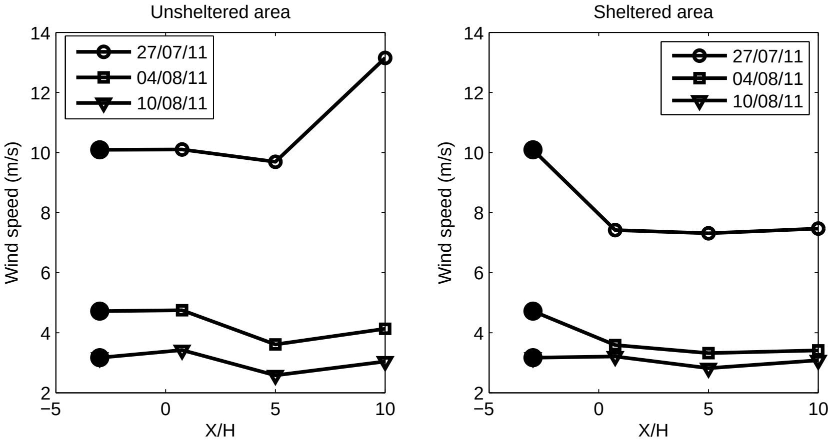

Figure 2.19: Mean horizontal wind speed at $z/H = 1.2$ height at various downwind distances for different field days. The solid circles indicate wind speed estimated by MOST at $(-3,\ 1.2)_{\text{ref}}$.

2.3.2 Time average concentration

On Jul 27th, Rotorod counters were placed at several downwind distances and at two heights ($z/H = 0.2, 1.2$) along the reference and sheltered transects. On Aug 23rd, Rotorod counters were placed at several downwind distances and at one height ($z/H = 0.2$). Ideally, the positions of Rotorod counters along the reference and sheltered transect should be matched; however, some problems occurred during the field experiments; for example, a few Rotorods' motors unexpectedly stopped operating, and some Rotorods were blown off by strong winds. Therefore, I only obtained a few viable pairs of concentration comparison between the reference and sheltered transect.

Measured time average concentrations for selected particle sizes are shown in Tables (2.5, 2.6, 2.7) and are displayed graphically on Figures

(2.20 and 2.21).

	x/H Unsheltered			x/H Sheltered		
D μm	**0.75**	**5**	**10**	**-1**	**0.75**	**5**
4	1.0E-04	1.0E-04	0.0E+00	2.0E-04	2.0E-04	1.0E-04
6	1.4E-02	1.2E-02	4.9E-03	1.5E-02	1.5E-02	1.4E-02
7	9.2E-03	7.7E-03	2.8E-03	9.1E-03	9.7E-03	8.2E-03
8	6.0E-03	5.3E-03	1.8E-03	5.8E-03	6.7E-03	5.5E-03
10	1.9E-03	1.7E-03	9.0E-04	2.0E-03	2.2E-03	2.2E-03
20	5.0E-04	7.0E-04	1.0E-04	7.0E-04	1.0E-03	4.0E-04
50	0.0E+00	8.0E-04	0.0E+00	0.0E+00	8.0E-04	7.0E-04

Table 2.5: **Jul 27th**: Measured time mean concentration by Rotorods in mg m^{-3} at $z/H = 0.2$ for selected particle sizes. The windbreak was located at $x = 0$. Dust was released from a gravel road at $x/H = -6$.

	x/H Unsheltered			x/H Sheltered			
D μm	**0.75**	**5**	**10**	**-1**	**0.75**	**5**	**10**
4	1.0E-04	1.0E-04	0.0E+00	1.0E-04	1.0E-04	1.0E-04	1.0E-04
6	1.0E-02	1.2E-02	6.1E-03	9.0E-03	1.1E-02	1.2E-02	1.1E-02
7	6.6E-03	7.8E-03	4.1E-03	6.0E-03	7.2E-03	7.0E-03	7.6E-03
8	4.6E-03	5.8E-03	3.1E-03	4.5E-03	4.9E-03	4.9E-03	5.3E-03
10	1.9E-03	2.0E-03	1.1E-03	2.0E-03	2.0E-03	1.8E-03	2.0E-03
20	8.0E-04	6.0E-04	5.0E-04	7.0E-04	7.0E-04	7.0E-04	7.0E-04
50	7.0E-04	0.0E+00	0.0E+00	0.0E+00	6.0E-04	7.0E-04	6.0E-04

Table 2.6: **Jul 27th**: Measured time mean concentration by Rotorods in mg m^{-3} at $z/H = 1.2$ for selected particle sizes. The windbreak was located at $x = 0$. Dust was released from a gravel road at $x/H = -6$.

It is evident that for each downwind measurement position, particles with diameters $5 \leq D \leq 10\,\mu$m were most abundant in the dust plume transported by the wind. At most downwind measurement positions, the time average concentration measured in the sheltered area was *larger* than at the matched position on the reference transect, and

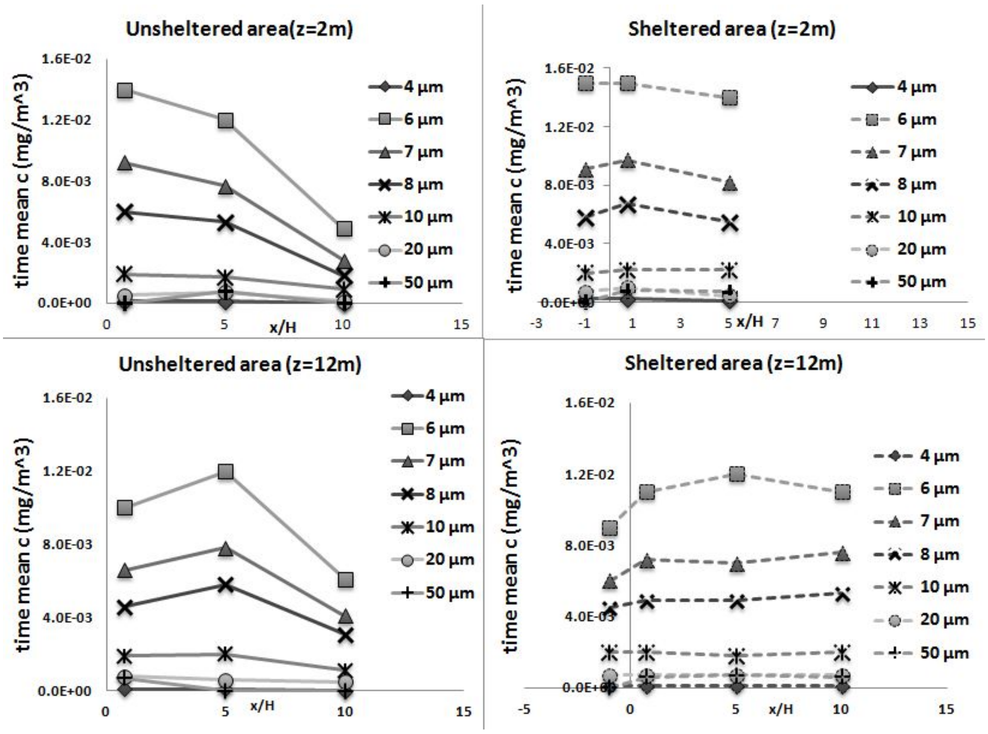

Figure 2.20: **Jul 27th**: Plot of size discriminated time average concentration from measurements of Rotorods at $z/H = 0.2$ (upper panel) and $z/H = 1.2$ (lower panel) vs. distance (scaled by the windbreak height $H = 10\,\mathrm{m}$) downwind of the source ($x/H = -6$) corresponding to Tables (2.5 and 2.6).

	x/H Unsheltered			x/H Sheltered			
D(μm)	**0.75**	**5**	**10**	**-1**	**0.75**	**5**	**10**
4	2.0E-04	2.0E-04	2.0E-04	1.0E-04	1.0E-04	1.0E-04	2.0E-04
6	1.3E-02	1.2E-02	1.0E-02	1.3E-02	1.4E-02	1.0E-02	1.1E-02
7	7.9E-03	7.8E-03	6.7E-03	8.3E-03	8.3E-03	6.7E-03	6.9E-03
8	5.3E-03	5.3E-03	4.4E-03	5.3E-03	5.9E-03	4.4E-03	4.8E-03
10	2.1E-03	1.9E-03	2.0E-03	2.1E-03	2.4E-03	1.8E-03	1.9E-03
20	9.0E-04	8.0E-04	1.0E-03	9.0E-04	7.0E-04	9.0E-04	1.0E-03
50	2.3E-03	0.0E+00	7.0E-04	2.3E-03	6.0E-04	7.0E-04	0.0E+00

Table 2.7: **Aug 23rd**: Measured time mean concentration by Rotorods in mg m^{-3} at $z/H = 0.2$ for selected particle sizes. The windbreak was located at $x = 0$. Dust was released from a gravel road at $x/H = -6$.

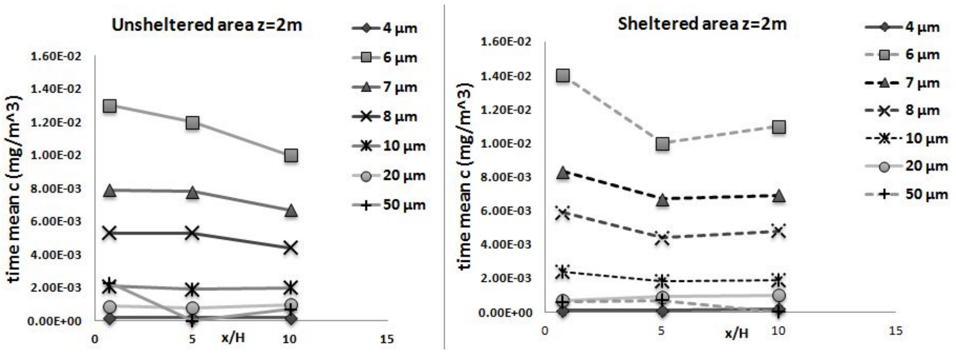

Figure 2.21: **Aug 23th**: Plot of size discriminated time average concentration from measurements of Rotorods at $z/H = 0.2$ vs. distance (scaled by the windbreak height $H = 10\,\mathrm{m}$) downwind of the source ($x/H = -6$) corresponding to table 2.7.

Figures (2.18, 2.19) show that the wind speeds in the sheltered area were slower than their matching positions in the unsheltered area. The plots of time mean concentration vs. distance (Figures 2.20 and 2.21) suggest that

(1) *at a given downwind location*, particle concentration varies with particle size

(2) particle concentration varies with measurement position for *particles with given size*

To address the first and second implication, time average concentration vs. particle diameter D_k at different downwind locations is plotted. Figure 2.22 shows the size distribution measured on Jul 27th. The plots for Aug 23 are very similar to that for Jul 27th. For clarity, I only present the plots of Jul 27th in this Chapter (the plot for Aug 23 is shown in Figure A.5 in Appendix A). Although the plots at different locations seem to be similar to each other, they do reveal some features of the concentration distribution, specifically:

(1) at any downwind location, concentration started to increase quickly for particles with diameters larger than $5\,\mu$m, and concentration peaked at $D = 6\,\mu$m. Concentration of particles larger than $10\,\mu$m decreased quickly but there was a tendency of rising concentration for particles of diameters larger than 50μm;

(2) at both heights ($z/H = 0.2$ and $z/H = 1.2$), in the unsheltered

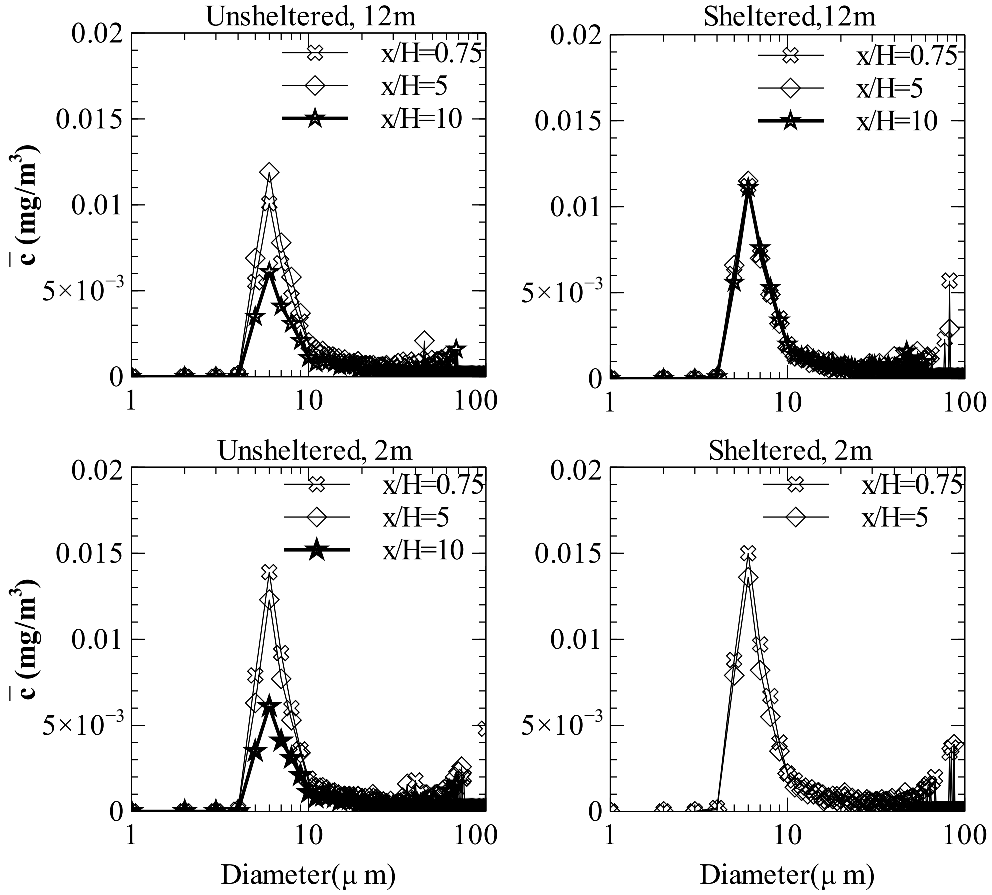

Figure 2.22: **Jul 27th**: Size distribution of concentration (mg m^{-3}) at (0.75/5/10, 0.2/1.2)$_{\mathrm{ref/lee}}$ along the reference and sheltered transect. The mass concentration corresponding to each diameter (D) is based on counting the number of particles whose diameter fall into $D - 0.5\,\mu\mathrm{m} < D < D + 0.5\,\mu\mathrm{m}$.

> area peak concentration measured at $x/H = 10$ was significantly lower than at the other two horizontal locations closer to the source. There was no significant difference between the concentrations measured at matching positions along the sheltered and reference transects, except for (10, 1.2) where the peak value was a lot higher along the sheltered transect. In general, time average concentration was higher in the sheltered area and at the lower height ($z/H = 0.2$) which was closer to the source of releasing; however, the difference was not striking.

By inspecting the size distribution of concentration, one can see that there was no shift in diameters of peak concentration at any location. In other words, particles of $6\,\mu$m (peak diameter) were abundant everywhere, but the question remains of how abundant were the $6\,\mu$m particles? (i.e. the percentage of $6\,\mu$m in the dust plume); besides the $6\,\mu$m particles, can one expect to detect particles of other sizes?; would the proportion of dust particles change as the dust plume travelled further downwind, and would the effects of the windbreak (i.e. disturbed wind field and entrapment function) change the proportion of the dust plume? To seek answers to these questions, an empirical probability density function (pdf) of dust concentration was constructed using

$$f(D_k) = \frac{\overline{c}_k}{\Delta D \sum_{i=1}^{100} \overline{c}_k}, \tag{2.13}$$

where $\overline{c}_k$ is the concentration of particles captured by the Rotorod counters belonging to the size range $D_k - 0.5 < D \leq D_k + 0.5$ during each field experiment (i.e. a period of 40 minutes). By definition, the probability that an airborne dust particle captured by the Rotorod at a specific downwind location has a diameter belonging to the range $(D1, D2]$ is

$$P(D1 < D \leq D2) = \int_{D1}^{D2} f(D_k)D_k.$$

Figure 2.23 shows the empirical pdf constructed by Equation 2.13 at $(0.75, 0.2/1.2)$, $(5, 0.2/1.2)$, $(10, 0.2/1.2)$ along the sheltered and reference transect.

There is no significant difference from location to location in the shape of pdf, so I did not use legends to distinguish the measurement locations. In fact, all of them are quite similar, which suggests that the proportion of particle sizes in the travelling dust plume didn't vary a lot. I surmise that dust particles of all sizes travelled at a similar speed in the field; in this way, no particle would lag behind the dust plume, thus the dust plume always retains the particles in the same proportions. Although deposition and windbreak entrapment were expected, movement of airborne dust particles was mainly driven by the prevailing wind, and no other forces exerted on dust particles were significant enough to influence the air flow; therefore, it is not surprising that all dust particles travel at a similar speed. In addition, by the definition of dust concentration pdf, the area under the curve of each measurement location can represent $P(1 < D \leq 100\,\mu\text{m})$ as marked on Fig 2.23.

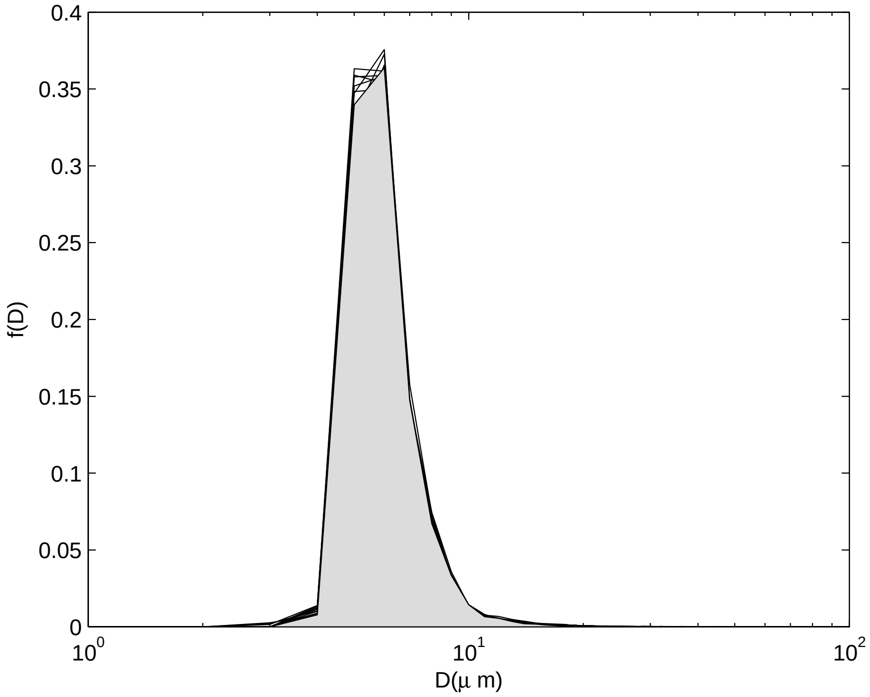

Figure 2.23: **Jul 27th**: Empirical pdf of c_k from measurements of Rotorods at $(0.75, 0.2/1.2)_{\mathrm{ref/lee}}$, $(5, 0.2/1.2)_{\mathrm{ref/lee}}$, $(10, 0.2/1.2)_{\mathrm{ref/lee}}$ along reference and sheltered transect respectively. The gray area indicated the probability of any particle in the dust plume belonging to the diameter range $[1\,\mu\mathrm{m}, 100\,\mu\mathrm{m}]$

2.3.3 Ensemble mean concentration transient

After background concentration had been zeroed and measurement errors had been corrected (as outlined in section 2.2.2, the ensemble average dust concentration transients as approximated by Equation 2.12 were computed, and are shown in Figures 2.24, 2.25 for the field experiments of Jul 27th and Aug 23rd. The corresponding scaled time series of ensemble concentration ($U_{\mathrm{ref}}\langle c\rangle/c_{\mathrm{ref}}$ vs. $U_{\mathrm{ref}}t$) are shown in Figures 2.26 and 2.27.

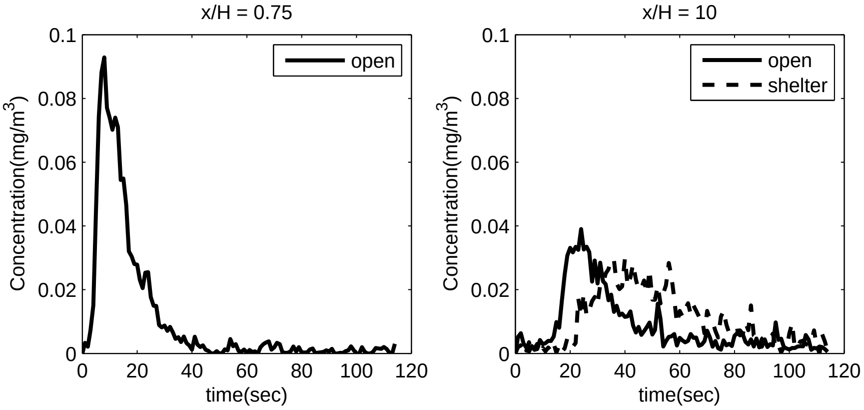

Figure 2.24: Unscaled time series of ensemble mean dust concentration on Jul 27. The horizontal measurement positions are shown on the plot. All Casella monitors were placed at the vertical height of $z = 2\,\mathrm{m}$. Measurement of ensemble mean dust concentration at $x/H = 0.75$ in the sheltered area was missing due to the malfunction of one of the Casella monitors on Jul 27.

Figures 2.24 to 2.27 reveal some features of the passage of dust plumes at the height of 2 m in the field regarding the comparison of the magnitude of peak concentration, its arrival time, and the duration of

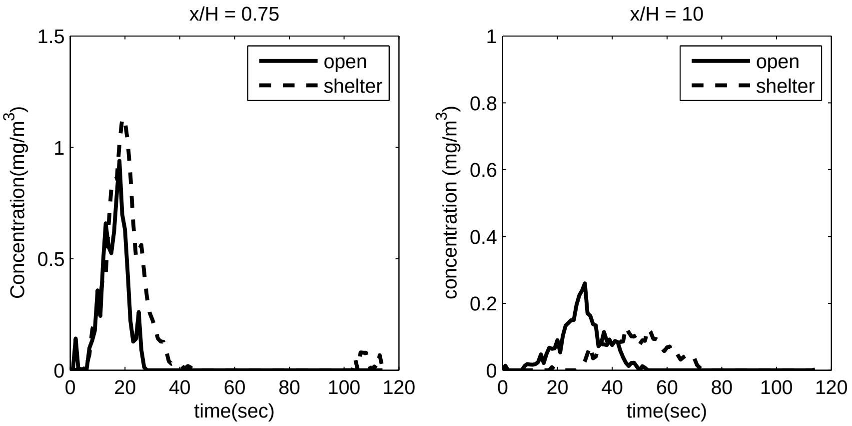

Figure 2.25: Unscaled time series of ensemble mean dust concentration on Aug 23. The horizontal measurement positions are shown on the plot. All Casella monitors were placed at the vertical height of $z = 2\,\mathrm{m}$.

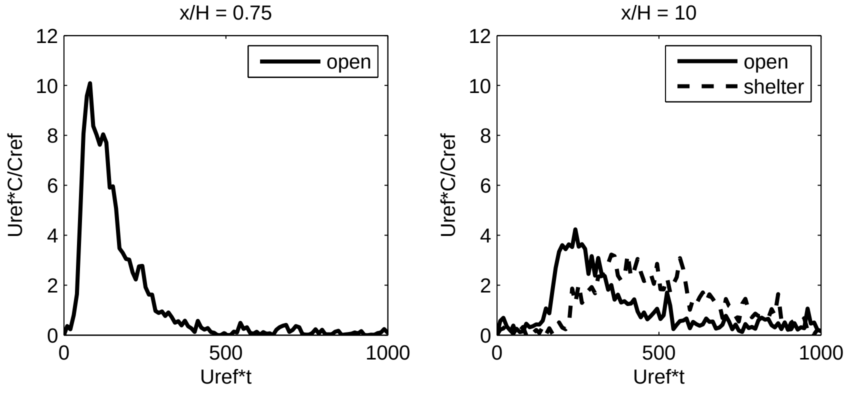

Figure 2.26: Scaled time series of ensemble dust concentration at $z = 2\,\mathrm{m}$ on **Jul 27**. $U_{\mathrm{ref}} = U(-3,\, 1.2)_{\mathrm{ref}}$ and $c_{\mathrm{ref}} = max(c(0.75,\, 0.2)_{\mathrm{ref}})$. The horizontal measurement positions are shown on the plot.

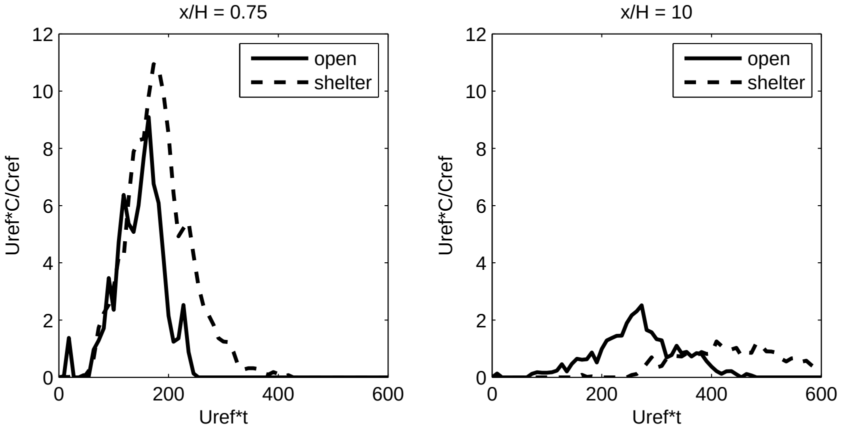

Figure 2.27: Scaled time series of ensemble dust concentration at $Z = 2\,\mathrm{m}$ on **Aug 23**. $U_{\mathrm{ref}} = U(-3,\, 1.2)_{\mathrm{ref}}$ and $c_{\mathrm{ref}} = max(c(0.75,\, 0.2)_{\mathrm{ref}})$. The horizontal measurement positions are shown on the plot.

dust plume passage which can be gauged by the width of the curves of ensemble average concentration transients.

Comparing matched locations along *reference* and *sheltered* transect At the farthest downwind location (i.e. $x/H = 10$), the peak concentration along the sheltered transect was lower than that at the matching position along the reference transect. The opposite occurred at the near downwind location $x/H = 0.75$. At all monitored locations, the concentration peak arrived later in the sheltered area, which is to be expected because the wind, the medium carrying dust particles, was slower in the lee of the windbreak. The width of the curve of ensemble mean concentration vs. time was wider in the sheltered area. This implies that it took more time for the dust plume to pass a downwind location along the sheltered transect than its matched location along the reference transect, another consequence of the reduced wind speed. Furthermore, there were more fluctuations shown in the ensemble concentration detected in the sheltered area, especially for locations further downwind (i.e at $x/H = 10$).

Comparing *near* downwind locations with *far* downwind locations The peak concentration occurred earlier in locations closer to the source, and the peak concentration at $x/H = 0.75$ was more than twice as large as that at $x/H = 10$. The fact that some dust particles (most likely large particles) had already deposited to ground by the time the dust plume arrived at a far downwind location may account for the lower peak concentration observed there. In addition, the duration of the dust plume was usually longer (wider curve) for locations further downwind (i.e. $x/H = 10$), and more flucutations in ensemble average concentration were observed. In short, further downwind locations didn't experience the abrupt change of dust concentration (sudden rise and drop) seen at near downwind locations, but there would be a prolonged passage of dust plumes at locations further downwind.

The data collected during the field experiments were not sufficient to unambiguously discern the effect of the natural windbreak on dust dispersion in the field. For example, it is unclear what causes the peak concentration detected in the sheltered area to be *higher* than that along the reference transect at $x/H = 0.75$, nor why the peak concentration at the far downwind location $x/H = 10$ is reduced in the sheltered area comparing to the matching location along the reference transect (see Figures 2.24 and 2.25). Intuitively, particle removal by windbreak entrapment and deposition may account for reduced peak concentration in the sheltered area; however, the effect of the disturbed wind field caused by the windbreak on dust dispersion is more difficult to explain intuitively. For this reason, a numerical model is needed to aid my investigation of the effects of the windbreak on dust dispersion. A Lagrangian stochastic model is developed for this purpose, which is the main topic of the next two Chapters.

Chapter 3

The Lagrangian stochastic (LS) model

The objective of the Indian Head dust dispersion experiments was to deduce the impact of a tree shelterbelt on the fate of dust lifting off a nearby gravel road (see Figure 2.3). To assist with the interpretation of the experiments, a Lagrangian stochastic (LS) particle trajectory model was adapted.

LS models are designed to compute the paths of fluid elements, or of particulates, in a *given* (or prescribed) turbulent flow — as defined in terms of its velocity statistics. Those statistics may be horizontally homogeneous, as (nominally) in the open region alongside the Indian Head shelterbelt, or disturbed (horizontally *in*homogeneous). From an ensemble of trajectories one may obtain a theoretical value $(\overline{c}/Q)^{LS}$ for the ratio of mean concentration (at any point) to the emission rate; the latter, so far as the experiments are concerned, was unknown. Then given measured $\overline{c}$ and theoretical $(\overline{c}/Q)^{LS}$, one may (for instance) infer a value for Q; and if the dust detector resolves particle size into classes (labelled k, say) then one may be able to estimate the emission rate Q_k in each of those size classes. Of interest here are two types of mean concentration: the size-differentiated concentration $\overline{c}_k = \overline{c}_k(x, y, z)$ provided by each of the Rotorods, which is an average over the entire 40 min of the experiment; and a size-aggregated, ensemble mean concentration transient $\langle c \rangle = \langle c \rangle(x, y, z, t)$ provided by each of the Casellas. The latter is obtained as the average over 19 vehicle passes (see Chapter 2), with suitable synchronization of the time origin so that the record commences when the vehicle was directly upwind from the transect in question.

Trajectories, representing particles from each of the observed size classes, were discretized into small time steps Δt (details follow below), and always terminated upon contact with the ground or when the particle had travelled more than 500 m away from the source (road). Particle deposition to the shelterbelt foliage was parameterized in terms of the particle Stokes number(St).

An LS trajectory model must be provided with (or "driven" by) the statistics of the ambient wind field, i.e. the components $\overline{u}_i$ of the mean wind, the Reynolds stress tensor $R_{ij} \equiv \overline{u'_i u'_j}$ (whose diagonal components are the turbulent velocity variances), and the turbulent kinetic energy dissipation rate ϵ. For the open (undisturbed) area velocity statistics were assumed to be described by the Monin-Obukhov similarity theory (MOST), which provides theoretical profiles allowing to extrapolate to all heights from the values measured by a single sonic anemometer. Trajectories along the transect through the shelterbelt were computed by an adaptation of the *gridded* LS model described by Wilson et al. (2009). The needed wind statistics were provided by a computation along the lines of Wilson (1985), i.e. a Reynolds-averaged Navier-Stokes (RANS) model driven by a momentum sink parameterizing the windbreak. The calculation used a second-order closure scheme, and provided flow statistics on a "grid".

This chapter focuses on the theoretical basis and implementation of the Lagrangian stochastic model.

3.1 Details of the LS model

3.1.1 Governing equations of the LS model

A first-order LS model can be utilized to model dispersion in the atmospheric surface layer where the Reynolds number of the motion is relatively high. Let $\mathbf{X} \equiv X_i(t)$ denote the position and $\mathbf{U} \equiv U_i(t) + \bar{u}_i$ the velocity of the moving particle, where $\bar{u}_i = \bar{u}_i(\mathbf{X})$ is the Eulerian mean velocity at the location of the particle. Assuming the evolution of $(\mathbf{X}, \mathbf{U})$ is a Markov process, the velocity increment over a time step dt is given by a generalized Langevin equation (Thomson 1987)

$$dU_i = a_i \left(\mathbf{X}, \mathbf{U}\right)\ dt +\ b_{ij}\ d\xi_j\ , \tag{3.1}$$

while the position increment is

$$dX_i = \left(U_i + \bar{u}_i\right)\, dt. \tag{3.2}$$

In Equation 3.1 $a_i\,dt$ is the deterministic part of the velocity increment, while $b_{ij}\,d\xi_j$ is a random increment, $d\xi_j$ being an increment of the Wiener process (with $\langle d\xi_j \rangle = 0$ and $\langle d\xi_i d\xi_j \rangle = dt\,\delta_{ij}$) and b_{ij} a scaling coefficient (Thomson 1987). If the moving particle is significantly heavier than the air it displaces, the effects of gravitational settling cannot be ignored. The simplest approach is to adopt the "settling sticky fluid element" (SSFE) model (Wilson 2000), which superimposes a constant gravitational settling velocity on the turbulent vertical velocity, and treats the ground as a perfectly absorbing surface (a suitable assumption for particles with large densities, such as loose and dry gravel dust). Therefore in order to model dust dispersion, Equation (3.2) has been modified to

$$dX_i = (U_i + \bar{u}_i - w_g\,\delta_{3i})\,dt. \tag{3.3}$$

It remains to specify the coefficients a_i, b_{ij}. The LS model must be consistent with inertial-subrange theory. For this reason, the choice of b_{ij} must ensure the model is consistent with the Kolmogorov similarity principle

$$\langle dU_i\,dU_j \rangle = C_0\,\epsilon\,dt\,\delta_{ij}, \tag{3.4}$$

where C_0 is a universal constant and $\epsilon = \epsilon(\mathbf{x})$ is the mean turbulent kinetic energy dissipation rate. It follows that

$$b_{ij} = \sqrt{C_0\epsilon}\,\delta_{ij}\ . \tag{3.5}$$

The deterministic coefficient of the acceleration ($\mathbf{a}$) is constrained by the well-mixed condition (Thomson 1987), viz. particles that are initially well-mixed (in position and velocity space) must remain so for all later times. This constraint links the specification of a_i to the probability density function (PDF) of the Eulerian velocity fluctuation. Suppose g denotes the joint PDF for the position and velocity of tracer particles, and g_a denotes the corresponding PDF for fluid elements. If the tracer particles are initially well-mixed, then g is initially proportional to g_a, and must remain so. By virtue of this constraint (i.e. the well-mixed equation) a_i can be determined from the Equations 9a and 9b in Thomson (1987) (i.e. Equations 3.6 and 3.7 below):

$$a_i\, g_a = \frac{\partial}{\partial u_j}(B_{ij}\, g_a) + \ \phi_i(\mathbf{x}, \mathbf{u}, t)\ , \tag{3.6}$$

$$\frac{\partial \phi_i}{\partial u_i} = -\frac{\partial g_a}{\partial t} - \frac{\partial}{\partial x_i}(u_i\, g_a)\ , \tag{3.7}$$

where $B_{ij} = (1/2)\, b_{ik}\, b_{jk} = (1/2)\, C_0\, \epsilon\, \delta_{ij}$ (the lower case position and velocity coordinates used above are the axes of position-velocity phase space).

We assume the Eulerian velocity-fluctuation PDF is Gaussian

$$g_a(u') = \frac{\sqrt{detR^{-1}}}{2\pi^{3/2}} \exp[-\frac{1}{2}\, {u'}_i\, {R_{ij}}^{-1}\, {u'}_j]\ , \tag{3.8}$$

where the Reynolds stress tensor R_{ij} is time-independent (the flow is stationary). In the open (unsheltered) region R_{ij} is *vertically* inhomogeneous but constant on horizontal planes, while around the windbreak it varies with both the vertical and the alongwind (x) coordinates.

Thomson (1987) gave one particular well-mixed LS model that is consistent with the Gaussian PDF, a model which can be expressed in the form (Wilson et al. 2009)

$$a_i = T_i^0 + T_{ij}^1\, U_j + T_{ijk}^2\, U_j\, U_k\ , \tag{3.9}$$

where

$$T_i^0 = \frac{1}{2}\frac{\partial R_{il}}{\partial x_l}\ , \tag{3.10}$$

$$T_{ijk}^2 = \frac{1}{2}{R_{lj}}^{-1}\frac{\partial R_{il}}{\partial x_k}\ , \tag{3.11}$$

$$T_{ij}^1 = -\frac{1}{2}C_0\epsilon {R_{ij}}^{-1} + T_{ijk}^2\, \bar{u}_k\ . \tag{3.12}$$

Note that this model is quadratic in the velocity fluctuation, and that the coefficients (the T's) can be calculated in advance and stored on the grid.

3.1.2 Velocity autocorrelation time scale and time step

For a first-order LS model, the time step Δt must be chosen to ensure that the simulation resolves the evolution in velocity and position over Δt without the need to explicitly model fluid element acceleration. Therefore, Δt must satisfy $\Delta t \ll T_L$, where T_L is the Lagrangian time scale measuring typical temporal persistence of the turbulent velocity. T_L can be related to the earlier coefficient $b = \sqrt{C_0\epsilon}$ by the following formula (Tennekes 1979)

$$T_L = \frac{{\sigma_w}^2}{C_0\epsilon}\ , \tag{3.13}$$

where (recall) C_0 is the Kolmogorov constant.

However the velocity correlation along the trajectory traced by a heavy particle should be reduced relative to that along the path of a fluid element. Following Sawford & Guest (1991) the velocity autocorrelation timescale Γ_p for a heavy particle trajectory was assumed to be

$$\Gamma_p = \frac{T_L}{\sqrt{1 + (\frac{\beta w_g}{\sigma})}} \ , \tag{3.14}$$

where β is an empirical dimensionless constant. The LS model for this thesis adopted $\beta \approx 2$ following Wilson's (2000) study of trajectory models for heavy particles in surface layer turbulence. Wilson demonstrated that with $\beta \approx 2$, the LS model estimated the location and width of the deposition swath (of glass beads released from a continuous elevated point source) very well.

3.1.3 Tuning the LS model by specifying C_0

Although in principle C_0 is a universal constant, in practice its value is adjusted to "tune" the LS model so as to reproduce an optimal value for an effective turbulent Schmidt number, i.e. ratio $Sc = \nu_T/K$ of the eddy viscosity to the eddy diffusivity. According to Sawford & Guest (1988), the diffusion limit of Thomson's multidimensional LS model for Gaussian turbulence implies the eddy diffusivity can be expressed as

$$K = \frac{2({\sigma_w}^4 + {u_*}^4)}{C_0 \epsilon} \ , \tag{3.15}$$

assuming the TKE dissipation rate $\epsilon = {u_*}^3/(k_v \, z)$ for local equilibrium in the neutral surface layer (NSL). The eddy diffusivity in the 'far field'

($t \gg T_L$) can be related to an effective Lagrangian time scale T_L by $K = {\sigma_w}^2 T_L$. In the NSL, T_L can be parameterized as $T_L = aZ/\sigma_w$, and the eddy diffusivity K can be written as

$$K = a\sigma_w z, \tag{3.16}$$

where a is an empirical coefficient. By Equation 3.15, the relation between C_0 and a is

$$C_0 = \frac{2k_v}{a} \frac{{c_w}^4 + 1}{c_w} \,, \tag{3.17}$$

where $c_w = \sigma_w/u_*$. In a neutral atmosphere, σ_w can be expressed as $1.25u_*$ or $1.3u_*$ (Kaimal & Finnigan 1994; Wilson 2008), and the eddy viscosity can be expressed as $\nu_T = k_v u_* z$. By definition of S_c one then has the eddy diffusivity as

$$K = \frac{1}{S_c} k_v u_* z. \tag{3.18}$$

Equations 3.16 and 3.18 relate the empirical coefficient a to the Schmidt number Sc. In other words, a implies Sc, and C_0 can be estimated by Equation 3.17. For this reason, C_0 can be obtained by calibrating the model against observations. The Project Prairie Grass (PPG) short range tracer dispersion trials (Barad 1958; Haugen 1959), conducted in a flat, open area under a wide range of stability conditions, are regarded as suitable observations to tune LS models. Wilson et al. (1981) recommended $a \approx 0.5$ (implying $S_c \approx 0.63$) for best agreement with the PPG trials. Given that in the NSL $c_w = 1.25$ or 1.3, it follows from Equation 3.17 that $C_0 \approx 4.4$ or 4.8. To specify C_0 for this project, measured $\overline{c}/Q$ at different heights for PPG Run 57 (neutral stratification) were compared with modeled $\overline{c}/Q$ using differing values of C_0. The value $C_0 = 4.3$ produced the closest match to observations (see Figure 3.1), and was adopted for this study.

3.2 Implementation of the LS model

The implementation of the 3-D first-order LS model for this project is based on the version of urbanLS documented by Wilson et al. (2009) in their simulation of wind transport in the urban environment.

3.2.1 Numerical grid

A 3-D grid is constructed using Cartesian coordinates: the positive x-axis points eastwards, the positive y-axis points northwards, and the positive z-axis points upwards (see Figure 2.3). Space is subdivided into control volumes (cv), whose centres are labelled (x(ic), y(jc), z(kc)). Faces of control volumes lie midway between the nodes of adjacent control volumes. The numerical grid spans the region $-180\,\mathrm{m} \leq x \leq 1190\,\mathrm{m}$ in the along-wind direction and $0\,\mathrm{m} \leq z \leq 415\,\mathrm{m}$ in the vertical direction; it is assumed that symmetry prevails in the cross-wind (y) direction in the unsheltered area and sheltered area respectively, so that the ability of the model to discriminate gradients along y is not called into action. The streamwise resolution of the numerical grid was uniformly $\Delta x = 10\,\mathrm{m}$; vertical resolution was constant at $\Delta z \approx 0.5\,\mathrm{m}$

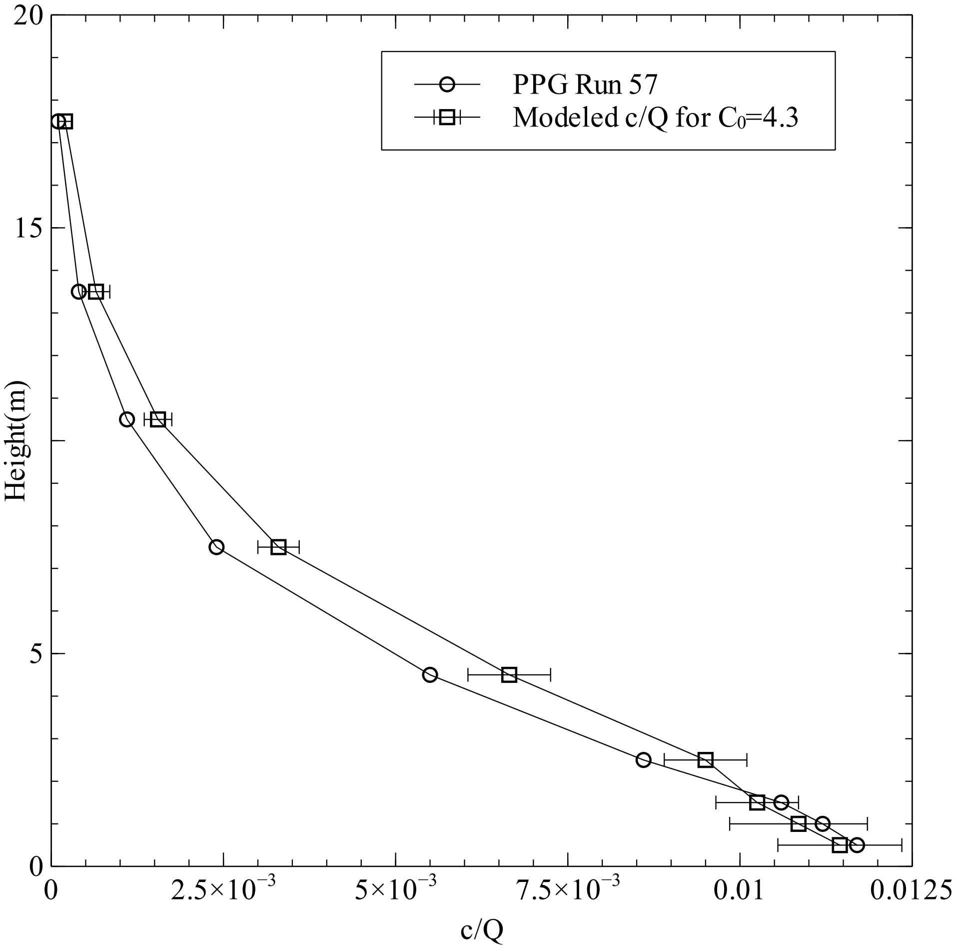

Figure 3.1: Vertical profiles of normalized mean, crosswind-integrated concentration $\overline{c}/Q$ at a radial distance of 100 m from a continuous near ground point source: comparison of an LS simulation (with $C_0 = 4.3$) with measured values from Project Prairie Grass Run 57 (neutral atmosphere: $L = -239$ m, $u_* = 0.5\,\mathrm{m\,s^{-1}}$, $z_0 = 0.0058$ m).

for $z \leq 20\,\mathrm{m}$, and gently coarsened above 20 m.

After velocity statistics at each cv center are read from the flow calculation (or computed by MOST), one can use Equations (3.10-3.12) to calculate, at each control volume center, the values of T^0, T^1, and T^2. For each time step of a particle trajectory, the model calculates a_i and b_{ij} using the (pre-calculated) T values and stored values for wind statistics (namely, $\overline{u}_i$ and ϵ) appropriate to the centre of cv presently occupied by the particle. Following Wilson et al. (2009), the T's (and wind statistics) are not interpolated to the particle's exact position, for as argued by Wilson et al. there is no evidence to suggest that the accuracy of the model is improved by adopting a computationally intensive interpolation scheme.

3.2.2 Wind field

The trajectory of a single particle simulated by the LS model is driven by the statistics of the ambient wind field; therefore, all components of the mean wind $\overline{u}_i$ and of the Reynolds stress tensor $\overline{u'_i u'_j}$ as well as the turbulent kinetic energy dissipation rate ϵ, at the center of each cv are essential inputs to the LS model. In the absence of any flow disturbance in the unsheltered area, i.e. if the surface layer is horizontally homogeneous, the needed wind statistics can be calculated using the Monin-Obukhov similarity theory (MOST). On the other hand in the area sheltered by the windbreak, wind statistics (obviously) are horizontally **in**homogeneous and so MOST does not apply. The needed 3-D wind statistics were supplied by a RANS wind flow model (whose inflow velocity statistics were matched to the observations). The approach taken was to make the simulated mean wind transect at $z/H = 0.2$ match the few measured wind data along that line, by tuning the value of the effective resistance coefficient (k_r) representing the shelterbelt in the RANS calculation; $k_r = 2.5$ was adopted becasue it produces optimal fitting of simulation with measurments at $z/H = 0.2$; in this way, one obtained a reasonable approximation of the ambient mean velocity as the basis for simulating particle trajectories (Figure 3.2).

Simulation of the disturbed airflow in the sheltered area under neutral stratification and under the condition of a perpendicular mean wind requires the specification of only two inputs: the ratio of the windbreak height to the surface roughness length (H/z_0), and the effective resistance coefficient (k_r) mentioned above.

Figure 3.3 shows the mean wind fields adopted for the unsheltered and sheltered areas, respectively. The salient features of the disturbed mean flow are:

1. mean streamline curvature of the air flow near the shelterbelt, concave upwards upwind of the windbreak and concave downwards downwind, is due to a fraction of the oncoming mass flux of air being forced to flow over the top of the windbreak; the increased wind speed aloft forms a jet, associated with streamline compression.

2. below the height of the windbreak, the mean wind speed is reduced significantly in the region $0 \leq x/H \leq 10$.

3. the region of strong reduction in mean velocity extends to about $x/H = 10$, although the mean wind profile does not recover fully even as far downwind as $x/H = 15$.

Turning now to the provision of *turbulence* fields to the LS model, the lower panel of Figure 3.4 shows how the turbulence (as characterized by the variance of vertical velocity, ${\sigma_w}^2$) varies with position along a transect through the windbreak at $z/H = 0.2$. The reduction in the immediate lee below the height of the windbreak and the enhanced turbulence in the wake region are evident. The reduced turbulence in the immediate lee ("quiet zone") is probably due to an enhanced TKE dissipation rate, for (Wilson 1985) the small scale TKE generated near the windbreak dissipates rapidly. On the other hand, ${\sigma_w}^2$ increases by more than 50% in the wake region, courtesy of strong wind shear. Thus the RANS model provides turbulence fields to the LS model that are at least qualitatively consistent with what are believed to be the dominant effects.

3.2.3 Entrapment parameterization

Besides disturbing the upwind airflow, a natural windbreak is also capable of filtering dust particles; that is, some fraction of the impinging dust particles may deposit onto vegetation elements (this is known as "entrapment") as the dust-laden air flow passes through the windbreak. Raupach et al. (2001) give a comprehensive review of particle entrap-

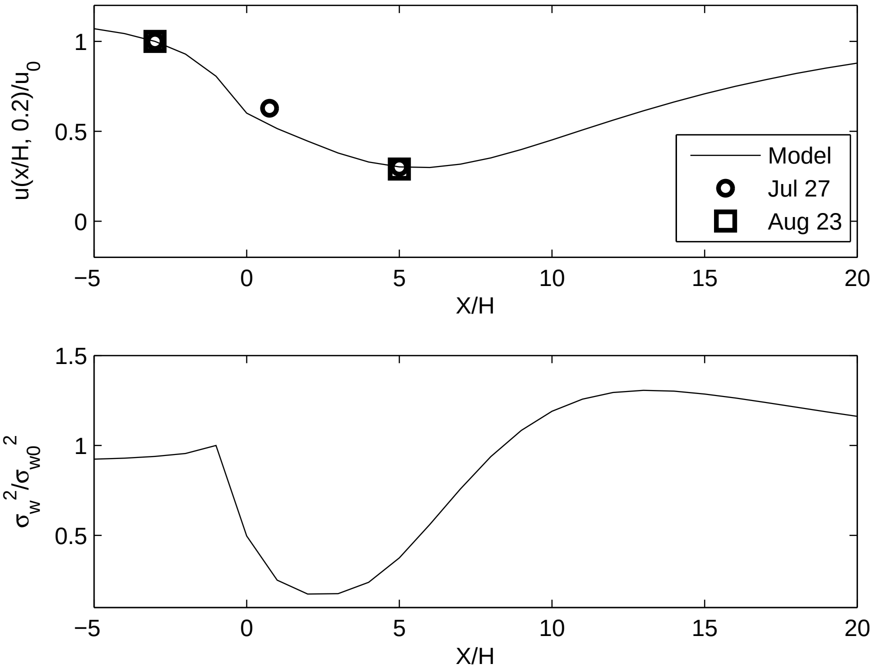

Figure 3.2: RANS simulation of the relative mean wind speed curve and of the normalized vertical velocity variance ${\sigma_w}^2/{\sigma_{w0}}^2$ along a transect at $z/H = 0.2$ through a shelterbelt; wind speed and vertical velocity variance at $z/H = 0.2$ of undisturbed (homogeneous) flow are labelled u_0 and ${\sigma_{w0}}^2$. The RANS model assumes neutral stratification and that the mean wind is perpendicular to the windbreak, and used the measured value for the ratio H/z_0 of windbreak height to surface roughness length, i.e. $H/z_0 = 200$. The resistance coefficient k_r was treated as a tuning parameter, and the profiles shown are for $k_r = 4.5$. The computational resolution is $(\Delta x/H, \Delta z/H) = (1, 0.2)$.

ment by thin windbreaks (see Section 1.3.2), and this was extended by Wilson (2005). The entrapment parameterization for the present LS model is based on the approach of Raupach et al. who stated that

"in a Lagrangian or fluid following reference frame, the particle

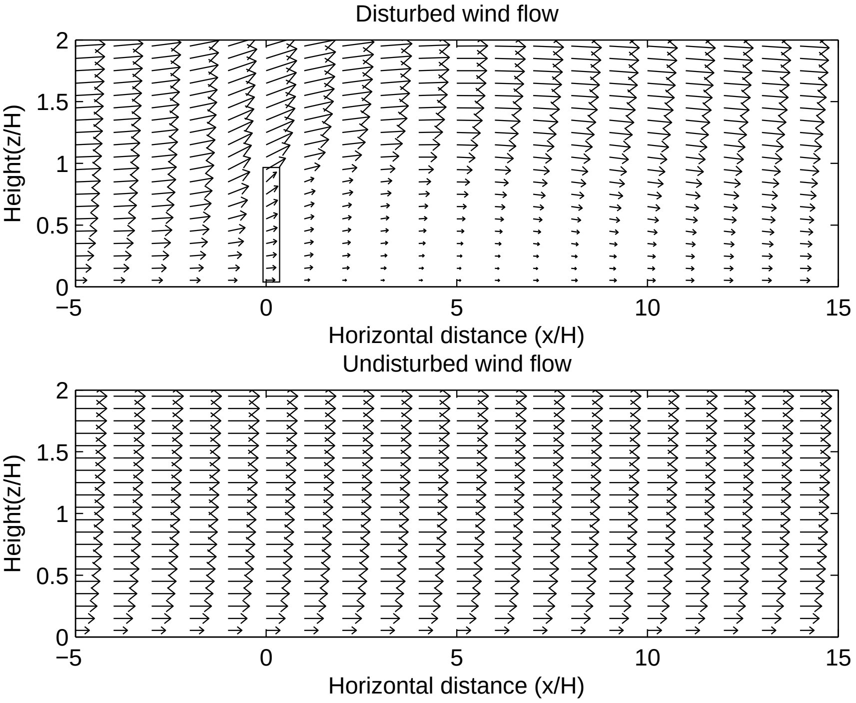

Figure 3.3: Comparing the mean wind field around the windbreak (upper panel), as simulated by the RANS model, with the wind field in the homogeneous area as represented by the (laterally-unvarying) MOST profile (lower panel). These fields are representative for neutral stratification with the mean wind perpendicular to the shelterbelt. The windbreak, outlined by the black rectangle, is centred on $x/H = 0$, and the height of the windbreak (H) is 10 m.

concentration c (particles m^{-3}) is governed by

$$\frac{dc}{dt} = -\alpha\, g_p\, c\ , \tag{3.19}$$

where α is the frontal area density of the windbreak elements."

After some manipulation, one may show that

$$\frac{dc}{c} = -\,\alpha\, \frac{g_p}{U}\, dx\ , \tag{3.20}$$

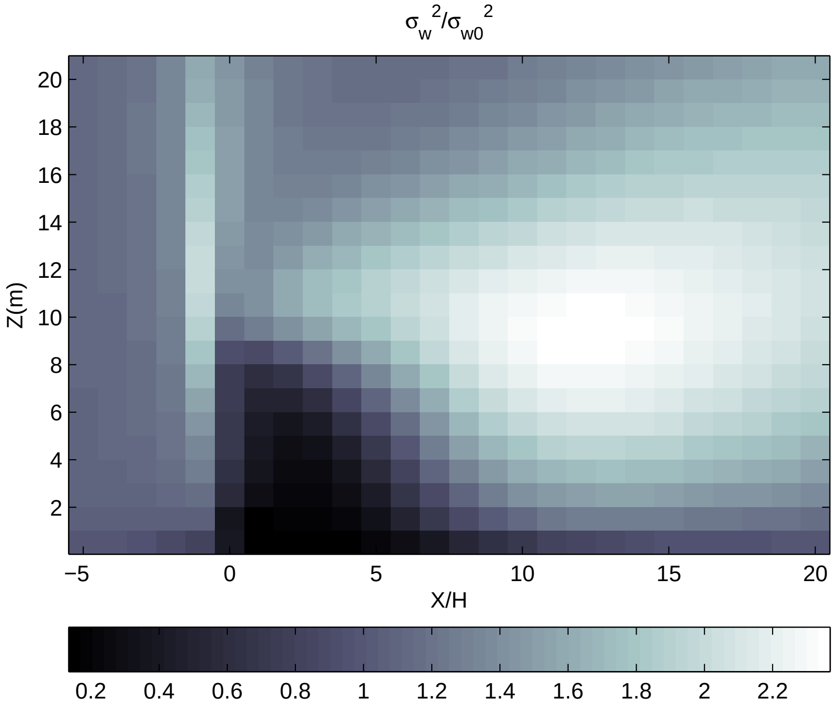

Figure 3.4: Modeled field of vertical velocity variance ${\sigma_w}^2$ normalized by ${\sigma_{w0}}^2$ of the undisturbed homogeneous flow, for neutral stratification and perpendicular wind incidence. The windbreak is centred on $x/H = 0$, and the height of the windbreak (H) is 10 m.

i.e. the fractional change of concentration during the distance step dx corresponding to each time step is related to the dimensionless deposition conductance g_p/U. In the present context (i.e. for the experiment conducted at Indian Head) Brownian diffusion can be neglected, because the majority of dust particles detected were larger than 1μm in diameter. That being the case g_p/U can be parameterized by the Stokes number (see Equations. 1.20 and 1.21).

In terms of actual implementation, entrapment in the LS model worked as follows. Whereas the RANS model supplying the wind statistics neglected the alongwind extension (i.e. width) of the shelterbelt along x-axis, that extension was resolved in the LS model. For each distance step dx occurring within the shelterbelt the value of g_p/U was computed, and if larger than a threshold probability the particle was deposited to the windbreak and the trajectory terminated. Figure 3.5 shows how probability of entrapment denoted by deposition conductance g_p/U changes as particle size increases. Generally speaking, larger particles are more likely to deposit onto foliage than smaller particles.

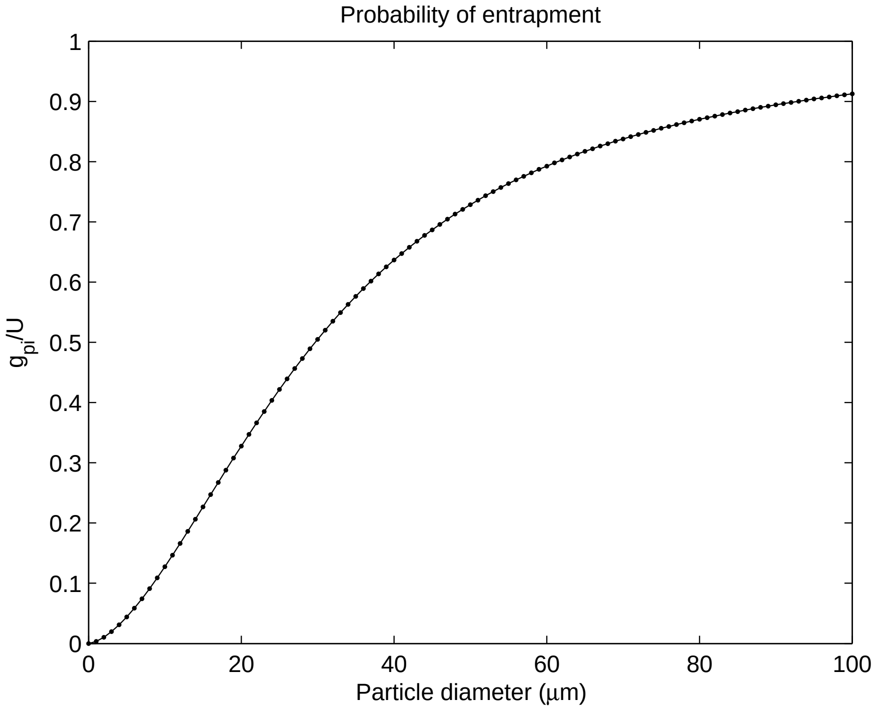

Figure 3.5: Normalized impaction conductance g_{pi}/U versus particle diameter, assuming the characteristic length for a typical foliage element is 0.05 m.

Chapter 4

Modeling particle dispersion

The LS model was run for a number of particle size classes, but here three representative size classes have been selected in order to produce the modelling results of Section 4.2, namely: "small" particles ($D = 6\,\mu$m), "medium" particles ($D = 50\,\mu$m) and "heavy" particles ($D = 100\,\mu$m). Simulations of particle motion, in both the unsheltered and the sheltered areas, have been configured to the conditions of the two experiments at Indian Head that were conducted under effectively neutral stratification, i.e. Jul 27th and Aug 23rd. Parameters specified for these model runs were the meteorological inputs (u_*, z_0), the windbreak dimensions, and the characteristics of the dust particles (i.e. diameter, gravitational settling velocity and density). Each simulation entailed the computation of an ensemble of 15000 particle trajectories, subdivided as 15 sub-ensembles each of 1000 particles. As the gravel road of the Indian Head experiments lay 60 m west of the windbreak, and as the origin of the x-axis had been chosen so as to align with the centre of the windbreak, in simulations particles were released in the locality of $x = -60\,\mathrm{m}$ (i.e. upstream) and at the y coordinate corresponding to the chosen transect (open or sheltered). This chapter focuses on the analysis of modeled results.

4.1 Theoretical basis for analysis of model output

The purpose of the LS model is to simulate the trajectories of a large number of particles released at the source, and deduce quantities pertinent to dust dispersion pattern, such as time average concentration over a chosen period (in practice, the first 60 s after release into the flow), ensemble average concentration transient, and deposition rate.

4.1.1 Initial size of the dust puff

For these simulations it was assumed that at the moment ("$t = 0$") of passing upwind of one or the other of the instrumented transects, the vehicle travelling along the gravel road would have produced puff of dust having a finite extension along the x and z axes, assuming symmetry along the y axis. In simulations the finite initial width was modelled by originating any given single trajectory at a point chosen at random within an area defined by $-60 - \delta_{xs}/2 \leq x \leq -60 + \delta_{xs}/2$, $z_0 \leq z \leq \delta_{zs}$, i.e. trajectory start points were uniformly distributed within those bounds. There are no obvious constraints on the choice of δ_{xs} and δ_{zs}, however, it seems reasonable to assume that the dimension of the initial dust puff should be limited to (at most) the width of the road and the height of the truck. The gravel road in the field was not wider than 10 m and the height of the truck was less than 2 m. I have tested the following choices for δ_{xs} and δ_{zs}:

(a) $\delta_{xs} = 0$, and $\delta_{zs} = z_0$, i.e. no initial spread

(b) $\delta_{xs} = 3$ m, and $\delta_{zs} = z_0$, i.e. initial trajectory points were uniformly spread in along-wind direction within $-61.5 \leq x \leq -58.5$ m, but all released at the surface

(c) $\delta_{xs} = 0$, and $\delta_{zs} = 1.5$ m, i.e. initial trajectory points were uniformly spread in vertical direction within $z_0 \leq z \leq 1.5$ m, but all released at the center of the gravel road $x = -60$ m

(d) $\delta_{xs} = 0$, and $\delta_{zs} = 2$ m, i.e. initial trajectory points were uniformly spread in vertical direction within $z_0 \leq z \leq 2$ m, but all released at the center of the gravel road $x = -60$ m

(e) $\delta_{xs} = 3$ m, and $\delta_{zs} = 1.5$ m, i.e. initial trajectory points were uniformly spread in the region bounded by $-61.5 \leq x \leq -58.5$ m and $z_0 \leq z \leq 1.5$ m

(f) $\delta_{xs} = 6$ m, and $\delta_{zs} = 1.5$ m, i.e. initial trajectory points were uniformly spread in the region bounded by $-63 \leq x \leq -57$ m and $z_0 \leq z \leq 1.5$ m

(g) $\delta_{xs} = 1$ m, and $\delta_{zs} = 2$ m, i.e. initial trajectory points were uniformly spread in the region bounded by $-60.5 \leq x \leq -59.5$ m and $z_0 \leq z \leq 2$ m

(h) $\delta_{xs} = 1$ m, and $\delta_{zs} = 1$ m, i.e. initial trajectory points were uniformly spread in the region bounded by $-60.5 \leq x \leq -59.5$ m and $z_0 \leq z \leq 1$ m

I have selected as "best choice" the alternative (amongst a to h) that results in the simulation of $\overline{c}/Q$ that best reflects the pattern of the mean concentration $\overline{c}$ measured by the Rotorods. To simplify the process of comparison, I only compare simulated $\overline{c}/Q$ with measured $\overline{c}$ for particles of size $6\,\mu$m, the most abundant particle size detected by Rotorod measurements in the field. Measured concentration $\overline{c}$ cannot be directly compared to simulated concentration normalized by source strength $\overline{c}/Q$; however, it is evident that the ratio of $\overline{c}(\xi_1, \zeta_1)$ to $\overline{c}(\xi_2, \zeta_2)$ should be the same as the ratio of $\overline{c}(\xi_1, \zeta_1)/Q$ to $\overline{c}(\xi_2, \zeta_2)/Q$ along the same measurement transects (reference or sheltered) for particles of the same size (i.e Q is invariant); assume $\xi = x/H$, and $\zeta = z/H$. Therefore, I choose the position $(0.75, 0.2)_{\mathrm{ref}}$ as a reference location, which is an arbitrary choice and is labeled as '0', and calculate the ratio of measured concentration ($\overline{c}_i$) of any other location labeled by a number i to that of the reference location ($\overline{c}_0$) as shown in Table 4.1, and then repeat the calculation for simulated $\overline{c}/Q$ at the same monitoring locations.

The choice of δ_{xs} and δ_{zs} is determined based on the comparison of the ratio of measured $\overline{c}_i/\overline{c}_0$ in Table 4.1 with the ratio of simulated $\frac{\overline{c}_i}{Q}/\frac{\overline{c}_0}{Q}$, where the subscript i stands for the label of monitoring locations as shown in Table 4.1, and '0' indicates the reference location $(0.75, 0.2)_{\mathrm{ref}}$. Table 4.2 shows modeled $\overline{c}_i/Q$ from simulations using the alternative assumptions as to initial puff size, and Table 4.3 shows the corresponding $\frac{\overline{c}_i}{Q}/\frac{\overline{c}_0}{Q}$ and compares them with measured $\overline{c}_i/\overline{c}_0$.

i	Position $(x/H, z/H)$	$\overline{c}\,(\mathrm{number\,m^{-3}})$	$\overline{c}_i/\overline{c}_0$
0	$(0.75, 0.2)_{\mathrm{ref}}$	80902	1.00
1	$(5, 0.2)_{\mathrm{ref}}$	71284	0.88
2	$(10, 0.2)_{\mathrm{ref}}$	28411	0.35
3	$(0.75, 0.2)_{\mathrm{lee}}$	86983	1.08
4	$(5, 0.2)_{\mathrm{lee}}$	78955	0.98

Table 4.1: Measured concentration (field day: Jul 27th) in number m^{-3} for particles of 6 μm diameter at locations labeled 0 to 4. The final column gives ratios of measured concentration, taking location 0, i.e. $(0.75, 0.2)_{\mathrm{ref}}$, as the reference.

i	(a)	(b)	(c)	(d)	(e)	(f)	(g)	(h)
0	1.7E-03	1.7E-03	8.4E-03	9.7E-03	8.5E-03	7.7E-03	1.0E-02	7.1E-03
1	9.2E-04	9.1E-04	4.8E-03	5.9E-03	4.7E-03	4.6E-03	5.9E-03	3.6E-03
2	7.9E-04	7.1E-04	3.0E-03	3.7E-03	3.3E-03	3.2E-03	3.7E-03	2.3E-03
3	1.1E-03	1.2E-03	1.2E-02	1.3E-02	1.1E-02	1.2E-02	1.4E-02	9.4E-03
4	1.6E-04	6.1E-04	8.6E-03	8.3E-03	8.3E-03	8.9E-03	8.3E-03	6.9E-03

Table 4.2: Modeled $\overline{c}/Q$ for locations $i = 0$ to 4, corresponding to the choices (a) to (h) for the spatial distribution of trajectory start points. Simulations for a neutral atmosphere, and particle diameter 6μm.

It is reasonable to assume that the closer the simulated $\frac{\overline{c}_i}{Q}/\frac{\overline{c}_0}{Q}$ to measured $\overline{c}_i/\overline{c}_0$, the better the simulated $\overline{c}/Q$ reflects the pattern of

i	measured c_i/c_0	(a)	(b)	(c)	(d)	(e)	(f)	(g)	(h)
0	**1.00**	1.00	1.00	1.00	1.00	1.00	1.00	1.00	1.00
1	**0.88**	0.54	0.54	0.56	0.61	0.55	0.59	0.59	0.50
2	**0.35**	0.46	0.42	0.35	0.38	0.39	0.41	0.37	0.32
3	**1.08**	0.62	0.74	1.41	1.36	1.28	1.53	1.36	1.34
4	**0.98**	0.09	0.37	1.03	0.86	0.98	1.16	0.83	0.98

Table 4.3: Comparing measured c_i/c_0 (second column) with simulated ratios $\frac{c_i}{Q}/\frac{c_0}{Q}$ for different spatial distributions of trajectory start points (a to h).

the measured $\overline{c}$ by Rotorods, and the better the corresponding spatial distribution of starting trajectory points. The degree of closeness at all interesting locations will be judged by calculating the sum of squared residuals (SSR). Let r_i denote the ratio $\overline{c}_i/\overline{c}_0$ and let $\hat{r}_i$ be the simulated ratio $\frac{\overline{c}_i}{Q}/\frac{\overline{c}_0}{Q}$. Then

$$\mathrm{SSR} = \sum_{0}^{4} (\hat{r}_i - r_i)^2 \, , \tag{4.1}$$

where $i = 0...4$ labels the monitoring locations, respectively $(0.75, 0.2)_{\mathrm{ref}}$, $(5, 0.2)_{\mathrm{ref}}$, $(10, 0.2)_{\mathrm{ref}}$, $(0.75, 0.2)_{\mathrm{lee}}$ and $(5, 0.2)_{\mathrm{lee}}$. A smaller SSR indicates the set of $\hat{r}_i$ is closer to the set of r_i, and implies better modeled results. Figure 4.1 shows the magnitude of squared residuals (indicated by the length of the shaded bars) at all locations ($i = 0$ to 4) for the choices (a) to (h) of spatial distribution of starting trajectory points. Choice (e), i.e. $\delta_{xs} = 3$ m, $\delta_{zs} = 1.5$ m, provides the smallest SSR and by the criteria adopted represents the optimal choice. Therefore simulations reported in this thesis are those using choice (e): starting points in the x-z plane were chosen uniformly within $-61.5 \leq x \leq -58.5$ m,

$z_0 \leq z \leq 1.5$ m as shown in Figure 4.2. The model assumes statistical symmetry along the the y-axis; thus the initial distribution of dust particles adopted by the model on a given transect in the x-z plane was bounded by the rectangular marked in Figure 4.2, i.e. choice (e).

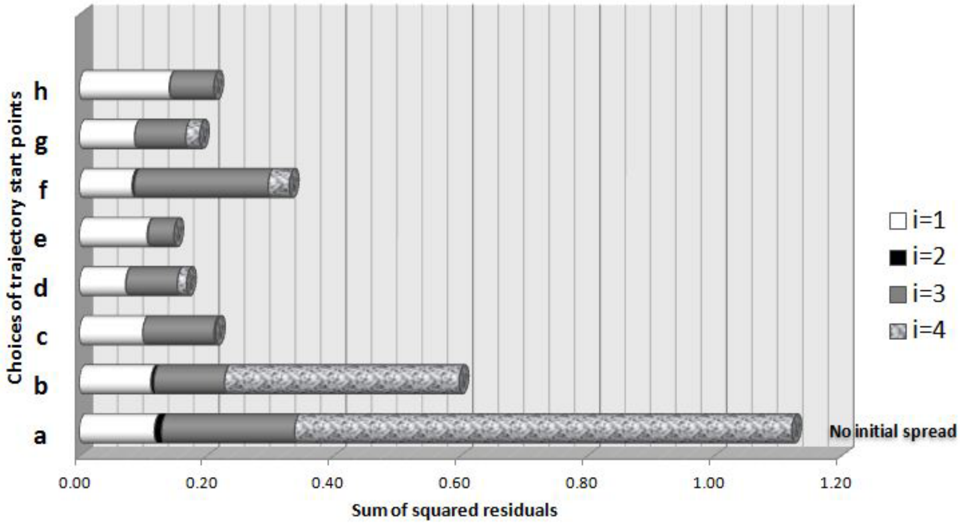

Figure 4.1: Basis for selecting the optimal distribution of trajectory start points for dust transport simulations. Locations (a) to (h) on the y-axis designate the eight alternative choices for the spatial distribution of trajectory start points. The lengths of the differently shaded segments of each bar indicates the contribution $(\hat{r}_i - r_i)^2$ to the overall sum of squares from a particular location, as labeled by the number i shown in the legend: (i=1), $(5, 0.2)_{\text{ref}}$; (i=2), $(10, 0.2)_{\text{ref}}$; (i=3), $(0.75, 0.2)_{\text{lee}}$; (i=4), $(5, 0.2)_{\text{lee}}$. Symbol $\hat{r}_i$ designates the simulated $\frac{\overline{c}_i}{Q}/\frac{\overline{c}_0}{Q}$, and r_i the measured $\overline{c}_i/\overline{c}_0$.

In reality the shape of the initial dust distribution would have been more complex than has been assumed in the model, and it is difficult to model the initial dust puff realistically. Figure 4.1 shows that the accuracy of modeled results is significantly improved by including initial

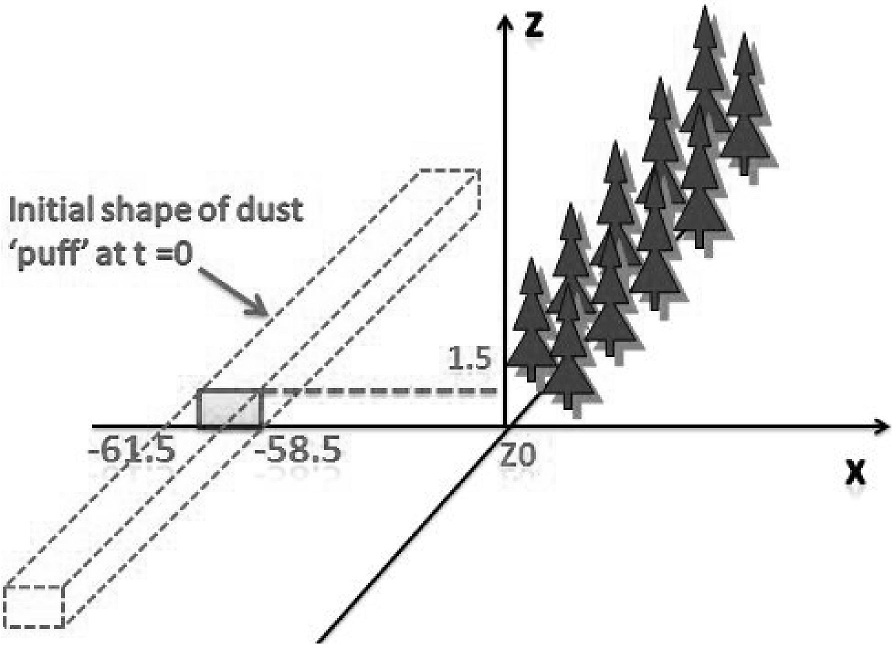

Figure 4.2: Asumed initial shape of the dust puff raised by the vehicle, corresponding to choice (e). This initial distribution was used to model dust dispersion for the experiment at Indian Head.

spread of dust, and (e) is the optimal choice only amongst the initial spread (a) to (h) tested. In other words, and hypothetically, the model might be further improved by adopting an initial spread that more closely matched the (unknown) real situation in the field.

4.1.2 Quantities pertinent to dust dispersion pattern

From the ensemble of computed trajectories the mean concentration at any point can be deduced by Equation (1.58), that is,

$$\frac{\bar{c}}{Q} = \frac{\bar{t}}{V} \, ,$$

where $\bar{t}$ is the average time a particle spends in a volume V (i.e. average residence time) downwind of the source with emission rate Q $[\mathrm{kg\,m^{-1}\,s^{-1}}]$.

Assume symmetry prevails in the cross-stream direction (i.e. along the y-axis). Consider a small "2D-volume" ("numeric concentration detector") centred at (x, z), having depth Δz and a very small alongwind width $\Delta x \ll \Delta z$. Provided $\Delta x \ll |U|\,\Delta t$, where $|U|$ is the alongwind velocity with which a particle passes through this detector, the time spent within the detector by a particle passing through is simply $\Delta x/|U|$. Accordingly the mean residence time $\bar{t}$ of trajectories within the detector "volume" can be computed as

$$\bar{t} = \frac{1}{N_p} \sum_{\alpha=1}^{n} \frac{\Delta x}{\overline{u}(x, z) + {U'}_{\alpha}} \, , \tag{4.2}$$

where $N_p (= 15000)$ is the total number of particles released at the source, $n \leq N_p$ is the number of particles that traverse the concentration detector, and α indexes those traverses such that U'_α is the streamwise velocity fluctuation at the time of the traverse. To a good approximation the horizontal velocity fluctuations can be ignored, and $\bar{c}/Q$ can be expressed

$$\frac{\bar{c}(x,z)}{Q} = \frac{1}{N_p} \sum \frac{\Delta x}{\overline{u}(x,z)\ \Delta z} \ . \tag{4.3}$$

Normalized time average concentration $\bar{c}/Q$ is related to the proportion of trajectories that cross the given detector and inversely proportional to wind speed with which they do so. The ensemble mean concentration transient $\bar{c}(t)/Q$ at a given position can be deduced in a similar way by computing average concentration *at each time step* using the above approach (i.e. averaging the residence time of particles which cross the location at each time step).

The normalized crosswind-integrated deposition rate ($\mathrm{mg\,g^{-1}\,m^{-1}}$) is another output of the LS model. It can be deduced by counting the number of particles ($N_0(x)$) that reach ground out of the total number of particles (N_p) released at the source as

$$D_0(x) = \frac{10^3\, N_0(x)}{N_p\, \Delta x} \ . \tag{4.4}$$

The factor 10^3 translates D_0 into the unit ($\mathrm{mg\,g^{-1}\,m^{-1}}$), conveniently stretching the ordinate. Equation 4.4 gives the amount of dust (measured in mg per 1 g of dust released at the source) which has deposited within a 1 m wide swath centered at the downwind location x.

4.2 Model results and discussion

Two types of model output will be discussed in this section: 1) snapshots of (simulated) puffs of dust at several instants after release from the source (i.e. road), whose extension was represented by a finite width δ_{xs} and height δ_{zs}; and 2) plots of quantities inferred from the ensemble of particle trajectories, such as time average concentration and time-average deposition rate. Specifically, time average concentration for a period of 60 sec will be reported. As stated in section 2.1, the time difference between two consecutive passes of the vehicle is 2 minutes, and simulation results showed that dust concentration has already decreased to zero at all measurement locations as soon as 1 minute after release. Therefore time averages of concentration over 60 sec are here reported (instead of averages over 120 sec) in order to reduce the computational burden of the trajectories calculations (paths are followed for 1 minute, rather than for two).

4.2.1 Simulated dust plume

For each simulation, i.e. puff containing $15,000$ particles of homogeneous size and released upwind either of the unsheltered ("reference") or sheltered area, I show snapshots of the dust plume at three times ($t = 10, 20, 30$ s), these having been chosen so as to display the drift and distortion of the dust plume as it passed over the region $0 \leq x/H \leq 15$. Although the time resolution is coarse, the snapshots reveal some qualitative features of dust dispersion (for various particle sizes). Figures (4.3-4.5) give these snapshots, and the corresponding spatial distribution of the particle number density for airborne and entrapped particles (black vertical strip centred at $x/H = 0$) of diameter 6 μm, 50 μm and 100 μm. The number density is here defined as the number of particles present (at a given time) within a small area with side lengths $\Delta x = 5\,\mathrm{m}$ and $\Delta z = 0.5\,\mathrm{m}$ surrounding the point of interest, i.e. the scale on the image is out of 15000 total number of particles released at the source. Deposited particles are shown in the snapshots (black horizontal swath at the bottom) but omitted on the images of number density distribution, since deposited particles are much more condensed than airborne particles; thus number of deposited particles cannot be clearly represented by the image scale. Showing the spatial distribution of number density at several instants is a way to reflect simulated trajectories from which quantities characterizing dust dispersion patterns (i.e. time average concentration, deposition rate) can be deduced.

The translation (i.e. advection) speed of the dust plumes, the plume duration at each detector, and the spatial distribution of particles are the primary qualitative features I am interested in as I observe the simulated dust plume; especially how the qualitative change of dust plume duration and number density are correlated with the input parameters, specifically, particle size and governing meteorological statistics (overall wind speed as parameterized by the friction velocity or the reference wind speed).

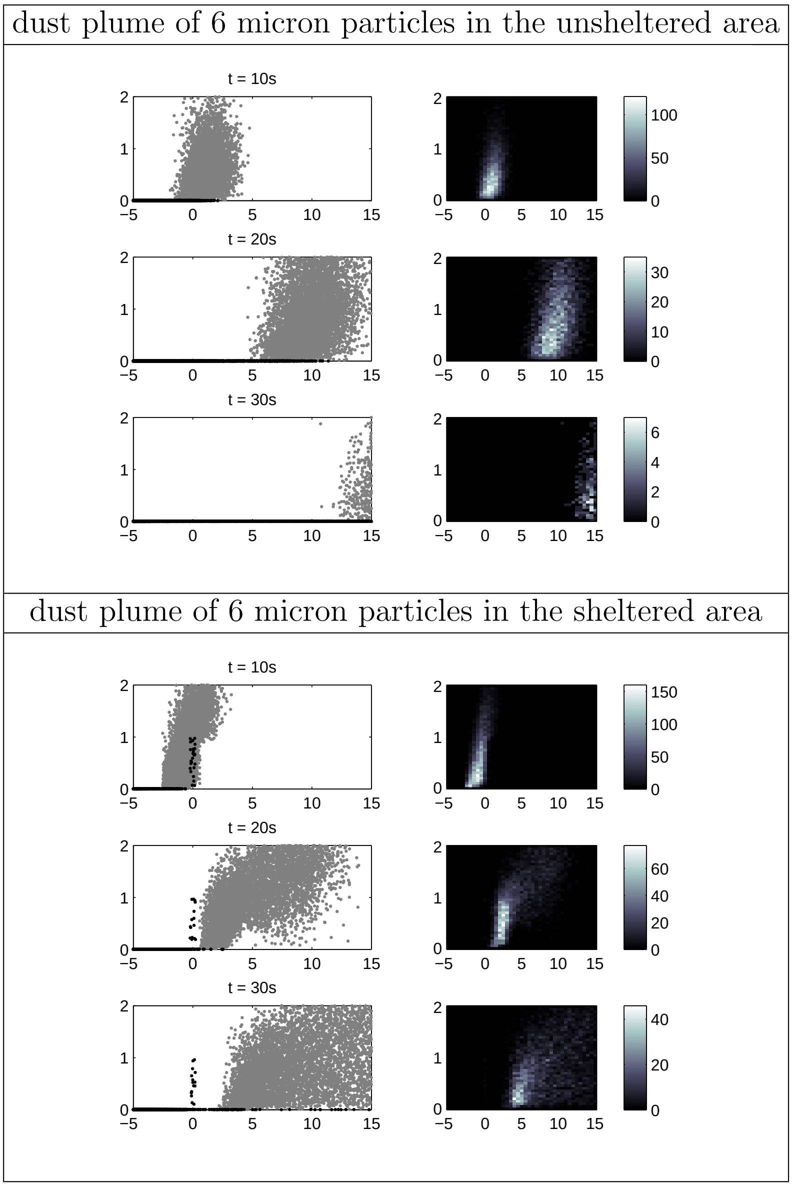

Figure 4.3: Left column: snapshots of (simulated) dust plumes composed of $6\,\mu$m particles at times $t = (10, 20, 30)$ s after their release into a neutral atmosphere (horizontal axis spans $0 \leq x/H \leq 15$, vertical axis $z/H \leq 2$). Right column: corresponding number density of airborne particles (averaging area $\Delta x = 5\,\mathrm{m}$, $\Delta z = 0.5\,\mathrm{m}$).

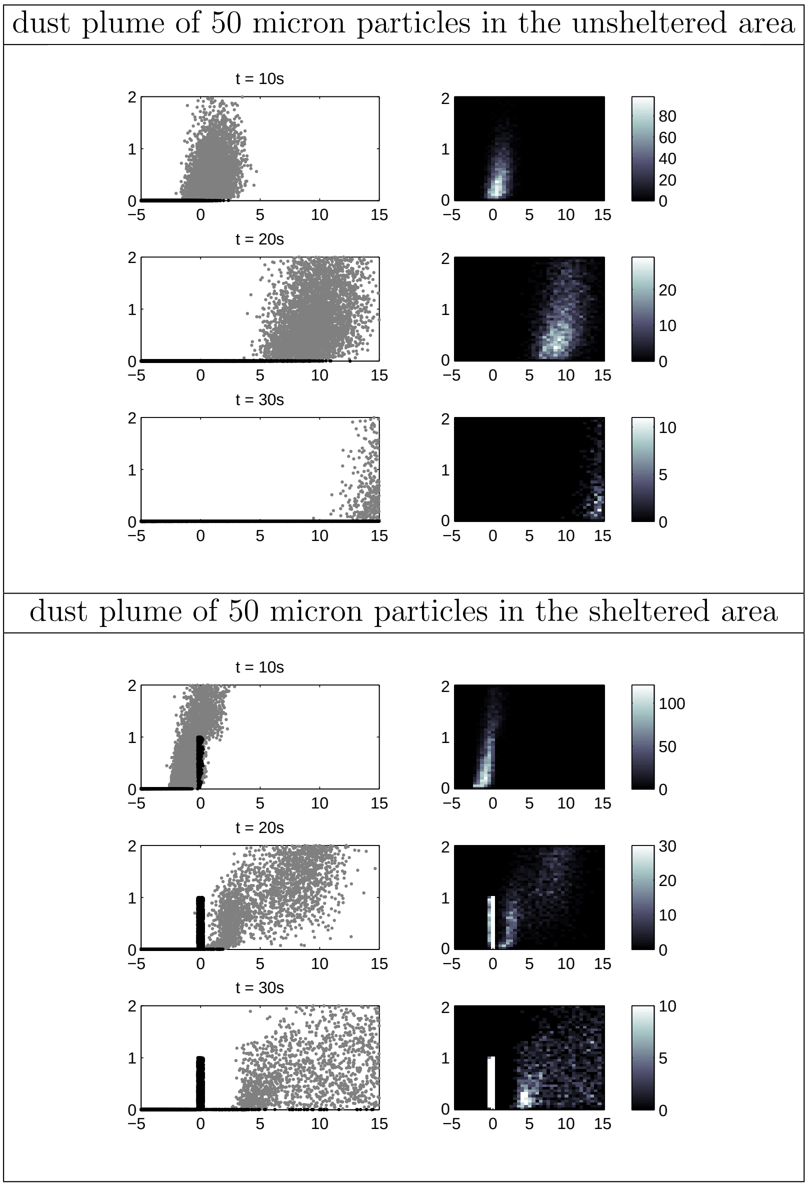

Figure 4.4: Left column: snapshots of (simulated) dust plumes composed of 50 μm particles at times $t = (10, 20, 30)$ s after their release into a neutral atmosphere (horizontal axis spans $0 \leq x/H \leq 15$, vertical axis $z/H \leq 2$). Right column: corresponding number density of airborne particles (averaging area $\Delta x = 5\,\mathrm{m}$, $\Delta z = 0.5\,\mathrm{m}$).

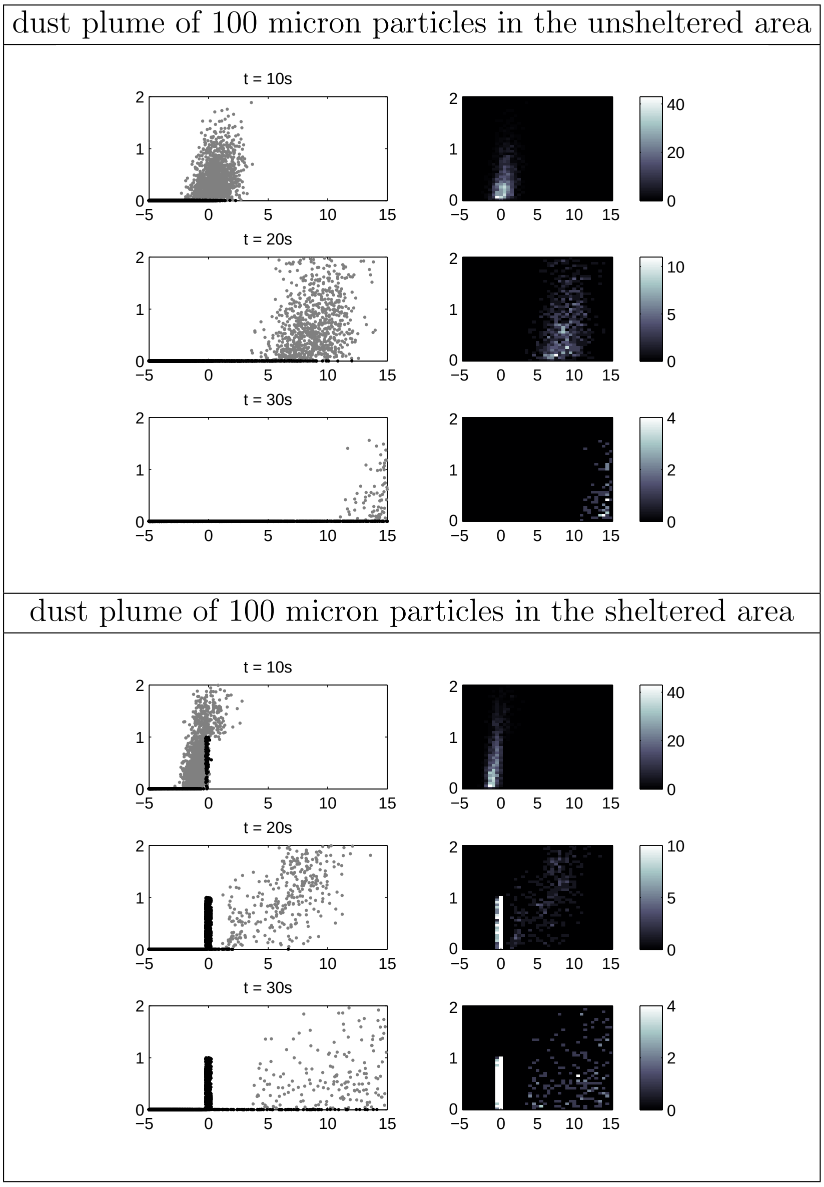

Figure 4.5: Left column: snapshots of (simulated) dust plumes composed of 100 μm particles at times $t = (10, 20, 30)$ s after their release into a neutral atmosphere (horizontal axis spans $0 \leq x/H \leq 15$, vertical axis $z/H \leq 2$). Right column: corresponding number density of airborne particles (averaging area $\Delta x = 5\,\mathrm{m}$, $\Delta z = 0.5\,\mathrm{m}$)

Sheltered area vs. unsheltered area

From Figures (4.3-4.5) it is evident that dust plumes, irrespective of particle size, are transported much faster along the unsheltered (reference) transect than along the sheltered transect. Thirty seconds after release, the upwind edge of the dust plume in the unsheltered area has almost reached the exit end of the region displayed ($0 \leq x/H \leq 15$, $0 \leq z/H \leq 2$). On the other hand at the same time after release more than half of the corresponding display area in the shelter of the windbreak remains occupied by the dust plume. Another salient feature is that the densest part of the dust plume (represented by the light core on images of number density) tends to lag behind in the sheltered area, causing a temporary visible “kink” of the plume at $t = 10$ sec and $t = 20$ sec. In other words, the fast moving upper part of the dust plume tends to spread in the horizontal (x) direction while the dense, slow-moving lower part trails behind. The “kink” is less visible for the largest particles (i.e. diameter = $100\,\mu$m), and notice that a temporary “clean spot” (white space) at lower height centred at $x/H = 5$ is caused by the bent dust plumes. As time elapses, the “clean spot” fills in as dust particles spread. In summary, with reference to these snapshots of simulated dust plumes, dust particles tend to congregate in the lower part of the dust plume which slightly tilts in the unsheltered area; and in the sheltered area, dust particles linger in the lower corner of the upwind side of the dust plume which first bends and then spreads into a larger volume of air.

This pattern, discerned qualitatively from the simulated dust plumes, seems plausible in the light of the "driving" fields of mean wind speed and turbulence, as represented by Figures (3.3, 3.4). It accords with intuition that a dust puff should "tilt," even in a horizontally-homogeneous wind field, because the mean wind speed increases with increasing height (higher dust particles travel faster). However in the sheltered area the vertical shear in the mean horizontal velocity is accentuated due to the combination of a displaced and accelerated jet over the windbreak and a drastically reduced wind speed ("bleed flow") in the "quiet zone" below the top of the windbreak ($0 \leq x/H \lesssim 10$). Furthermore the turbulent kinetic energy (TKE) decreases to a minimum value in the immediate lee, which is consistent with the earlier observation that in these simulated dust plumes particles congregate in the lower upwind corner of the dust plume in the sheltered area. These particles travel downwind much slower than dust particles in the upper part of the plume, and they undergo limited vertical mixing. As a result, an evident "kink" is seen in dust plumes. On the other hand, increased mean wind shear produces a high TKE belt or wake originating near the top of the windbreak, and in that region mixing is intensified. This enhanced vertical mixing may explain why the "clean spot" is closed in a short period of time (less than 10 s), and dust particles eventually spread into the sheltered area.

Small particles vs large particles

From the snapshots of dust plumes, one can see that there is no great difference in the advection speed of the dust plumes, irrespective of particle size, in both the unsheltered area and sheltered area. Nevertheless the number density (see definition in Section 4.2.1) of airborne particles in a given wind field differs a lot. For simplicity, I focus on number density in the densest part of the dust plumes (usually shown in light gray on the images). Two observations can be made regarding the relationship between number density and particle size (note: recall that in the simulations, irrespective of particle size, each plume is defined by the positions of 15,000 particles). Firstly, in a given wind field (whether that be horizontally-homogeneous or disturbed) the number density declines with increasing particle size. Secondly, for small particles, number density is higher in the sheltered area than the unsheltered area, while that trend is reversed for larger particles.

An explanation for these observations emerges by taking into account particle sedimentation (trajectories descending to the roughness height $z = z_0$), the pattern of which is perturbed by the windbreak aerodynamics, and particle entrapment by windbreak foliage. Probability of entrapment is very low for small particles (diameter $D < 10\,\mu\text{m}$), but increases significantly as particle size increases. For particles of diameter $D > 50\,\mu\text{m}$, the entrapment probability starts to approach unity (see Figure 3.5). In both the horizontally-homogeneous and the disturbed wind fields, larger particles are more prone to deposit onto ground due to their gravitational settling. Accordingly one may envisage that most small particles will remain suspended in the air — because neither entrapment nor gravitational settling significantly affects their trajectories; in addition, the dispersion rate of the dust plume, and especially of the dense, lower part, is slower in the sheltered area (see discussion in previous section). Consequently more dust particles tend to congregate and linger at low level in the sheltered area where a higher number density for small particles is observed. On the other hand, a significant number of large particles are removed from the air by early deposition upwind of the windbreak, and by entrapment (shown as thickened black vertical strips in Figures (4.4, 4.5). Notice that deposition rate diminishes in the sheltered area, possibly because (1) the windbreak had already scrubbed out a number of particles that (otherwise) would have deposited onto ground further downstream, and/or (2) turbulence in the wake region might prolong particle residence aloft.

4.2.2 Modeled quantities

Any time after having been injected into the air at the source, particles belong in one or the other of the following three categories: a given particle either is (1) still suspended, or (2) has been deposited to ground, or (3) has been deposited to foliage. This section quantifies the (simulated) patterns of airborne particle concentration, of deposition versus horizontal (downwind) distance, and of entrapment.

Time average concentration $\overline{c}/Q$

The previous qualitative discussion has established that the lower part of a simulated dust plume advects downwind at a slower pace than its upper part, and especially so in the sheltered area where the "quiet zone" is observed. Tables (4.4, 4.5) and the corresponding Figures (4.6 - 4.9) document the theoretical (i.e. simulated) pattern of the normalized mean concentration $\overline{c}/Q$ over a period of 60 s, in terms of transects (reference and sheltered) at $z/H = 0.2$ and $z/H = 1.2$ and for various particle sizes.

	x/H Unsheltered			x/H Sheltered		
diameter μm	**0.75**	**5**	**10**	**0.75**	**5**	**10**
2	8.9E-03	5.1E-03	3.1E-03	1.2E-02	6.9E-03	5.1E-03
6	8.5E-03	4.7E-03	3.3E-03	1.1E-02	8.3E-03	6.5E-03
10	9.2E-03	4.7E-03	3.1E-03	1.0E-02	9.1E-03	4.8E-03
20	8.3E-03	5.1E-03	2.8E-03	1.0E-02	9.1E-03	4.7E-03
50	6.9E-03	4.0E-03	2.2E-03	2.6E-03	2.9E-03	9.8E-04
100	2.0E-03	9.5E-04	4.5E-04	1.1E-04	0.0E+00	9.2E-05

Table 4.4: Modeled $\overline{c}/Q$ over an averaging interval of 60 s for various particle sizes at $z/H = 0.2$ under neutral stratification

Figures 4.6 and 4.7 show that $\overline{c}/Q$ *is higher in the sheltered area than in the unsheltered area, except for the case of very large particles (i.e. diameters* $D \geq 50\,\mu$m *).* The difference between $\overline{c}/Q$ in the unsheltered area (reference) and in the sheltered area is more distinct at higher levels. For small particles ($D \leq 10\,\mu$m), $\overline{c}/Q$ can be three to

	x/H Unsheltered			x/H Sheltered		
diameter μm	**0.75**	**5**	**10**	**0.75**	**5**	**10**
2	1.1E-03	2.0E-03	2.0E-03	4.0E-03	5.6E-03	4.1E-03
6	1.2E-03	2.1E-03	2.0E-03	3.5E-03	5.1E-03	3.9E-03
10	1.3E-03	1.9E-03	2.0E-03	3.4E-03	5.0E-03	4.5E-03
20	1.0E-03	1.8E-03	1.9E-03	3.5E-03	4.8E-03	3.8E-03
50	6.7E-04	1.0E-03	1.3E-03	1.5E-03	1.3E-03	1.2E-03
100	1.0E-04	3.4E-04	1.9E-04	4.4E-04	1.7E-04	1.9E-04

Table 4.5: Modeled $\overline{c}/Q$ over an averaging interval of 60 s for various particle sizes at $z/H = 1.2$ under neutral stratification

four times larger along the "shelter" transect at $z/H = 1.2$ than at the same height on the reference transect. A possible explanation for this is the mean vertical wind induced by the windbreak, which possibly lifts small particles to the 12 m height of the upper transect. However the horizontal wind speed at $z/H = 1.2$ is still subject to reduction in the lee of the shelterbelt, even if the magnitude of that reduction is not as large as occurs along the lower transect at $z/H = 0.2$. Consequently, particles which attain the height of 12 m have a longer stay at any given detector before they are advected further downwind, and as indicated by Equation 1.58 the value of $\overline{c}/Q$ in any volume is proportional to the average time a particle spends within it. In addition, by comparing Figures 4.6-4.7, one can see that on both transects and at all downwind distances $\overline{c}/Q$ *is much lower at* $z/H = 1.2$ *than at* $z/H = 0.2$. This is due to the fact that the particle source is at or near ground. Moreover, notice that $\overline{c}/Q$ *at a given downwind distance declines rapidly for particles of diameters* $\geq 10\,\mu$m (see Figures 4.6 -

4.7). For larger particles, faster decrease of $\overline{c}/Q$ can be attributed to more significant ground deposition and windbreak entrapment being found for larger particles than smaller particles.

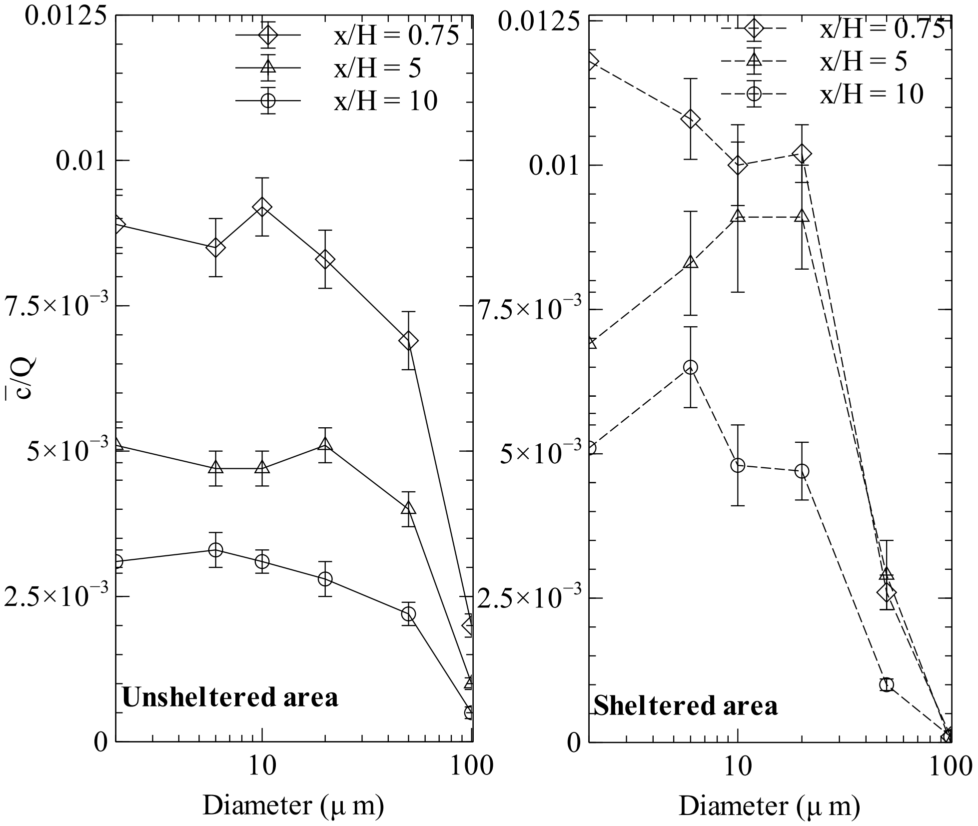

Figure 4.6: Modeled size distribution of time averaged concentration over 60 s normalized by source strength ($\overline{c}/Q$) at positions $(0.75, 0.2)$, $(5, 0.2)$ and $(10, 0.2)$ along the unsheltered (i.e. reference) and sheltered transect under neutral stratification. Error bars show the standard deviation of the 15 realizations of each run of the LS model.

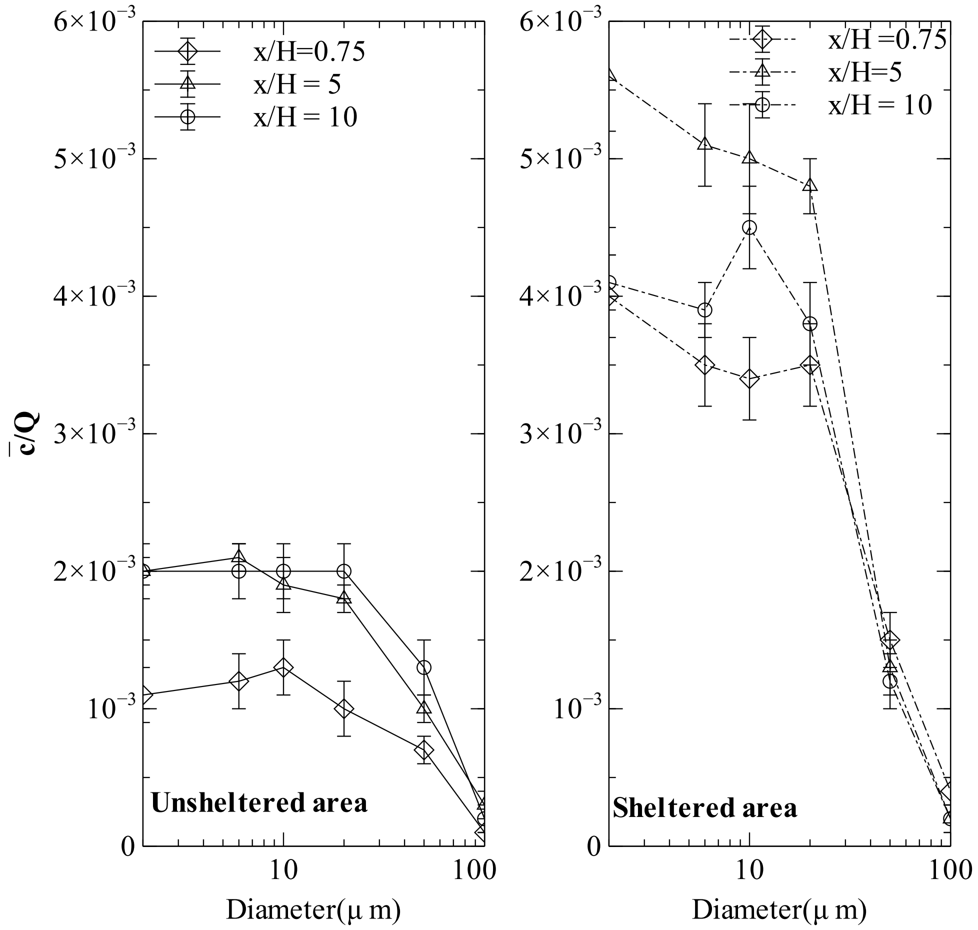

Figure 4.7: Modeled size distribution of time averaged concentration over 60 s normalized by source strength ($\bar{c}/Q$) at positions $(0.75, 1.2)$, $(5, 1.2)$ and $(10, 1.2)$ along the unsheltered (i.e. reference) and sheltered transect under neutral stratification. Error bars show the standard deviation of the 15 realizations of each run of the LS model.

Intuitively, one might think that higher downwind dust concentration occurs at places closer to the source, but this is not always true as indicated by the simulated results (Figures 4.8 and 4.9). *At $z/H = 1.2$, higher concentration favors locations at further downwind distances in the unsheltered area, and the highest concentration usually occurs at $x/H = 5$ in the sheltered area.* One may ask why high concentration at high level is not found at $x/H = 0.75$, the smallest x/H closest to the source? This is mainly because it takes time for released particles to be mixed up to the higher level, and as particles reach the higher level ($x/H = 1.2$), they were transported further downwind in the horizontal direction; therefore, the peak concentration need not occur at the position closest to the source. Since $\overline{c}/Q$ is proportional to $\bar{t}$ (Equation. 1.58), it is not surprising that higher concentration is often found in the sheltered area because of slower wind speed resulting in a longer residence time.

Ensemble mean concentration transient $\overline{c}(t)/Q$

The time average normalized dust concentration $\overline{c}/Q$ does not provide information regarding questions such as as the following: at a given location, how long after dust injection will peak dust concentration occur? What is the value of that peak concentration? How long will the dust plume dwell at that given location? These questions can however be addressed by the model by looking at the ensemble mean concentration transient $\langle c(t)\rangle/Q$. Figure 4.10 shows the ensemble mean

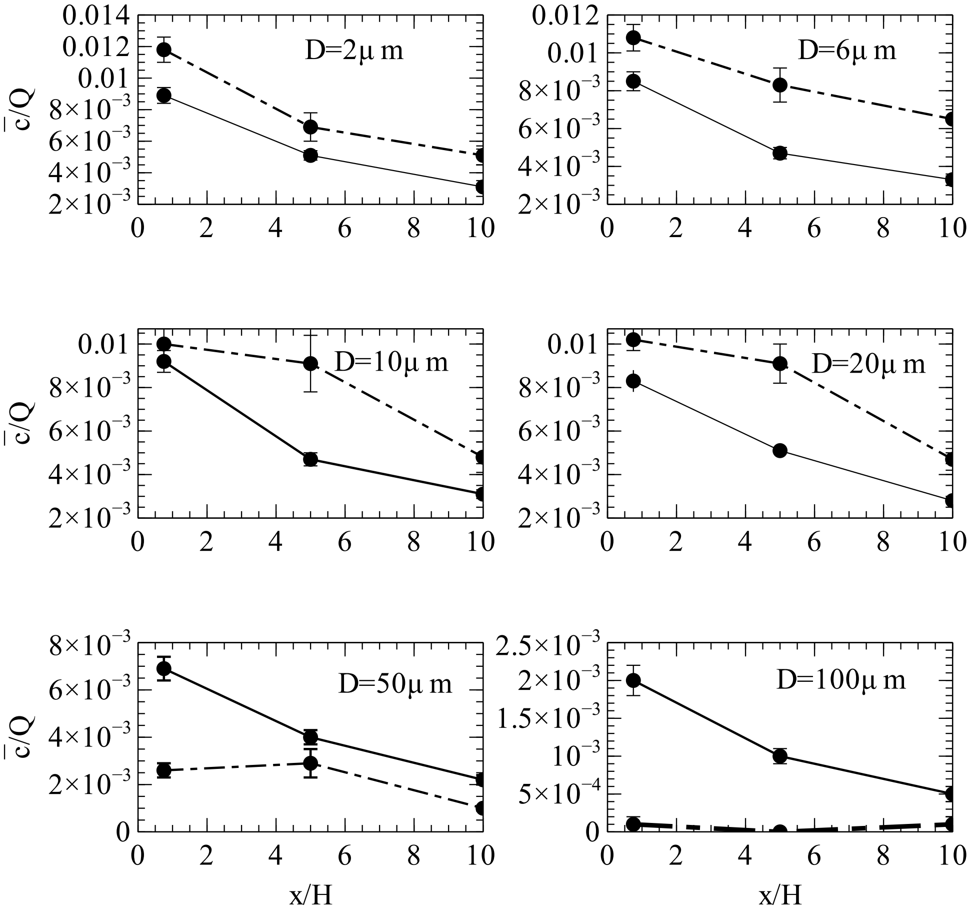

Figure 4.8: Comparing the evolution of time average $\overline{c}/Q$ over 60 s along downwind distances on the **unsheltered (solid lines)** and **sheltered transect (dashes lines)** at $z/H = 0.2$ for various particle sizes with labeled diameters.

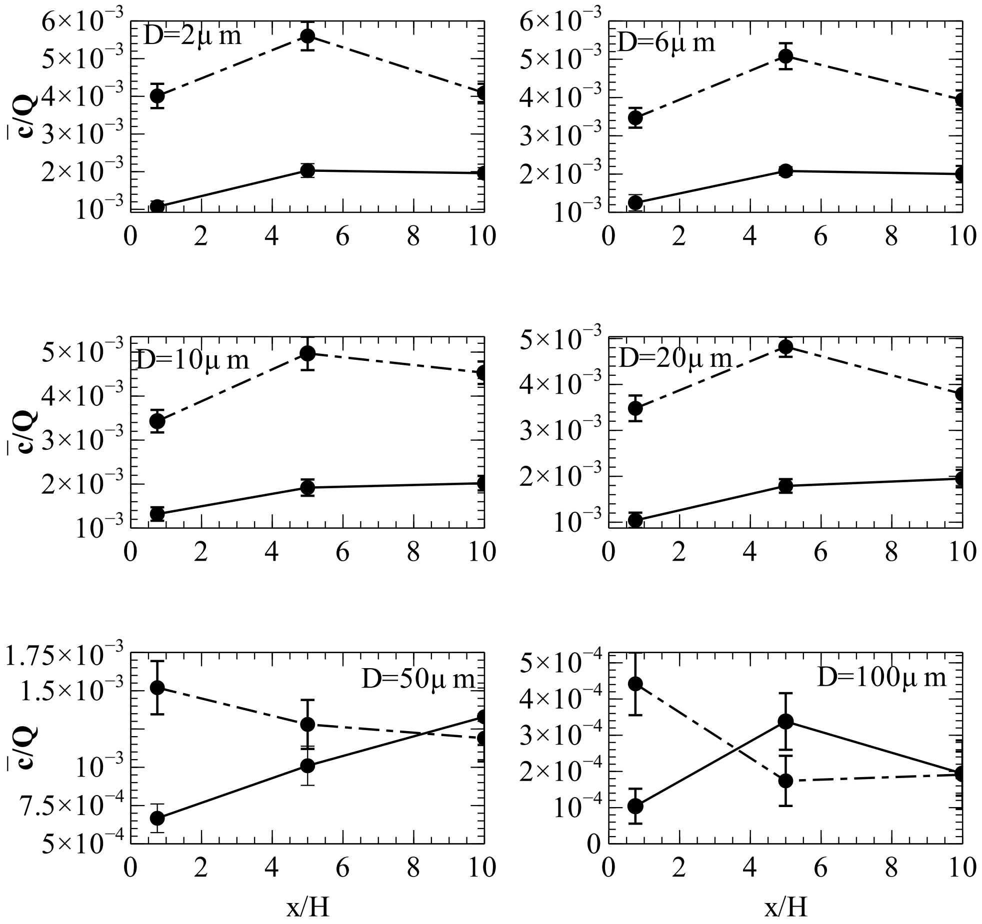

Figure 4.9: Comparing the evolution of time average $\overline{c}/Q$ over 60 s along downwind distances on the **unsheltered (solid lines)** and **sheltered transect (dashes lines)** at $z/H = 1.2$ for various particle sizes with labeled diameters.

transients for particles of diameter $D = 6\,\mu$m (small particles) along the upper and lower transects at $x/H = 0.75, 5, 10$. Figure 4.11 shows the same information for large particles of diameters of $100\,\mu$m.

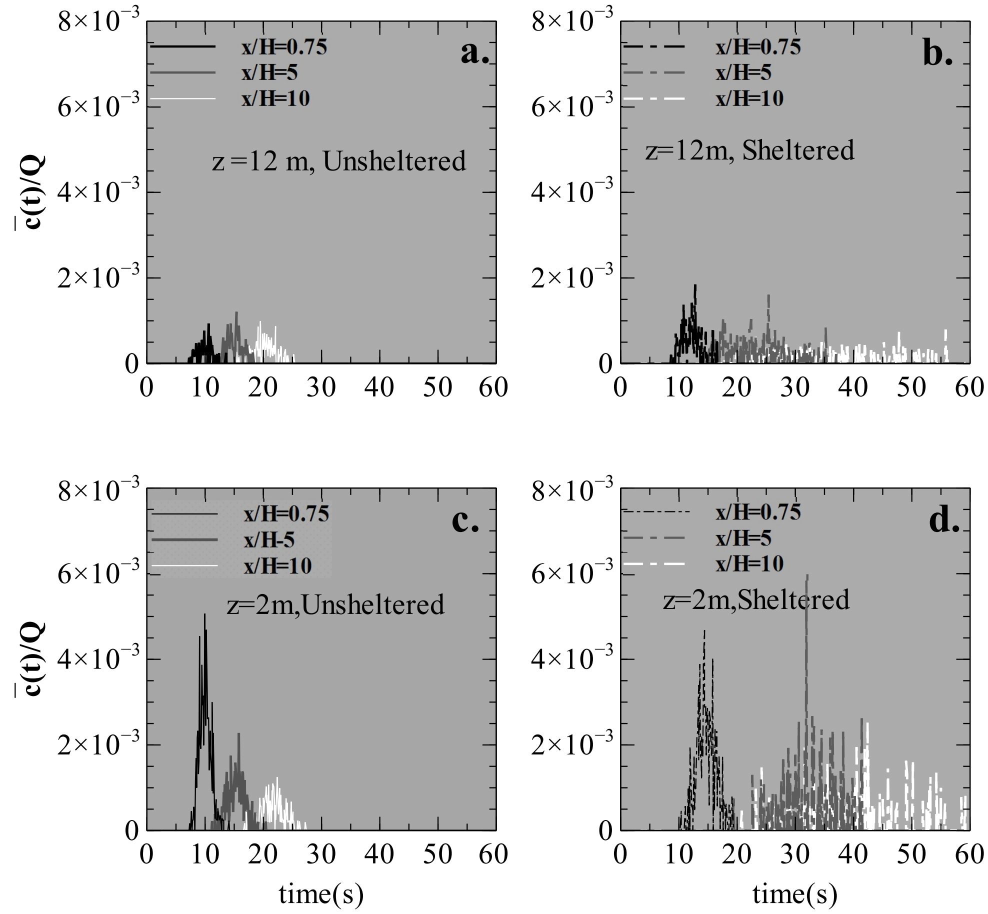

Figure 4.10: Modeled concentration transients $\bar{c}(t)/Q$ for $6\,\mu$m particles. Neutral stratification.

Two observations can be made by comparing Figures 4.10 and 4.11. Firstly, there is no obvious difference, at any location, between the

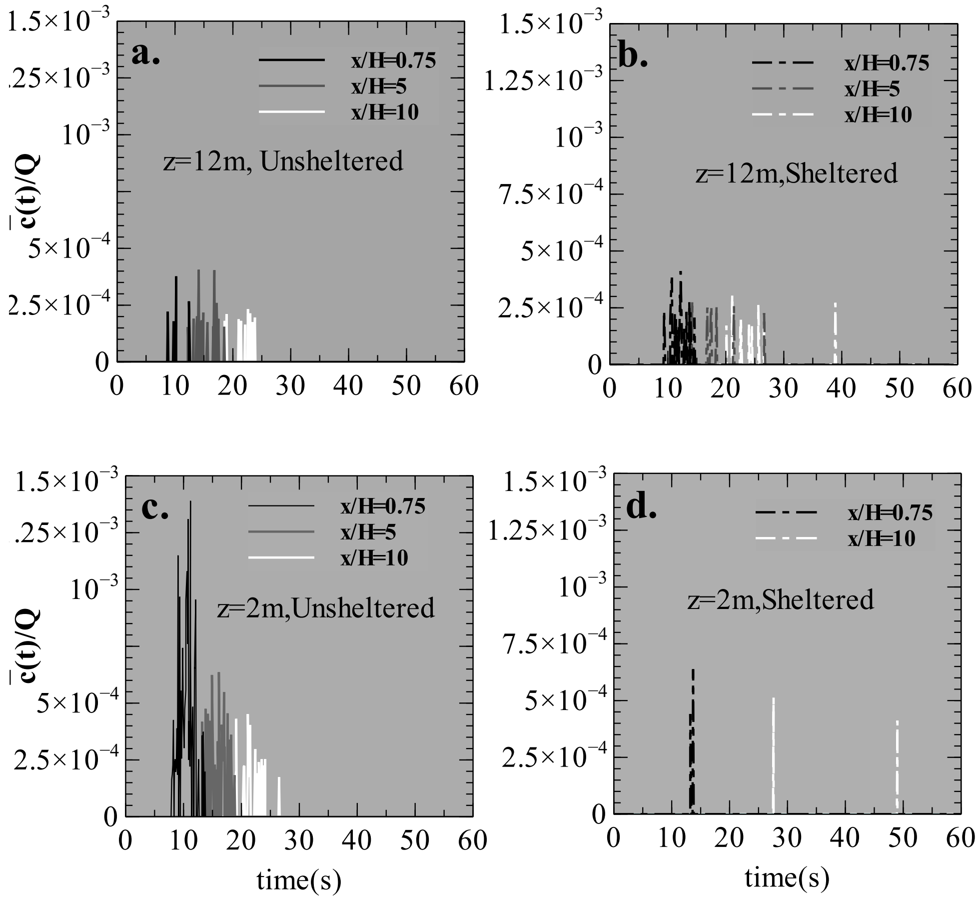

Figure 4.11: Modeled $\overline{c}(t)/Q$ for 100 μm particles at under neutral stratification.

durations of plumes of small and large particles, a point that had earlier been deduced (Section 4.2.1) from snapshots of model dust plumes. Secondly, the concentration transients are smoother for the smaller particles. Concentration transients for the large particles consist of zeros and spikes, especially in the sheltered area. This is in one sense merely a sampling problem, for the irregularity of the ensemble mean transient could be reduced by computing many more trajectories. However the windbreak, either directly (through particle entrapment) or indirectly (altered pattern of deposition), reduces the number of surviving trajectories in its wake, accentuating the sampling problem.

The following discussion of the ensemble mean concentration transient is based on Fig. 4.10. The reader is asked to envisage the experience of (imaginary) butterflies lingering at certain locations downwind of the source, once a plume of dust (containing a large number of small particles) had been injected by a moving vehicle. Consider three pairs of butterflies, two black, two cyan, and two magenta, were flying at an elevation of 2 m. Once a puff of dust had been injected into the air and started to travel downwind, the two **black** butterflies chose to rest at $\mathbf{x/H = 0.75}$; the two **cyan** ones lingered at $\mathbf{x/H = 5}$; and the two **magenta** ones decided to stay at positions further downwind $\mathbf{x/H = 10}$. One member of each pair positioned itself in the lee of the windbreak, the other on the transect across the unsheltered area. From subplots **c.** and **d.** of Fig. 4.10 we see that in the unsheltered area all butterflies encountered the dust plume earlier than their counterparts in the sheltered area. On the other hand, all butterflies in the sheltered area experienced a longer duration of immersion in the dust plume than did their counterparts in the unsheltered area. The lag between plume onset times as observed by each pair was longer for the cyan ($x/H = 5$) and magenta ($x/H = 10$) butterflies. In both the uniform and the disturbed wind fields, the black ($x/H = 0.75$) butterflies experienced the highest peak dust concentration, and the magenta ones ($x/H = 10$) experienced the lowest peak concentrations. Nevertheless, the magenta ones had the longest immersion in the dust plume, whereas for the black butterflies the dust plumes arrived and passed promptly.

Now imagine that the three pairs of butterflies flew up to 12 m, and stayed at exactly the same horizontal positions as before. Their experience with the passage of the dust plumes can be predicted by subplots **a.** and **b.** of Fig. 4.10. It is evident that they would experience categorically lower dust concentrations than at the lower level. The black butterfly in the unsheltered area would experience about the same peak concentration as the magenta and cyan. In addition, the butterflies no longer experience the sudden rise and dissipation of dust concentration; butterflies in the sheltered area would experience a prolonged passage of dust plumes with steady low concentration. Even for butterflies in the unsheltered area, the change of concentration became more gradual. In short, change of dust concentration is abrupt (i.e. sudden rise and drop) in the unsheltered area especially for downwind locations close to the source at lower levels. On the other hand, dust concentration tends to be lower and steadier (longer passage of dust plumes) in the sheltered area, especially for far downwind locations at higher levels.

Deposition rate

Although the effects of a windbreak on concentration of airborne dust particles are ultimately of the greatest interest, those effects cannot be properly comprehended without considering how the windbreak perturbs the pattern of dust deposition to ground, and the degree to which it directly scrubs the airstream (the latter topic, i.e. particle entrapment by the windbreak, is described in the next section).

Fig. 4.12 compares the transects of normalized deposition rate (as defined by Equation 4.4) for three particle sizes ($D = 6\,\mu$m, $D = 50\,\mu$m, and $D = 100\,\mu$m).

A few observations can be made relative to this figure. Firstly, it is evident that in both the unsheltered area and in the sheltered area, the highest rate of deposition occurs even before the particles reach the location $x/H = 0$. Secondly, and again in both the unsheltered and sheltered areas, the peak deposition rate for 100 micron particles (i.e. the largest) is significantly higher than that for the smaller particles (in the sheltered area peak deposition rate for 100 micron particles is nearly twice as high as for 50 micron particles, and 4 times as high as for the 6 micron particles). Thirdly, irrespective of particle size there are only small differences in the peak values and peak locations between the unsheltered area and sheltered area; the peak deposition rate for the 100 micron particle is slightly higher in the sheltered area ($D_0 \approx 40\,\mathrm{mg\,g^{-1}\,m^{-1}}$) than in the unsheltered area

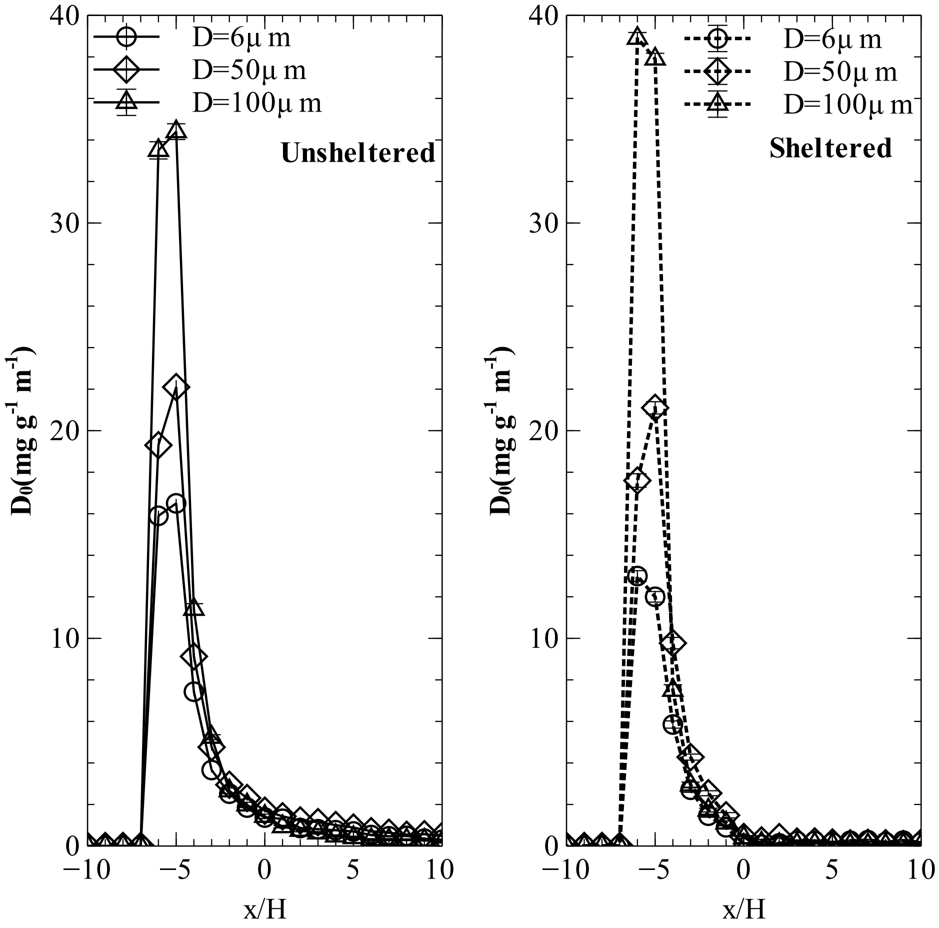

Figure 4.12: Comparing modeled deposition rate $D_0(\,\mathrm{mg\,g^{-1}\,m^{-1}})$ for particles of small ($D = 6\,\mu$m), medium ($D = 50\,\mu$m), and large size ($D = 100\,\mu$m) in the sheltered area and unsheltered area. The location of the windbreak is $x/H = 0$.

($D_0 \approx 35\,\mathrm{mg\,g^{-1}\,m^{-1}}$), whereas the higher peak deposition rate for the 6 micron particle is found in the unsheltered area. Fourthly, compared to the peak deposition rates, deposition rates at locations $x/H \geq 0$ are very low, both in the unsheltered and sheltered areas; however *some* deposition ($D_0 \leq 5\,\mathrm{mg\,g^{-1}\,m^{-1}}$) does occur beyond $x/H = 0$ in the unsheltered area, whereas downwind of the windbreak D_0 is almost zero. This latter feature can also be seen in the dust plume snapshots (Tables 4.3, 4.4, 4.5) in which the gradually fading and sporadic black colors represent the amount of deposition in the lee of the windbreak.

Bouvet et al. (2006) studied heavy particle deposition in a windbreak flow by comparing the modeled deposition rate (using an LS model) to observations conducted in a flow disturbed by a porous windbreak fence. They concluded that the fence plays two roles in dispersion of particles;

(1) it traps some particles as the dust-laden air flows through it;

(2) it disturbs the ambient wind field, and thereby alters the trajectories of particles.

Their results show that, with the source just upstream and slightly above the top of the fence, deposition to ground is significantly reduced (relative to undisturbed flow) due to scrubbing of the particle plume by the fence (entrapment). The influence of the disturbed wind flow on deposition to ground is more complicated because changes both in the horizontal and vertical wind components “affect the deposition swath in contrary senses, and the true effect of the windbreak lies between those two asymptotic situations” (Bouvet et al. 2006). The disturbance to the horizontal wind field causes the deposition swath to shift upwind, and become narrower and more peaked (drastic reduction of the horizontal wind speed near the windbreak causes the particles to congregate and deposit much earlier). On the other hand the disturbed vertical wind causes the deposition swath to shift downwind with wider spread and reduced peak deposition rate because the curvature of the air flow (positive mean vertical wind speed where the flow approaches the windbreak) lifts the particle plume; in this way, particles have a greater chance to be advected away and spread further before depositing to the ground.

The trajectory calculations that have been a component of this thesis project indicate an obvious decrement of deposition rate downwind of the windbreak, due to entrapment; otherwise however, the width of the swath, and the peak deposition rate and its location do not differ greatly between the sheltered and unsheltered areas. Taking into account the conclusion of Bouvet et al. (2007), it is difficult to decide whether the deposition rate is more greatly affected by the change of horizontal or of vertical wind in the air flow disturbed by the windbreak. However, the third observation above, (i.e. that the modeled peak D_0 for 100 micron particles is higher in the sheltered area, and peak D_0 for 6 micron particles is higher in the unsheltered area) suggests that larger particles are more likely to be influenced by the reduced horizontal wind speed, while conversely small particles are more likely to be lifted by the positive vertical wind speed in the vicinity of the windbreak. In addition, Figure 4.12 shows that the modeled peak deposition rate of 100 micron particles is significantly higher than that of smaller particles along both the unsheltered transect and sheltered transect, and the peak deposition rate occurs just upwind of $x/H = 0$. This observation can account for the fact that the modeled time average $\overline{c}/Q$ for 100 micron particles downwind of $x/H = 0$ is significantly lower than that for small particles (as indicated by Figures 4.6, 4.7). This is because most large particles are removed from the air by deposition before they have reached the position $x/H = 0$.

Windbreak entrapment

Quite apart from sedimenting out of the air to ground, suspended dust particles can be removed from the bleed flow by deposition onto the foliage of a shelterbelt. Section 3.2.3 introduced the parameterization of windbreak entrapment that has been adopted for this LS model, and showed that the probability of entrapment increases as particle size increases (Fig. 3.5). Figure 4.13 shows how the entrapped fraction (i.e. number of particles deposited to the foliage divided by the total number of particles released) varies with particle size, as indexed by the gravitational settling velocity (particle density $\rho_p = 1522\,\mathrm{kg/m^3}$, the value assumed for the field experiment at Indian Head). Entrapped fraction peaks for the particle size $D = 50\,\mu\mathrm{m}$, rather than increasing monotonically as does the probability of entrapment. Here is one possible explanation. Although larger particles have a higher probability of being entrapped by the windbreak, fewer of them can make their way to the windbreak in the first place due to the higher deposition

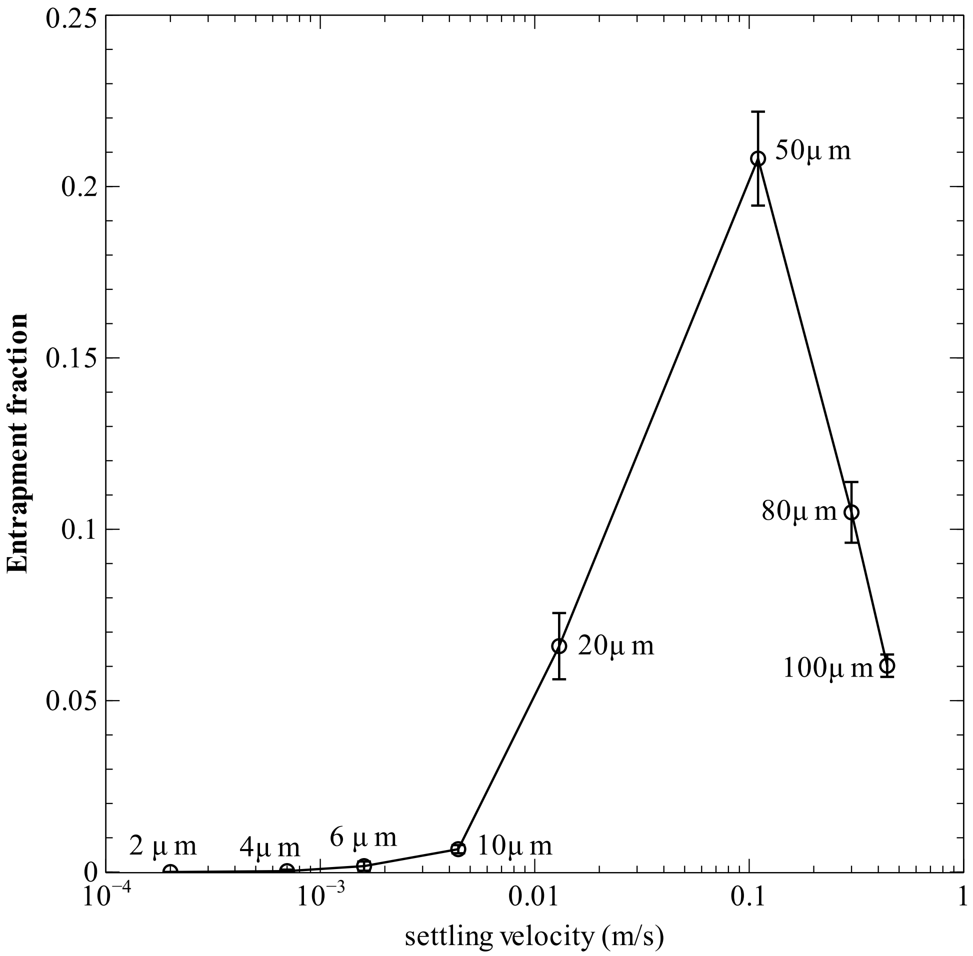

Figure 4.13: Entrapment fraction (number of particles deposited to foliage out of total number of particles released at the source) vs settling velocity w_g simulated in the neutral surface layer over a time period of 60 s. The corresponding particle diameter is shown next to each data point.

rate to ground that results from their larger gravitational settling velocity (see Figure 4.12). On the other hand, a larger number of smaller particles *can* reach the location of the windbreak but they are more likely to be lifted over the windbreak, or to flow through the windbreak without entrapment onto the foliage because their probability of entrapment is low. Therefore, the maximum entrapment is associated with a medium particle size, since a considerable number of medium particles can reach the vicinity of the windbreak due to their moderate deposition rate, while a relatively high probability of entrapment ensures that a large number of medium particles will be deposited to the foliage. Notice that Figure 3.5 shows that the probability of entrapment starts to approach unity for dust particles of diameter larger than 50 μm, and Figure 4.12 shows that deposition rate for 50 micron particles is significantly lower than very large particles but not much higher than small particles; therefore, that entrapment fraction peaks at 50 micron dust particles is a reasonable result for this LS model. The experimental results of field trials at Indian Head indicate that dust plumes in the field were mostly composed of small partilces (diameters smaller than 10 μm). In fact, Figures 2.22 and 2.23 show that more than 90% of dust particles detected in the field were smaller than 10 μm. This suggests that entrapment had a only minor inflence in field experiments conducted in Indian Head, which explains why time average concentrations measured along the sheltered transect were not very different from those at matching locations along the unsheltered transect (Figures 2.20, 2.21).

4.2.3 Summary

The preceding sections of this chapter have introduced readers to the results provided by the Lagrangian stochastic model, as regards concentration of airborne particles, deposition rate, and entrapment fraction. As mentioned in the beginning of Section 4.2.2, any time after a single particle starts its imaginary journey (as simulated by the LS model), it must belong in one of three categories: (1) it remains airborne, (2) it has been deposited to the ground, or (3) it has been entrapped by the windbreak. Therefore, the effects of the windbreak on particle dispersion should be viewed by putting the three pieces of information together. However, the units for modeled quantities expressing concentration of airborne particles, deposition and entrapment are all different, which makes it difficult to deduce potential connections amongst them, and the connections may be essential to reveal the effects of the windbreak on dust dispersion. From Section 4.1, the readers can see that the simulated properties $\overline{c}(t)/Q$ and D_0 are related to the fraction of total particles released at the source (i.e. number of particles that fall into one of the three categories out of total number of particles released), and the implementation of the LS model ensures that the sum of the fractions of airborne particles, deposited particles and entrapped particles should be unity.

Summarizing these fractions by way of a pie chart (Figure 4.14) gives a general picture how the dust dispersion pattern is influenced by the windbreak. The figure shows that for small ($D = 6\,\mu$m) particles, windbreak entrapment is insignificant (no influence on fraction airborne). However although a trivial number of these small particles are entrapped by the windbreak, the fraction of particles remaining airborne (at $t = 60$ s) in the disturbed wind field is nearly twice as large as in the reference flow (unsheltered area). For particles as large as $20\,\mu$m, the airborne fraction in the inhomogenous wind field increases approximately 40 %. Although not as distinct a rise as for the $6\,\mu$m particles, this increment in the fraction of particles remaining airborne for $20\,\mu$m in the sheltered area is still significant enough to account for the rising concentration in the sheltered area as shown in Figures 4.6 and 4.7. From the pie chart, one may conjecture that the increment in concentration for small particles in the lee of the windbreak is caused mostly by a decreased fraction of deposited particles in the sheltered area. This suggests that small particles have a stronger tendency of remaining in the air in the sheltered area, whereas they are more likely to be deposited to ground in the unsheltered area. According to Bouvet et al. (2006), and as explained in section 4.2.2, this is mostly likely attributable to the upward mean wind in the vicinity of the windbreak; the positive vertical wind speed can cause small particles to drift further downstream in the air.

On the other hand, the pie charts for large particles show that there is no significant difference in the fraction of airborne particles (the dark gray area) between the unsheltered area and sheltered area. The area representing the fraction of deposited particles (the light gray area) in the unsheltered area is divided into fractions of entrapped particles and deposited particles in the sheltered area, and the area of deposition fraction dominates the pie charts for both the unsheltered area and sheltered area. Figure 4.12 shows that the peak deposition rate around $5H$ upwind of $x/H = 0$ is increased in the sheltered area for $100\,\mu$m particles, and the values of peak deposition rate in the unsheltered area and sheltered area are approximately the same for $50\,\mu$m particles. The corresponding pie charts for the two particle sizes show that the number of deposited particles is reduced in the lee of the windbreak. Putting these two together, one reaches the conclusion that *the number of **large particles** deposited in the lee of the windbreak is reduced (relative to the same location in uniform flow) due to entrapment and few particles survive their passage through the windbreak in the bleed flow.* This feature can be seen on snapshots for the dust plumes consisting of $50\,\mu$m particles, for which the deposition fraction is reduced most according to the pie chart, and the fraction of entrapment achieves its maximum value according to Fig. 4.13. The snapshots (Figure 4.4) for a $50\,\mu$m particle plume clearly show that the black swath representing deposited particles is sporadic and much thinner in the lee of the windbreak than in the unsheltered area.

In short, for small particles, the altered dispersion pattern (i.e. increase in concentration of airborne particles) in the lee of the windbreak is mainly caused by the disturbed wind field, and windbreak entrapment has little influence. On the other hand, windbreak entrapment plays an important role in decreasing the deposition fraction for large particles in the lee of the windbreak.

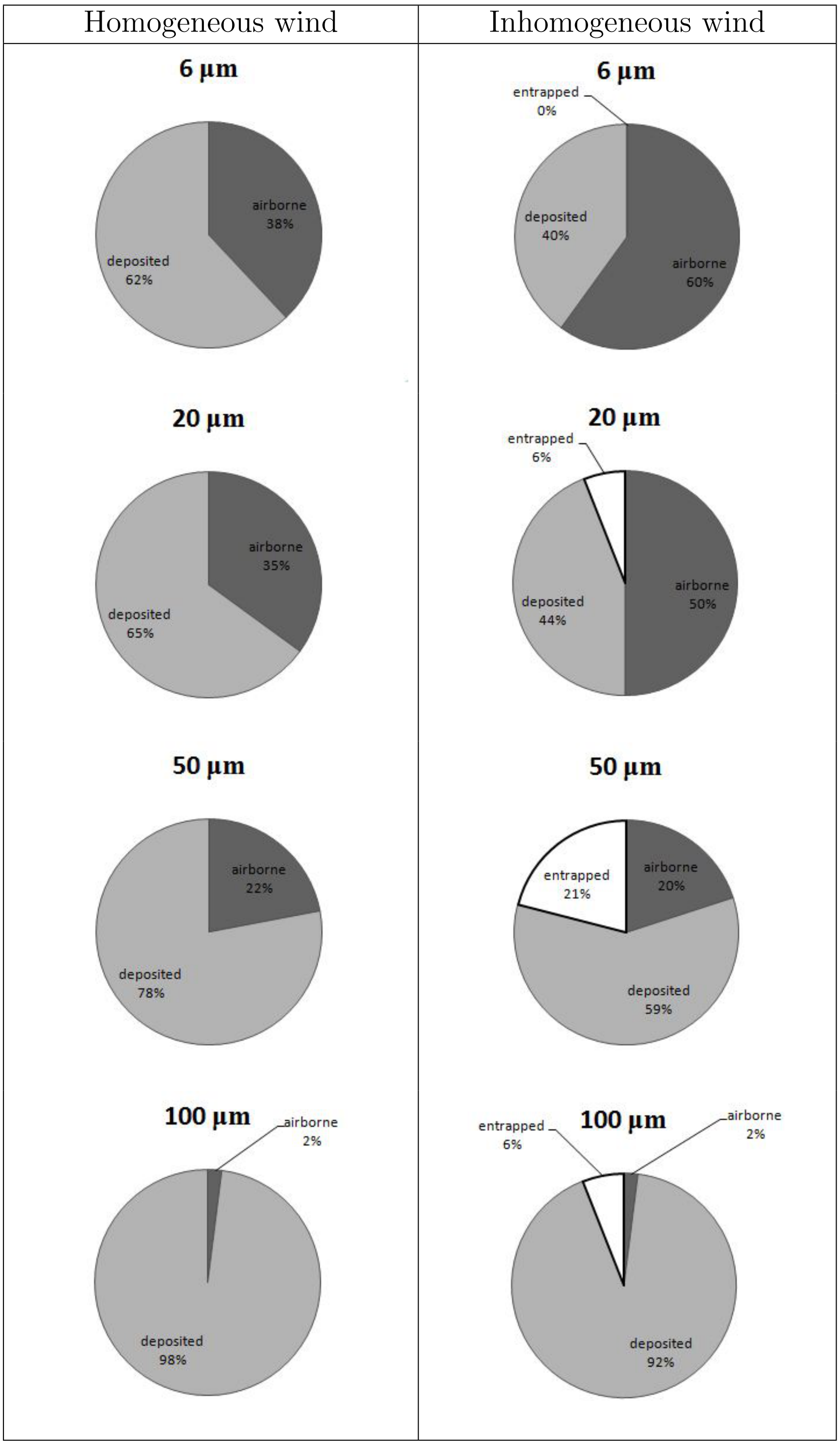

Figure 4.14: Fate of dust particles 60 s after their release, in the undisturbed and disturbed wind field for a neutral atmosphere.

Chapter 5

Comparison: modeled results and observations

The observations of the Indian Head experiment were presented in Chapter 2, while analogous model results were covered in Chapter 4. The next (and final) step is to directly compare the observations with the model, for the following purposes: 1) to continue the quest to understand the effects of the windbreak on dust dispersion, by comparing the dispersion pattern in the lee of the windbreak with that in an unsheltered area, and, 2) to assess the validity of the Lagrangian stochastic model adapted for the project.

5.1 Theoretical basis for inferring concentration

Dust concentration is the primary quantity measured in the field, and the only quantity that can be compared with model results. The concentration data are of two types, viz. the size-segregated concentrations measured by the Rotorods, which are a time-average over the entire 40 minutes of each experiment (symbol $\overline{c}_k$, where k designates a size class); and ensemble-averaged aggregate concentration transients (symbol $\langle c(t) \rangle$) as provided by the Casella real time dust monitors.

Theoretical average concentrations provided by the LS model are invariably normalized by source strength, i.e. the model provides $\overline{c}(t)/Q$ or, if size segregated, $\overline{c}_k/Q_k$. If the source strength (emission rate) Q (or Q_k) were known, a theoretical value for concentration could be inferred by the simple relation

$$\overline{c} = Q \times (\frac{\overline{c}}{Q}) \, ,$$

which raises the question: how might one deduce the dust emission rate?

5.1.1 Inverse dispersion method

Flesch & Wilson (2004) illustrated the use of a variant of the "inverse dispersion method," a term used when a source strength is inferred indirectly from one or more measured concentrations. To determine the emission rate Q from ground-level area sources having a known perimeter (and which were assumed to emit at a uniform rate), time-average tracer concentration $\overline{c}$ was measured at a point **P** within the plume, and the theoretical (i.e. modelled) value for $(\overline{c}/Q)_{mod}$ at point **P** was provided by a Lagrangian stochastic model which simulated the transport of tracer gas under the prevailing meteorological conditions. The emission rate (source strength) was inferred as

$$Q = \frac{(\overline{c} - c_b)}{(\overline{c}/Q)_{mod}}, \tag{5.1}$$

where c_b is the background tracer concentration. Flesch & Wilson (2004) demonstrated the satisfactory accuracy of the inverse dispersion method when used to quantify sources on terrain where the Monin-Obukhov similarity theory (MOST) is applicable (i.e. flat, open areas where air flow is not disturbed by any major obstacles). Based on their experiments, Flesch & Wilson (2004). made several suggestions for the measurement of concentration, in order to obtain the best estimate of Q:

- Line-averaged concentration measurements across the plume are preferable to point measurements.

- Concentration measurements near the edge of the tracer plume should be avoided; the concentration detector should not be placed immediately above or downwind of the source.

- Distance of the detector from the source should be small enough that the concentration rise over background is accurately measured.

- The period over which time averaging is performed should match normal micrometeorological averaging intervals, viz. typically 10 - 60 min.

- Periods of extreme atmospheric stratification and periods of very light winds (low friction velocity, u_*) should be avoided.

In several respects the experimental regime of the Indian Head experiments differed from the situation treated by Flesch & Wilson (2004). using inverse dispersion. Flesch & Wilson (2004). addressed the emission of *gases* (and more specifically – although the detail does not matter – methane, CH_4). Although gravel dust particles are very small, the density of gravel ($1522\,\mathrm{kg\,m^{-3}}$) is three orders of magnitude larger than that of air ($\approx 1\,\mathrm{kg\,m^{-3}}$), and due to particle inertia (and related gravitational settling) trajectories of airborne solids differ systematically from those of gaseous "particles" (or "fluid elements"). Solid particles are liable to be deposited to ground due to their negative buoyancy, while a more subtle complication is that velocity auto-correlation along the trajectory traced by a heavy particle differs from the (by definition, "Lagrangian") velocity auto-correlation along the path of a fluid element.

A second complication (relative to the simpler regimes treated by Flesch & Wilson 2004) is that it is unclear whether the emission rate (or injection rate) of dust particles from the gravel road was uniform, either in time (i.e. the same from pass to pass at any given N-S location y) or in space (i.e. the same at the two points upwind of the sheltered and reference transects). The vehicle always traveled at a speed of about $80\,\mathrm{km\,hr^{-1}}$, so one might hope that so long as the prevailing wind did not vary (i.e. similar meteorological conditions), it should disturb a similar amount of dust every time it passed a given (y) location on the road. However, dust particles on the gravel road are certainly heterogenous in size. The question is whether the lifted dust plume always carried the same relative proportions of component dust particles upon each vehicle pass, i.e. was the size-discriminated source strength (Q_k) equal from pass to pass, and from point to point?

Regarding the first point, following Wilson (2000) for LS simulations of the Indian Head experiments dust particles were modeled as if each were a "settling sticky fluid element," which is to say that a constant settling velocity w_g (appropriate to the particle density and size, i.e. computed using Equation 2.8) was superposed on the random (turbulent) vertical velocity (see Equation 3.3), and trajectories were terminated whenever and wherever they descended below height $z = z_0$.

As for the question of the uniformity of the source strength, the following approach has been taken. A size discriminated source strength Q_k, regarded as a plausible first approximation, has been inferred from measured (size discriminated) concentration $\overline{c}_k$ at a single location. That source strength has been *assumed* to apply at all points along the road, and theoretical values of $\overline{c}_k/Q_k$ given by the LS model have been un-scaled to provide theoretical values for the size discriminated concentration at all other measurement locations. By comparing these inferred theoretical concentrations with the measured concentration, I address the objectives listed in the beginning of this Chapter, i.e. 1) deduce the effects of the windbreak on dust dispersion, and 2) justify the Lagrangian stochastic model developed for the project.

5.1.2 Inferring size-specific source strength

Which concentration measurement location should best be chosen to infer the source strength? As noted above, a location in the unsheltered area (where MOST applies) is preferable, and measurements near the edge of the plume should be avoided (it should be clear that in principle, confidence limits on theoretical ratios $\overline{c}_k/Q_k$ must be wider for locations in the more complex, i.e. disturbed, shelter flow). Therefore, I focused on the reference transect and eliminated from further consideration the measurements at the higher level ($z = 12\,\mathrm{m}$), which might lie near the edge of the dust plume. A further consideration was that the location of the concentration detector should not be too far from the source, and accordingly I chose the location on the reference transect standing closest to the road, i.e. the measurement location whose coordinates are $(0.75,\ 0.2)_{\mathrm{ref}}$. Note that although a background dust concentration was not measured, it is reasonable to assume $c_b = 0$ because there was no significant injection of gravel dust particles into the atmosphere in the upwind fields. The only significant source was the gravel road, and that, only upon its disturbance by the fast moving vehicle.

Table 5.1 summarizes the measured data and the LS model predictions from which size-segregated source strengths have been computed using Equation 5.1, with an emphasis on particles with diameters less than 10 μm, which were the most abundant in the field. Figure 5.1 shows the (apparent, i.e. inferred) size-segregated source strength versus diameter.

$D_k(\mu\mathrm{m})$	$(\frac{\bar{c}_k}{Q_k})_{mod}(0.75, 0.2)_{\mathrm{ref}}$	$\bar{c}_{k,exp}(0.75, 0.2)_{\mathrm{ref}}$		Q_k	
		Jul 27th	Aug 23rd	Jul 27th	Aug 23rd
4	8.2E-03	2.0E-04	1.0E-04	1.5E-02	2.3E-02
5	7.3E-03	7.1E-03	7.9E-03	1.1E+00	9.7E-01
6	8.5E-03	1.3E-02	1.4E-02	1.6E+00	1.5E+00
7	8.3E-03	7.9E-03	9.2E-03	1.1E+00	9.5E-01
8	9.4E-03	5.3E-03	6.0E-03	6.4E-01	5.7E-01
9	8.3E-03	3.5E-03	3.6E-03	4.3E-01	4.2E-01
10	9.2E-03	2.1E-03	1.9E-03	2.1E-01	2.3E-01
20	7.6E-03	9.0E-04	5.0E-04	6.6E-02	1.2E-01

Table 5.1: Source strength $Q_k(\,\mathrm{mg\,m^{-1}\,s^{-1}})$ for different particle sizes (k), inferred from the experiments of Jul 27 and Aug 23. Q_k has been deduced from the measured (size-discriminated) concentration at $(0.75, 0.2)_{\mathrm{ref}}$ along the reference transect, together with the theoretical value $(\bar{c}_k/Q_k)_{mod}$ for that location from the LS model (computed assuming neutral stratification).

The shape of the size distribution of Q_k can be expected to be similar to the shape of the size distribution of measured concentration (shown in Figure 2.22) because for small particles the model values of (normalized) size-segregated concentration $(\bar{c}_k/Q_k)_{mod}$ at a given downwind location do not greatly vary with size; in other words, for a given downwind location, larger source strength (for given particle size k) corresponds to larger concentration $\bar{c}_k$, and vice versa.

The uncertainty bounds on the inferred source strength Q_k dis-

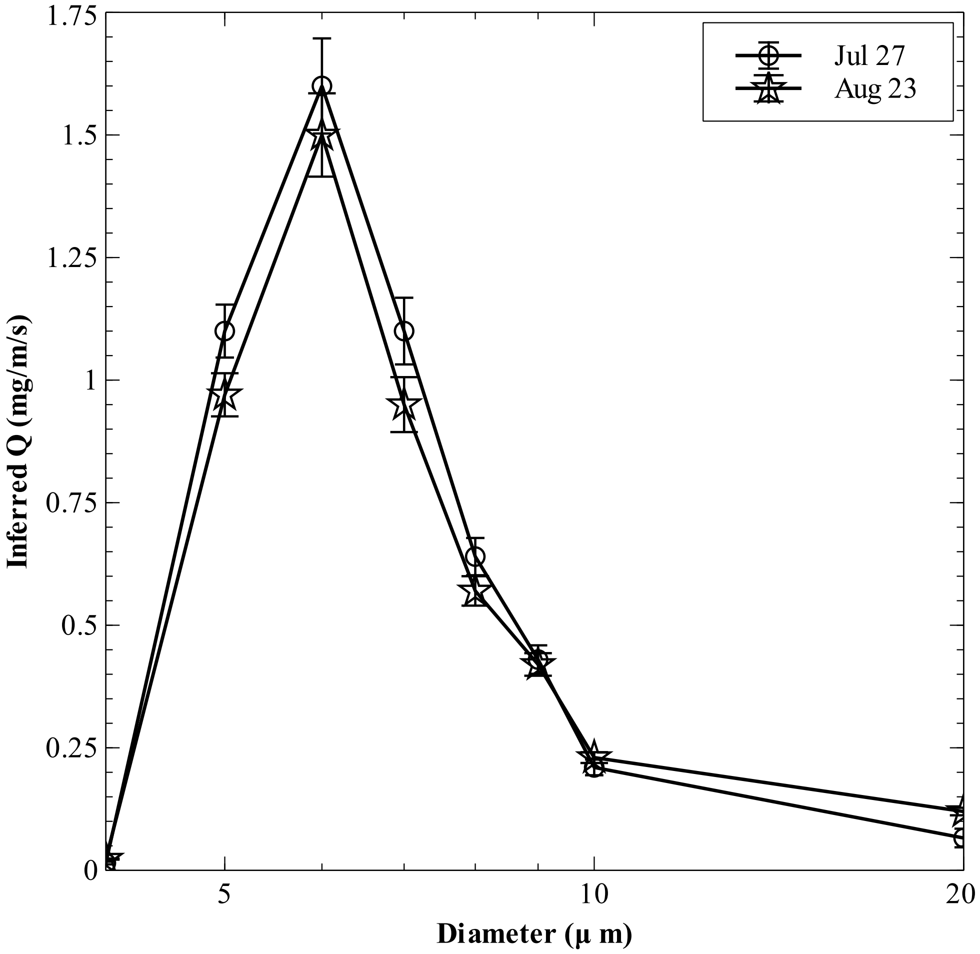

Figure 5.1: Inferred source strength Q_k vs. particle diameter, based on Table 5.1.; error bars are calculated using Equation (5.2)

played on Figure 5.1 have been computed by combining the stochastic uncertainty in the theoretical values $(\frac{\overline{c}_k}{Q_k})_{mod}(0.75, 0.2)_{\text{ref}}$ supplied by the LS model, evaluated as the standard deviation over the 15 sub-ensembles of each run, with the uncertainty in the measured concentrations $\overline{c}_{k,exp}(0.75, 0.2)_{\text{ref}}$. Let

$$\begin{aligned} \alpha &= (\frac{\overline{c}_k}{Q_k})_{mod}(0.75, 0.2)_{\text{ref}} \\ \beta &= \overline{c}_{k,exp}(0.75, 0.2)_{\text{ref}} \end{aligned}$$

and let $\delta\alpha$ and $\delta\beta$ designate the absolute uncertainties in each. According to the rule for error propagation, the uncertainty in $\frac{\beta}{\alpha}$ (i.e. $Q_{k(inf)}$ from Equation 5.1) with known $\delta\alpha$ and $\delta\beta$ is

$$\delta Q_{k(Inf)} = |Q_{k(Inf)}|\sqrt{\left(\frac{\delta\alpha}{\alpha}\right)^2 + \left(\frac{\delta\beta}{\beta}\right)^2}. \tag{5.2}$$

Similarly the uncertainty in the inferred source strength for each size class $\delta Q_{K(inf)}$ will propagate to the inferred time average concentration at a chosen downwind location $\overline{c}_k(x/H, z/H)$ as explained in the next section.

5.1.3 Size-specific concentration implied by the LS model

Given the inferred source strength $Q_{k(Inf)}$ and the LS model's $(\overline{c}_k/Q_k)_{mod}$, time average concentration at a downwind location $(x/H,\ z/H)$ along both reference and sheltered transect for a particle size k can be inferred by

$$\overline{c}_k(x/H,\, z/H) = Q_{k(Inf)} \times \left[\frac{\overline{c}_k(x/H,\, z/H)}{Q_k}\right]_{mod}. \tag{5.3}$$

Tables 5.2 and 5.3 document the 40-min time average concentration implied (by the modeled $(\overline{c}_k/Q_k)_{mod}$) according to the size-segregated inferred source strengths $Q_{k(Inf)}$ shown in Table 5.1 for the field experiment of Jul 27th.

	x/H Unsheltered			x/H Sheltered	
D μm	**0.75**	**5**	**10**	**0.75**	**5**
4	1.00E-04	5.37E-05	3.41E-05	1.39E-04	1.17E-04
5	7.90E-03	4.87E-03	3.46E-03	1.22E-02	9.42E-03
6	1.39E-02	7.69E-03	5.40E-03	1.77E-02	1.36E-02
7	9.20E-03	4.77E-03	3.10E-03	1.37E-02	8.09E-03
8	6.00E-03	2.87E-03	1.91E-03	7.09E-03	5.94E-03
9	3.60E-03	2.13E-03	1.30E-03	4.34E-03	4.86E-03
10	1.90E-03	9.71E-04	6.40E-04	2.07E-03	1.88E-03
20	5.00E-04	3.16E-04	1.84E-04	5.99E-04	5.79E-04

Table 5.2: **Jul 27th**: Inferred time mean concentration in $\mathrm{mg\,m^{-3}}$ at $z/H = 0.2$ for selected particle sizes. The windbreak was located at $x = 0$. Dust was released from a gravel road 60 m upwind of the windbreak ($x/H = -6$).

Figure 5.2 compares the inferred time average concentrations $\overline{c}_k$ vs. diameter at locations $(x/H,\, 0.2)_{\mathrm{ref/lee}}$ and $(x/H,\, 1.2)_{\mathrm{ref/lee}}$ for $x/H =$ (0.75, 5, 10) along both sheltered and reference transect with those measured on that day. (Note: Figure 5.1 indicates that inferred source strengths $Q_{k(Inf)}$ do not differ very much between the experiments of Jul 27th and Aug 23rd, so that the implied time average concentrations from Equation 5.3 must also be very similar; thus results for Aug 23 have not been shown here.) The uncertainties in the inferred

	x/H Unsheltered			x/H Sheltered		
D μm	**0.75**	**5**	**10**	**0.75**	**5**	**10**
4	1.46E-05	2.56E-05	2.56E-05	4.27E-05	6.59E-05	5.12E-05
5	1.08E-03	1.84E-03	2.06E-03	4.22E-03	6.38E-03	4.98E-03
6	1.96E-03	3.43E-03	3.27E-03	5.72E-03	8.34E-03	6.38E-03
7	1.33E-03	2.00E-03	2.11E-03	3.77E-03	5.32E-03	5.10E-03
8	6.38E-04	1.09E-03	1.15E-03	2.17E-03	3.64E-03	2.87E-03
9	4.34E-04	9.54E-04	8.24E-04	1.73E-03	2.17E-03	1.65E-03
10	2.68E-04	3.92E-04	4.13E-04	7.02E-04	1.03E-03	9.29E-04
20	5.92E-05	1.12E-04	9.87E-05	1.91E-04	3.03E-04	2.11E-04

Table 5.3: **Jul 27th**: Inferred time mean concentration in $\mathrm{mg\,m^{-3}}$ at $z/H = 1.2$ for selected particle sizes. The windbreak was located at $x = 0$. Dust was released from a gravel road at 60 m upwind of the windbreak ($x/H = -6$).

source strength $Q_{k(inf)}$ (as estimated using Equation 5.2) and in modeled $\frac{\overline{c}_k(x/H,z/H)}{Q_k}$ (taken to be the standard deviation of the modeled c_k/Q_k across the 15 sub-ensembles for each run of the LS model) were combined to obtain an uncertainty in the inferred time averaged concentration $\overline{c}_k$ by following the rule of error propagation for multiplication. Letting

$$\begin{aligned} \alpha &= \frac{\overline{c}_k(x/H,\, z/H)}{Q_k} \, , \\ \beta &= Q_{k(Inf)} \, , \end{aligned}$$

the uncertainties in inferred values of $\overline{c}_{k(Inf)}(x/H,\, z/H)$ (i.e. $\alpha \times \beta$ with known $\delta\alpha$ and $\delta\beta$) can be expressed

$$\delta\overline{c}_{k(Inf)}(x/H,\, z/H) = |\overline{c}_{k(Inf)}(x/H,\, z/H)| \sqrt{\left(\frac{\delta\alpha}{\alpha}\right)^2 + \left(\frac{\delta\beta}{\beta}\right)^2} \, , \quad (5.4)$$

and are shown as error bars in the left panel of Figure 5.2.

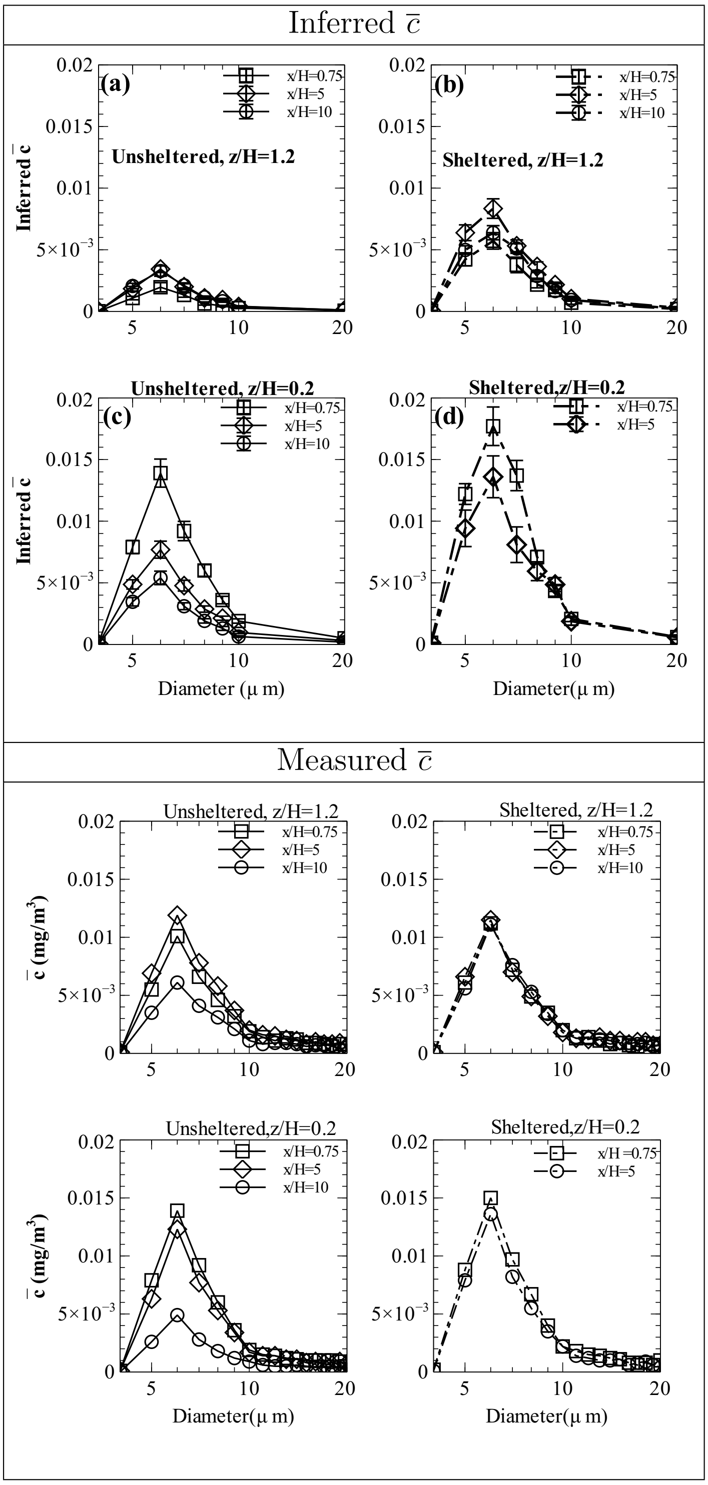

Figure 5.2: Comparison of the size distribution of the inferred time average concentrations with the size-specific time average concentration measured on Jul 27th under effectively neutral stratification.

The pattern of the inferred time average concentrations shows some qualitative similarity with the measured concentration, as described in detail in Section 2.3.2. Time average concentrations peak at particle size $D = 6\,\mu$m. Generally, concentrations in the sheltered area exceed those at corresponding locations on the reference transect, and concentrations at the lower level exceed those at the higher. These features are more accentuated in the inferred than in the measured concentrations. This is probably because inferred concentrations estimated by Equation 5.3 are influenced by modeled $\overline{c}_k(x/H,\, z/H)/Q_k$ shown in Figures (4.6 and 4.7), which reveals distinct differences in modeled $\overline{c}_k/Q_k$ between counterparts in terms of the wind field (homogenous/inhomogenous) and height levels of $z/H = 0.2$ and $z/H = 1.2$.

In addition to the normalized time average concentration, the LS model also provides the ensemble-average transient of normalized, size-segregated concentration, $\langle c_k(t)\rangle/Q_k$. Given also the inferred source strength $Q_{k(inf)}$, one can obtain an ensemble average concentration transient, which can be compared with the measurements from the Casella dust monitors. Because the latter give time series of concentration without size discrimination (i.e. aggregate concentration of all particle sizes), the inferred ensemble-averaged (size-specific) concentration transients at $z/H = 0.2$ shown in Table 5.1 have been aggregated,

$$\langle c\rangle_{mod} = \sum \left(\frac{\langle c\rangle_k}{Q_k}\right)_{mod} \times (Q_k)_{inf}\ .$$

However the particle size range detected by the Rotorods likely does not cover the full range of particle sizes actually present in the field, and the Casella monitors may respond to small dust particles not captured on the Rotorods. Therefore instead of directly comparing $\langle c \rangle_{mod}$ with $\langle c \rangle_{Exp}$ to study their qualitative similarities, I applied the scaling method on modeled $\langle c \rangle_{mod}$ as described in Section 2.2.2, and compared it with scaled $\langle c \rangle_{Exp}$ measured in the field. In short, $U_{\mathrm{ref}} \times \langle c \rangle / c_{\mathrm{ref}}$ is plotted against $U_{\mathrm{ref}} \times t$, where U_{ref} is the simulated wind speed at $(-3,\ 1.2)_{\mathrm{ref}}$ along the reference transect, and c_{ref} is the peak concentration at $(0.75,\ 0.2)_{\mathrm{ref}}$ along the reference transect. The inferred and measured ensemble-averaged concentration transients, scaled by the reference wind speed and concentration, are placed together in Figure 5.3 which shows that there are similarities between the inferred ensemble-averaged concentration transients obtained by the LS model and measurements from Casella monitors.

These similarities are

1. peak concentration decreases with increasing downwind distances, and the peak concentration at a given downwind location arrives later on the sheltered transect than its counterpart on the reference transect;
2. the duration of the dust plume is longer in the sheltered area, and the pattern of peak concentration is more distinct at a location closer to the source. The concentration transient at locations further downwind from the source is wider and weaker, with stronger

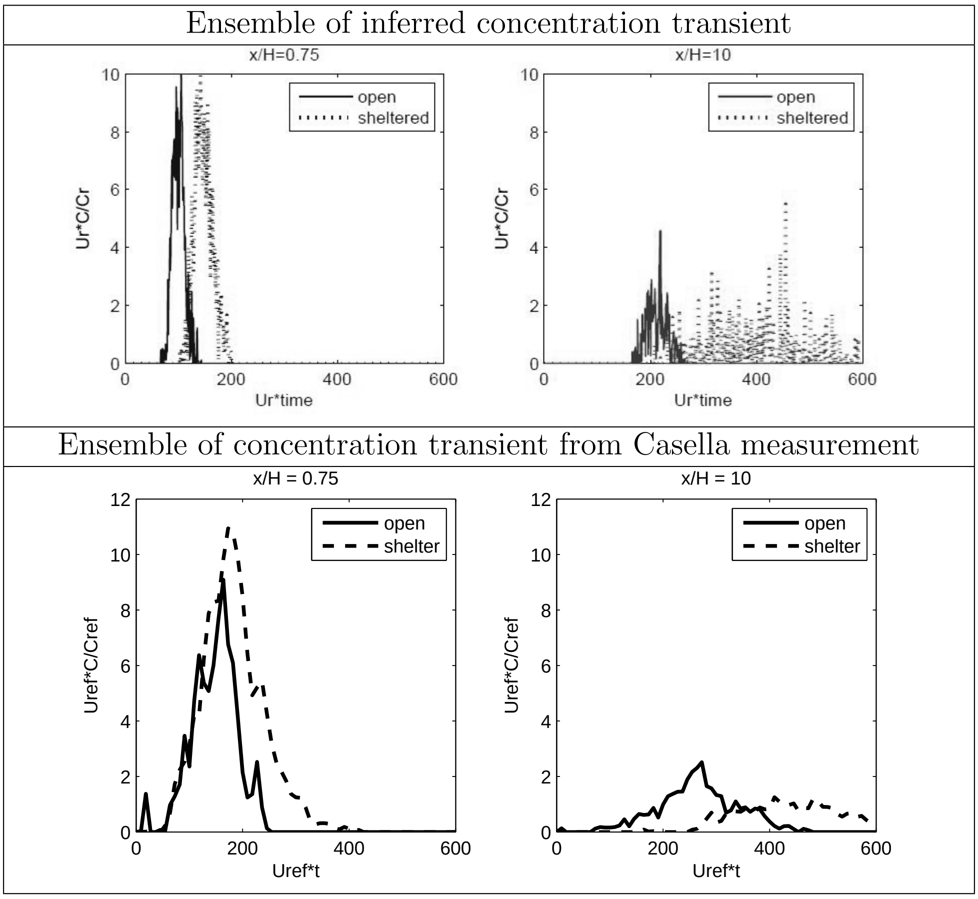

Figure 5.3: Comparing normalized, ensemble-averaged concentration transients inferred from simulations for a neutral atmosphere (upper panel) with those measured by the Casella dust monitors (lower panel). These results are for the experiment of 23rd Aug, with $U_{\mathrm{ref}} = 9.09\,\mathrm{m\,s^{-1}}$.

fluctuations.

However there are some discrepancies between the modeled and measured ensemble mean concentration transients: specifically, peak concentration occurs earlier, and the duration of the ensemble-averaged concentration transient is shorter, for modeled results. It is natural to wonder about the fidelity of the Lagrangian model (i.e. to think about systematic errors lying on the theory side). However two types of random error *in the observations* need to be considered, for they *may* be partly responsible the discrepancies shown by Figure 5.3.

Firstly, there is a sampling uncertainty (or sampling error) associated with the field experiment. The ensemble-averaged concentration transients obtained from the Casella measurements are averaged over 19 realizations (see Equation 2.12), however in the turbulent surface layer an ensemble over (only) nineteen realizations (transients) cannot be expected to provide a sample mean that (with high confidence) closely estimates the underlying (true, but unknown) population mean. In other words, an average over nineteen realizations is not adequate to eliminate the influence of randomness of each individual realization on the calculated ensemble mean. Secondly, and equally importantly, there is a degree of uncertainty regarding the placement (with each ≈ 40 minute long Casella record) of the individual time origins (coresponding to vehicle passage upwind of the transect) of each realization. As described in Section 2.2.2, the driver controlled the time at which the vehicle passed the location directly upwind of the first measurement transect on each pass. Although the driver's watch was manually synchronized with Casella monitors, some uncertainty in time origin of each measurement transect on each pass remains: if this is estimated as ±2 sec then this corresponds to an uncertainty on the $U_{\mathrm{ref}}t$ axis of about ±20 m [*](for the experiment of 23rd Aug, shown in Figure 5.3).

5.2 Fidelity of the modeled results

Quantitatively, how reliable are the inferred concentrations? This is difficult to answer, due to the circular nature of the prediction method — which requires first using measured $\overline{c}_k(0.75, 0.2)_{\mathrm{ref}}$ and modeled $\overline{c}_k(0.75, 0.2)_{\mathrm{ref}}/Q_k$ to infer Q_k, and then using inferred Q_k and modeled $\overline{c}_k(x/H,\, z/H)/Q_k$ to obtain inferred $\overline{c}_k(x/H,\, z/H)$. Fidelity of inferred concentration depends on both the field experiment and on the LS model, both of which are subject to uncertainty: the field data are subject to sampling error (inadequate degree of averaging) and possibly also to systematic errors (e.g. incorrectly controlled Rotorod rotation rate; incorrect assumption regarding particle collection efficiency, etc.), while the LS model certainly oversimplifies the processes it represents. As a working hypothesis, I assume the closer the match of inferred to measured concentration, the more accurate the inferred

---

[*] The uncertainty in time origin for each experiment session can probably be extended to ±5 sec due to changeable circumstances during each experiment session, then locations of experimental dust transients on the $U_{\mathrm{ref}}\,t$ axis are uncertain by ±50 m

concentration — ideally, the two would be equal ($\overline{c}_{Exp} = \overline{c}_{Inf}$). Statistical measures introduced in this section will address the question raised at the beginning of this paragraph.

Figure (5.4) presents scatter plots of inferred $\overline{c}_{Inf}$ vs. measured $\overline{c}_{Exp}$ at downwind locations $(x/H,\ 0.2/1.2)_{\mathrm{ref/lee}}$ for $x/H = (0.75,\ 5,\ 10)$ along both sheltered and reference transect. A simple way to quantify the fidelity of inferred $\overline{c}$ is to measure how well the plotted points are fitted by a 1:1 line. The correlation coefficient

$$R^2 = 1 - \frac{\text{residual sum of squares}}{\text{total sum of squares}}$$

gives the fraction of total variance explained by a linear fit, and measures the quality of the inferred concentrations (the better the fit, the closer the value of R^2 to unity). In addition, the fraction of the modeled concentrations lying within a factor of two of the corresponding observations (FAC2) is also a useful measure of the accuracy of the inferred concentration. Correlation coefficients R^2 and FAC2 scores for subplots (a) through (d) in Figure 5.4 are shown in Table 5.4. The inferred concentrations fail to predict adequately the observed concentrations along $z/H = 1.2$, but the model's fidelity is encouraging for both of the lower ($z/H = 0.2$) transects, i.e. both on the reference (unsheltered) and sheltered transects.

Comparing $(\overline{c}_k)_{mod}$ to $(\overline{c}_k)_{Exp}$ is equivalent to comparing $(\frac{\overline{c}_k}{Q_k})_{mod}$ to measured $(\overline{c}_k)_{Exp}$ normalized by inferred $Q_{k(inf)}$. Let $\hat{\theta}_k = (\frac{\overline{c}_k}{Q_k})_{mod}$, and $\theta_k = \frac{\overline{c}_{k(Exp)}}{Q_{k(Inf)}}$. Tables 5.5 to 5.8 show numerical comparison of $\hat{\theta}_k$ from

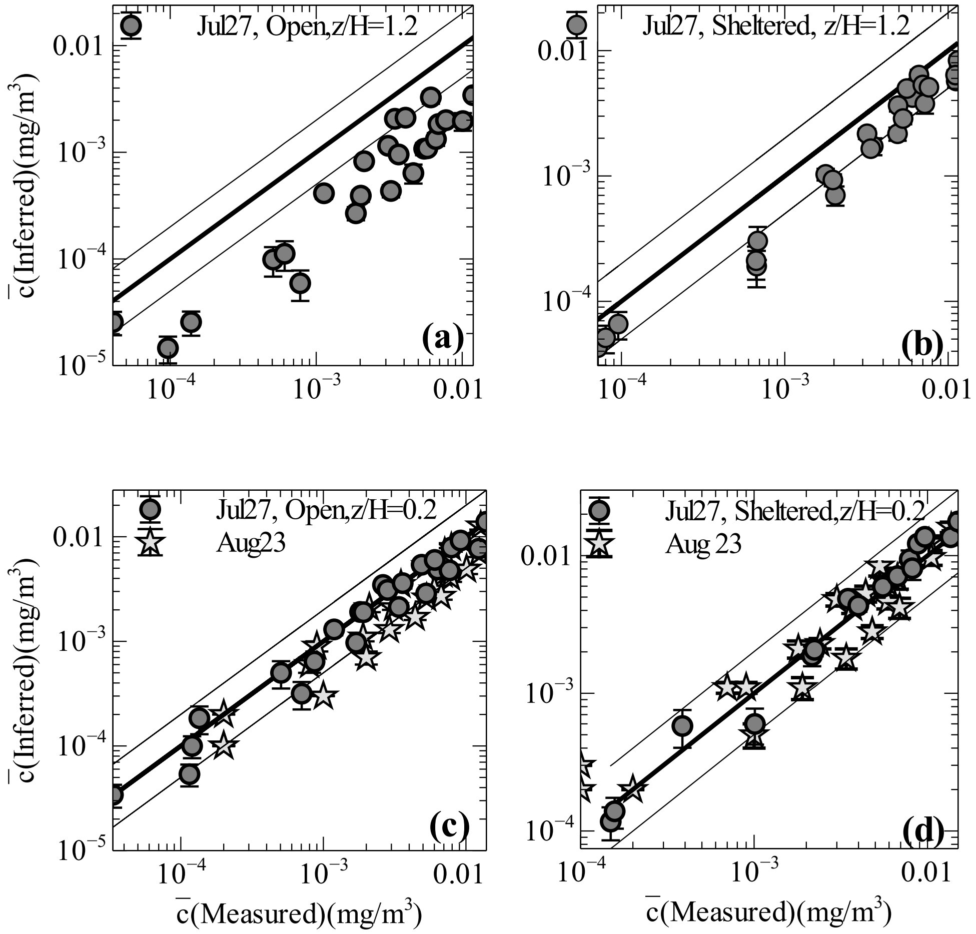

Figure 5.4: Scatter plot of inferred versus measured time average concentrations, for the two field days with neutral stratification (Jul 27 and Aug 23). Upper panels, $z/H = 1.2$ and lower panels $z/H = 0.2$. The thick line is a 1:1 (perfect) fit, while thin lines correspond to ratios (of measured to inferred concentration) equalling 1/2 and 2.

	(a)	(b)	(c)	(d)
Location	$(x/H, 1.2)_{\text{ref}}$	$(x/H, 1.2)_{\text{lee}}$	$(x/H, 0.2)_{\text{ref}}$	$(x/H, 0.2)_{\text{lee}}$
R^2	-13.0	0.20	0.68	0.91
FAC2	0.17	0.67	0.77	1

Table 5.4: Goodness of fit scores for the Lagrangian model at the upper transects (subplots a,b) and at the lower transects (subplots c,d) of Figure 5.4

LS model to θ_k from field observations at all monitoring locations at $z/H = 0.2$ (where the LS model demonstrates better agreement with observation) in the field for selected particles sizes for both field days (Jul 27th and Aug 23rd) under neutral atmospheric conditions.

	$(0.75,\ 0.2)_{\text{ref}}$		$(5,\ 0.2)_{\text{ref}}$		$(10,\ 0.2)_{\text{ref}}$	
D(μm)	$\frac{\overline{c}_{k(Exp)}}{Q_{k(Inf)}}$	$\left(\frac{\overline{c_k}}{Q_k}\right)_{mod}$	$\frac{\overline{c}_{k(Exp)}}{Q_{k(Inf)}}$	$\left(\frac{\overline{c_k}}{Q_k}\right)_{mod}$	$\frac{\overline{c}_{k(Exp)}}{Q_{k(Inf)}}$	$\left(\frac{\overline{c_k}}{Q_k}\right)_{mod}$
4	8.2E-03	8.2E-03	6.8E-03	4.4E-03	0	2.8E-03
5	7.3E-03	7.3E-03	5.8E-03	4.5E-03	2.4E-03	3.2E-03
6	8.5E-03	8.5E-03	7.5E-03	4.7E-03	3.0E-03	3.3E-03
7	8.3E-03	8.3E-03	7.0E-03	4.3E-03	2.5E-03	2.8E-03
8	9.4E-03	9.4E-03	8.3E-03	4.5E-03	2.8E-03	3.0E-03
9	8.3E-03	8.3E-03	7.9E-03	4.9E-03	2.8E-03	3.0E-03
10	9.2E-03	9.2E-03	8.2E-03	4.7E-03	4.4E-03	3.1E-03
20	7.6E-03	7.6E-03	1.1E-02	4.8E-03	1.5E-03	2.8E-03

Table 5.5: **Jul 27th**: $\overline{c}_{kExp}/Q_{kInf}$ and modeled $\overline{c}_k/Q_k$ for several particles sizes at $(0.75,\ 0.2)_{\text{ref}}$, $(5,\ 0.2)_{\text{ref}}$ and $(10,\ 0.2)_{\text{ref}}$ along reference transect

Figure 5.5 shows how θ_k shown as white and black dots at positions (0.75, 0.2), (5, 0.2) and (10, 0.2) along sheltered and reference transect can fit $\hat{\theta}_k$ vs downwind distance (x). Figure 5.5 shows that modeled $(\overline{c}_k/Q_k)_{mod}$ decreases with increasing downwind distance on both the reference and the shelter transect, for selected particle sizes

	$(0.75,\ 0.2)_{\mathrm{lee}}$		$(5,\ 0.2)_{\mathrm{lee}}$	
D(μm)	$\frac{\overline{c}_{k(Exp)}}{Q_{k(Inf)}}$	$(\frac{\overline{c_k}}{Q_k})_{mod}$	$\frac{\overline{c}_{k(Exp)}}{Q_{k(Inf)}}$	$(\frac{\overline{c_k}}{Q_k})_{mod}$
4	1.4E-02	1.1E-02	6.8E-03	9.6E-03
5	8.2E-03	1.1E-02	7.3E-03	8.7E-03
6	9.1E-03	1.1E-02	8.3E-03	8.3E-03
7	8.8E-03	1.2E-02	7.4E-03	7.3E-03
8	1.1E-02	1.1E-02	8.6E-03	9.3E-03
9	9.2E-03	1.0E-02	8.1E-03	1.1E-02
10	1.1E-02	1.0E-02	1.1E-02	9.1E-03
20	1.5E-02	9.1E-03	6.0E-03	8.8E-03

Table 5.6: **Jul 27th**: $\overline{c}_{kExp}/Q_{kInf}$ and modeled $\overline{c}_k/Q_k$ for several particles sizes at $(0.75,\ 0.2)_{\mathrm{lee}}$ and $(5,\ 0.2)_{\mathrm{lee}}$ along the sheltered transect.

	$(0.75, 0.2)_{\mathrm{ref}}$		$(5, 0.2)_{\mathrm{ref}}$		$(10, 0.2)_{\mathrm{ref}}$	
D(μm)	$\frac{\overline{c}_{k(Exp)}}{Q_{k(Inf)}}$	$(\frac{\overline{c_k}}{Q_k})_{mod}$	$\frac{\overline{c}_{k(Exp)}}{Q_{k(Inf)}}$	$(\frac{\overline{c_k}}{Q_k})_{mod}$	$\frac{\overline{c}_{k(Exp)}}{Q_{k(Inf)}}$	$(\frac{\overline{c_k}}{Q_k})_{mod}$
4	8.2E-03	8.2E-03	8.7E-03	4.4E-03	8.7E-03	2.8E-03
5	7.3E-03	7.3E-03	7.1E-03	4.5E-03	6.2E-03	3.2E-03
6	8.5E-03	8.5E-03	8.3E-03	4.7E-03	6.8E-03	3.3E-03
7	8.3E-03	8.3E-03	8.2E-03	4.3E-03	7.1E-03	2.8E-03
8	9.4E-03	9.4E-03	9.4E-03	4.5E-03	7.8E-03	3.0E-03
9	8.3E-03	8.3E-03	7.3E-03	4.9E-03	6.8E-03	3.0E-03
10	9.2E-03	9.2E-03	8.4E-03	4.7E-03	8.8E-03	3.1E-03
20	7.6E-03	7.6E-03	6.7E-03	4.8E-03	8.3E-03	2.8E-03

Table 5.7: **Aug 23rd**: $\overline{c}_{kExp}/Q_{kInf}$ and modeled $\overline{c}_k/Q_k$ for several particles sizes at at $(0.75,\ 0.2)_{\mathrm{ref}}$, $(5,\ 0.2)_{\mathrm{ref}}$ and $(10,\ 0.2)_{\mathrm{ref}}$ along reference transect

	$(0.75, 0.2)_{\mathrm{lee}}$		$(5, 0.2)_{\mathrm{lee}}$		$(10, 0.2)_{\mathrm{lee}}$	
D(μm)	$\frac{\overline{c}_{k(Exp)}}{Q_{k(Inf)}}$	$(\frac{\overline{c_k}}{Q_k})_{mod}$	$\frac{\overline{c}_{k(Exp)}}{Q_{k(Inf)}}$	$(\frac{\overline{c_k}}{Q_k})_{mod}$	$\frac{\overline{c}_{k(Exp)}}{Q_{k(Inf)}}$	$(\frac{\overline{c_k}}{Q_k})_{mod}$
4	4.3E-03	1.1E-02	4.3E-03	9.6E-03	8.7E-03	6.7E-03
5	8.0E-03	1.1E-02	5.5E-03	8.7E-03	6.1E-03	4.7E-03
6	9.2E-03	1.1E-02	6.8E-03	8.3E-03	7.0E-03	6.5E-03
7	8.8E-03	1.2E-02	7.1E-03	7.3E-03	7.3E-03	4.4E-03
8	1.0E-02	1.1E-02	7.8E-03	9.3E-03	8.5E-03	5.0E-03
9	8.7E-03	1.0E-02	7.1E-03	1.1E-02	8.0E-03	4.2E-03
10	1.1E-02	1.0E-02	7.9E-03	9.1E-03	8.4E-03	4.8E-03
20	5.8E-03	9.1E-03	7.5E-03	8.8E-03	8.3E-03	3.8E-03

Table 5.8: **Aug 23rd**: $\overline{c}_{kExp}/Q_{kInf}$ and modeled $\overline{c}_k/Q_k$ for several particles sizes at $(0.75, 0.2)_{\mathrm{lee}}$, $(5, 0.2)_{\mathrm{lee}}$ and $(10, 0.2)_{\mathrm{lee}}$ along the sheltered transect

(small particles, i.e. diameters less than 20 μm); however, the decrease is monotonic on the reference transect whereas there are some sporadic minor increases in $(\overline{c}_k/Q_k)_{mod}$ on the sheltered transect. Moreover, the modeled results show that $(\overline{c}_k/Q_k)_{mod}$ for small particls on the sheltered transect is higher than that on the reference transect for a given distance downwind of the windbreak, which may be attributable to particle lifting induced by the positive vertical wind in the vicinity of the windbreak, and/or the reduced wind speed and less intense vertical mixing in the “quiet zone” (as discussed in Chpater 4).

Table 5.4 shows the goodness of fit of the modeled results with observations, at different monitoring locations, and reveals that goodness of fit is significantly better at the height level $z/H = 0.2$ than at the higher level. Since the LS model was applied to simulate particle trajectories for a range of small particles (i.e. $D \leq 20\,\mu$m), it would be

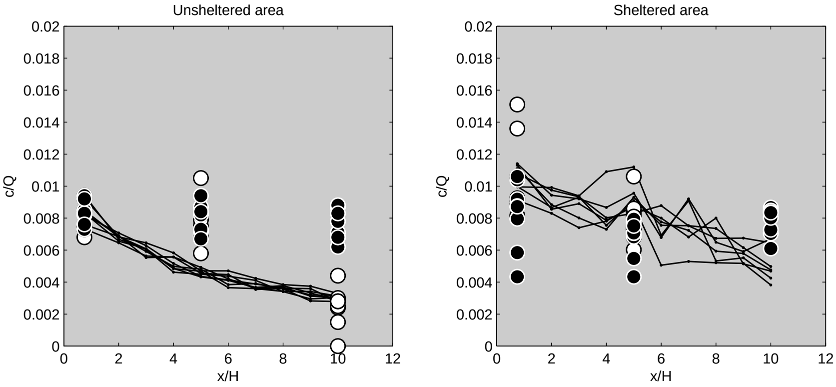

Figure 5.5: Comparison of $(\bar{c}_k/Q_k)_{mod}$ (black lines) to the ratio of $(\bar{c}_k)_{Exp}$ to $Q_{k(Inf)}$ (dots) on the reference (left panel) and sheltered transects (right panel) respectively. White and black dots are for inferred source strength normalized $\bar{c}_{k(Exp)}$ obtained from field day Jul 27th and Aug 23rd respectively.

interesting to know which particle size has the best goodness of fit at $z/H = 0.2$. Given the quality of model fit at $z/H = 0.2$ as shown in Table 5.4, the closeness of $\hat{\theta}_k$ to θ_k for each selected particle size can be compared by calculating the sum of squared residuals (SSR) $\sum\left(\hat{\theta}_k - \theta_k\right)^2$ over all monitoring locations at $z/H = 0.2$, the graphic representation of which is shown in Figure 5.6. The smaller the SSR, the better the modeled results. Figure 5.6 reveals that SSR for particles of 6 micron diameters is smallest. The degree of closeness justified by SSR doesn't differ a lot for small particle sizes except for particles of 4 micron diameters, the SSR of which is about two times as high as SSR of any other particle sizes shown. Notice that generally speaking, particles sizes with higher observed concentration show smaller SSR values implying better goodness of fit of the modeled results, and the lowest SSR is associated with particle size with highest concentration (i.e. peak concentration) observed in the field.

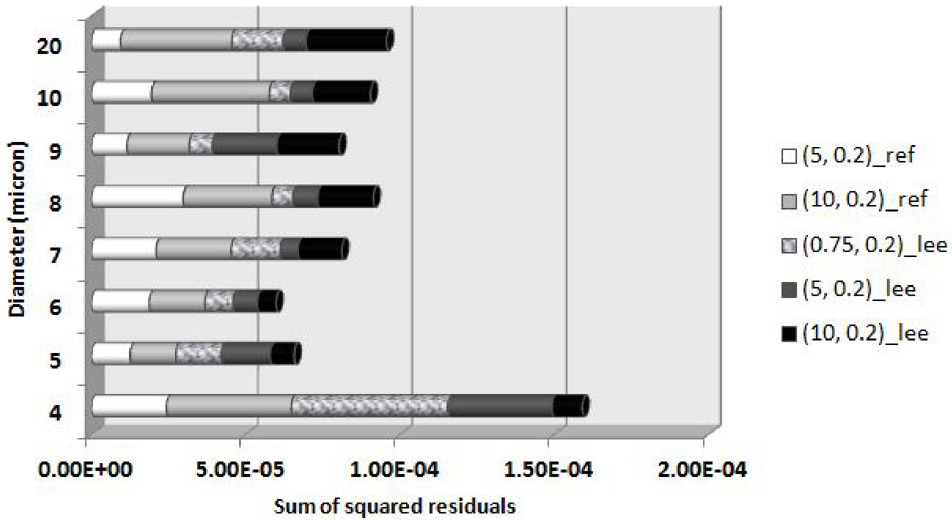

Figure 5.6: Sum of squared residuals to show the closeness of $(\frac{\bar{c}_k}{Q_k})_{mod}$ denoted as $\hat{\theta}_k$) to $\bar{c}_{kExp}/Q_{kInf}$ denoted as θ_k for selected particle classes. Length of different shaded bars indicate the contribution to the overall SSR from $(\hat{\theta}_k - \theta_k)^2$ at the corresponding location shown in the legend.

After statistically justifying the LS model, I noticed that the modeled results show better qualitative agreement with measured results where higher concentration (i.e. more abundant number of particles) was detected in the field. Specifically, $\bar{c}_k$ at $z/H = 0.2$ was significantly higher than that at $z/H = 1.2$, and for particles species of higher concentration detected in the field (e.g. $D = 5, 6\,\mu$m), their corresponding modeled concentrations show greater closeness to measured values. An acceptably low level of random (statistical) error in the LS simulations hinges on the computation of an adequately large number of particle trajectories. The sampling number of imaginary particles for this LS model (i.e., 1000×15) is believed to be sufficient. On the observations side, random error in concentration measurement can only be eliminated by sampling a larger number (or mass) of particles. Where low particle counts or concentrations were detected during the field experiments, the disparity between model and measurement may suggest an insufficient count of sampled dust particles in the field; for example, the 12 m height was too far from the source, and few particles were lifted high enough to reach that level. In the future, in order to improve the quality of the experimental data, one may consider adjusting the height of measurement, i.e., avoid choosing height levels which are too high above the source level.

In short, the pattern of size-specific concentrations inferred from the LS model is qualitatively consistent with the observed pattern. Figures 5.2 and 5.3 compare modeled time average concentration and ensemble-averaged concentration transients to the corresponding observations. Both figures demonstrate that there are similarities between the modeled results and the field observations. Most obviously, time average concentration peaks at $6\,\mu$m diameter. The dust plume progressing along the sheltered transect lags behind that on the reference transect. Time average concentration decreases with increasing downwind distance on a given transect (sheltered or reference). At a given downwind location, instantaneous concentrations reflected by the ensemble average concentration transients in Figure 5.3 first rise until a peak value is achieved, and then drop from the peak to zero. The peak concentration decreases with increasing downwind distance, and the time needed for the passage of the dust plume increases with increasing downwind distance. In addition, model values for normalized concentration $(\overline{c}_k/Q_k)_{mod}$ as a function of downwind distance (as shown by Figure 5.5) demonstrate that at a given downwind location, time average concentration tends to be higher on the sheltered transect.

The goodness of fit of the modeled results to observation (or the fidelity of LS model) can be quantified by calculating the correlation coefficient (R^2) and the fraction of the modeled concentrations lying within a factor of two around the corresponding observations (FAC2) based on the working hypothesis that $\hat{\theta} = \theta$ should be satisfied in an ideal situation, where θ stands for observation in the field, and $\hat{\theta}$ is the same quantity obtained by simulation. Finally, the relative closeness of modeled results to observation can be justified by calculating the sum of squared residuals (SSR). Statistical justification of the LS model (i.e. R^2, scores of FAC2 and SSR) suggests that the modeled results fit measured results significantly better at the lower level ($z/H = 0.2$), and modeled results are relatively closer to the measured results for particles of higher concentration in the field.

Chapter 6

Conclusion

The objective of this project has been to study the effects of a natural windbreak of aspect ratio ($W/H = 0.5$) on dust particle dispersion in the neutral surface layer, an undertaking which required integrating knowledge of atmospheric dispersion with windbreak aerodynamics. Concentration of airborne particulates depends on many factors; observation location relative to the source, particulate source strength, particulate settling velocity, and, the statistics of the ambient wind field are among the most important factors that can affect particle concentration. In general, a windbreak can influence particle concentration in two ways: (1) by filtering particles as they pass through the windbreak, and (2) by disturbing the wind field. In my thesis I have focused my analysis on the case that the atmospheric surface layer is neutrally stratified, and the mean wind direction is perpendicular to the windbreak (and dust source). The complications attending the effects of atmospheric buoyancy and/or a wind striking the windbreak at an oblique angle are considered beyond the reasonable scope of this M.Sc. project.

6.1 Findings

Comparing measurements with simulation, we see that in general time average concentration decreases along the downwind direction for a given source strength. In a horizontally-homogenous wind field, this decrease is caused by spreading of particles induced by turbulence, along with gravitational settling out of the flow (Bouvet et al. 2007). The situation becomes more complicated in the lee of a natural windbreak because both the disturbance to the wind field and the direct action of the foliage in filtering the airstream (i.e. entrapment) can influence the patterns of concentration and deposition of particles. Furthermore the influence of these effects on small particles ($D \leq 20\,\mu$m) differs from that on large particles ($D \geq 50\,\mu$m). Perhaps counterintuitively, according to the results given in this thesis the time average concentration at a downwind location along the sheltered transect tends to be *higher* than its counterpart along the unsheltered transect. The modeled results (i.e. concentration normalized by source strength) show that the increase is more obvious for the time average concentration of small particles (diameters less than $20\,\mu$m) at the higher level ($z = 12\,$m) than that at the lower level ($z = 2\,$m), as indicated by Figures (4.6 - 4.9). The observations also show that measured time average concentration increases in the sheltered area (see Figures 2.20 and 2.21), although the magnitude of the increment is not as evident as that shown in the modeled results. The LS model suggests that concentration for large particles (diameters $D \geq 50\,\mu\mathrm{m}$) doesn't increase (or even tends to decrease) in the sheltered area. This cannot be verified by field observations, since we didn't obtain enough data for large particles during the field experiment.

Field observations combined with modeled results suggest that the wind reduction zone in the lee of a windbreak would cause more dust particles to accumulate in the 'quiet zone', because reduced wind speed and turbulence reduce the intensity of mixing of dust particles with ambient air. As a result, concentration is higher in the wind reduction zone compared to the matching locations along the reference transect. Small particles are more likely to be influenced by the disturbed wind field, and the effect on them of windbreak entrapment is trivial — both the model and the observations show that time average concentration of small particles in the sheltered area tends to be higher than at the matching location in the unsheltered area. On the other hand, the LS model indicates that larger particles are more likely to be deposited to windbreak elements because probability of entrapment increases along with particle size. Since larger particles are prone to be deposited onto ground instead of lingering in the air, windbreak entrapment causes more reduction in deposition rate than in aerial concentration of large particles in the lee of the windbreak.

Both modeled ensemble average concentration transients and Casella measurements (see Figure 5.3) indicate that dust plumes dwell longer in the sheltered area, whereas they pass quickly by locations in the unsheltered area, resulting in a shorter duration of dusty conditions. The model results suggest that all particles, regardless of their size, travel at a similar speed downwind. Specifically, the modeled ensemble mean concentration transients (Figures 4.10 and 4.11) indicate that the peak concentration occurs at a similar time for both small and large particles; in addition, the size distribution of time average concentration (see Figure 5.2) indicates that the relative proportion of dust particles of different sizes within a dust plume doesn't vary with increasing downwind distance.

6.2 Validity of the results

It is difficult to thoroughly justify the validity of the modeled data based on the field experiment in Indian Head, for two reasons. First, the measured data are not sufficient to give a complete picture of the spatial distribution of concentration. Second, one should be aware of the assumptions and simplifications adopted to process experimental data and simulate dust dispersion using the LS model. The LS model developed for this project uses some simple but effective approaches to simulate particle trajectories. First, the LS model follows Thompson's well-mixed condition based on the assumption that the probability density function of velocity statistics is Gaussian, which is generally regarded as a reasonable approximation for weakly-stratified surface layer winds. The approach of parameterizing windbreak entrapment may be oversimplified in that the model assumes impaction conductance is uniform within the natural windbreak; in reality, entrapment efficiency may vary spatially within the windbreak. Zhou et al. (2004) suggest that the internal structures of a windbreak, i.e. vegetative surface area for leaves, branches, trunks and the geometric shape of the individual vegetative elements are all important factors to determine the flow near the windbreak, which may have effects on particle deposition to windbreak elements. However, Asman (2005) pointed that it is not clear at the moment how to parameterize the internal structure of the windbreak using those factors. For the LS model developed for this project, the frontal area density of vegetation elements (specified as $\alpha = 0.5\,\mathrm{m}^2\mathrm{m}^{-3}$) and the characteristic length scale of vegetation elements (specified as $d_e = 0.05\,\mathrm{m}$) are the parameters characterizing the windbreak's internal structure, and their values were obtained not by measurement, but by adopting what seemed a plausible assumption for a natural windbreak. The effects of gravitational settling are treated simply by adding a constant settling velocity to the vertical velocity component and reducing the autocorrelation timescale along the heavy particle trajectory, which is an effective approach to account for trajectories of heavy particles demonstrated by Wilson (2000). The wind statistics used to drive the LS model matched the measured wind speed at (−3, 0.2) along the unsheltered transect; still, there is no way to prove the accuracy of the input wind speed. As stated by Bouvet et al. (2006), who adopted an LS model to study heavy particle deposition in a windbreak flow, the modeled wind speed and turbulence in the sheltered area could be subject to errors as serious as 100%.

With so many assumptions and simplifications adopted by the LS model, it is not surprising that the quantitative agreement of the modeled results with the measured results is mediocre. About 69% of inferred concentrations (including both heights: $z/H = 0.2$ and $z/H = 1.2$ in the unsheltered area and shletred area for Jul 27th and Aug 23) lie within a factor of two (FAC2) of the corresponding measured concentrations (see Fig. 5.4). The FAC2 score is significantly higher for measurements along the lower ($z/H = 0.2$) transect at which higher concentration is expected because of the proximity to source level. In addition, the closeness of modeled results to measurements judged by computing the sum of squared residuals (SSR) indicates that modeled results demonstrate higher accuracy for particle species (in terms of size) with higher concentration detected in the field. This suggests that the LS model is more useful in modeling higher concentration in terms of quantitative quality. Qualitatively, the results are encouraging. Both measured and modeled results indicate that time average concentration of small particles of diameters less than 20μm tends to increase in the wind reduction zone in the lee of the natural windbreak where the duration of the dust plume is prolonged. In short, the results of this research suggest the LS model is a useful tool in terms of giving a reasonable approximation of the dust dispersion pattern observed in the field during the Indian Head experiments.

The question raised in Chapter 1 was — **can a shelterbelt mitigate the downwind concentration of road dust**? The answer, based on this preliminary research, is that a natural windbreak is **not** effective in reducing the concentration of *small* airborne particles (diameter $D \leq 20\,\mu$m); indeed, conversely, the reduced wind speed and turbulence in the near lee of the windbreak can increase the time average concentration of small particles and prolong the dwell time of a transient dust plume. And although windbreak entrapment appears to be a significant mechanism for scrubbing *large* dust particles ($D \geq 50\,\mu$m) from the air, enhancing the action of gravitational deposition, the fact that the observed dust plumes at Indian Head were composed mostly of small particles implies that, at least as regards its immediate lee, **a shelterbelt with aspect ratio $W/H = 0.5$ does not mitigate the concentration of road dust**.

It is natural to wonder whether there might be an optimal design for roadside shelterbelts that is most conducive to mitigation of dust. Might it be possible to improve the efficiency of entrapment of small particles (PM_{10}), which account for more than 90% of the number of particles in dust plumes detected in the field? Windbreak entrapment is governed by Equation 3.20, which can be integrated along a trajectory to yield (Raupach et al. 2001)

$$\frac{C_1}{C_0} = \exp\left(-\frac{g_p \alpha S_b}{U}\right) , \tag{6.1}$$

where C_0 is the upwind particle concentration and C_1 is the particle concentration measured at the downwind edge of the windbreak, i.e. concentration in the air which has passed through the windbreak. In Eq. 6.1 α is the frontal area density of the windbreak, g_p is the total conductance for particle deposition (see Section 1.3.2), U is the ambient wind speed, and S_b is the total distance the dust-laden air traverses while passing through the windbreak. S_b must exceed the width W of the windbreak due to turbulence; typically $S_b/W = 1.2$, according to Raupach et al. (2001). Assuming Brownian diffusion can be ignored, g_p/U can be replaced by the impaction efficiency g_{pi}/U and parameterized in terms of the Stokes number (Equations 1.20 and 1.21).

Equation 6.1 suggests that the probability for particles to pass through the windbreak without impaction onto foliage decreases as g_{pi}/U, α and/or S_b increases. S_b can be increased by increasing the width of the windbreak and/or increasing the ambient turbulence in order to increase the amplitude of the meandering trajectories of airborne particles. Therefore, two methods to improve the efficiency of windbreak entrapment suggest themselves:

(1) increase the width of the windbreak by planting more rows of trees;

(2) select tree species which optimize the efficiency of entrapment of target particles, for instance, PM_{10}.

The first method of improving control of dust off roads would appear straightforward, and be easy to achieve. The practicality of the second approach remains questionable, and further research is warranted. From the perspective of Equation 6.1, one should select trees producing a large frontal area density α, i.e. frontal area of foliage elements per unit volume (dense vegetation). Equations 1.20 and 1.21 show that for a given particle size and ambient wind velocity, the impaction efficiency depends on the characteristic length scale of vegetation elements. Figure 6.1 shows that for a windy day ($U = 10\,\mathrm{m\,s^{-1}}$) the impaction efficiency at given particle size approaches a maximum value as the length scale of the vegetation elements approaches zero (which obviously is not feasible). The curves for small particles are concave downwards, and the curvature increases as particle size decreases; therefore, it might be possible to improve impaction efficiency and thus the effectiveness of a shelterbelt for scrubbing dusty air by selecting trees of a type that features very fine foliage. Figure 6.1 shows that if the target particles are PM_{10}, then a foliage dimension in the range 0.5 to 1 cm may be a good choice.

To conclude, it appears possible that one could improve the efficiency of a shelterbelt in scubbing fine particlates from rural road dust. Whether or not the above specific suggestions might be useful in prac-

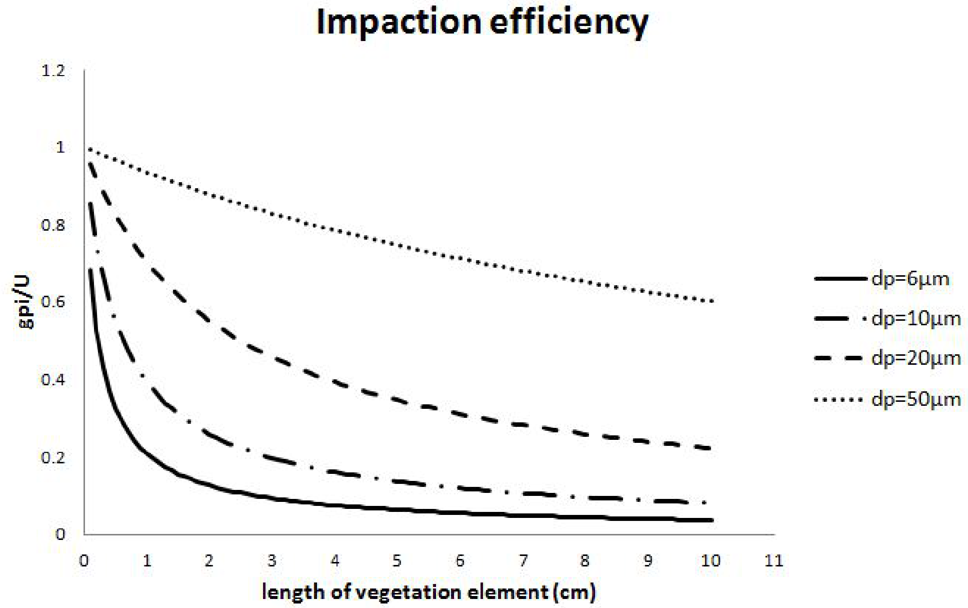

Figure 6.1: Impaction efficiency vs length scale of vegetation element for several particle sizes for the ambient wind speed of $10\,\mathrm{m\,s^{-1}}$ as measured in the field under neutral stratification.

tice is a subject for future researchers.

Bibliography

[Asman 2005] Asman, W.A.H. (2005). Entrapment of ammonia, odour compounds, pesticide sprays and pathogens by shelterbelts. *Technical report*, Danish Institute of Agricultural Sciences, P.O. Box 80, 8830 Tjele, Denmark.

[Aylor 1993] Aylor, D.E. (1993). Relative collection efficiency of Rotorod and Burkard spore smaplers for airborne Venturia inaequalis Ascospores. *Phytopathology.*, **83**, 1116-1119

[Bache 1981] Bache, D.H. (1981). Analysing particulate deposition to plant canopies. *Atmos. Environ.*, **15**, 1759-1761

[Barad 1958] Barad, M.L. (1958). Project Prairie Grass, a Field Program in Diffusion. *Geophys. Res. Pap.*, No. **59**, TR-58-235(II) Air Force Cambridge Research Center

[Bouvet et al. 2006] Bouvet, T., Wilson, J.D., & Tuzet, A. (2006). Observations and modeling of heavy particle deposition in a windbreak flow. *Boundary Layer Meteorol*, **45**, 1332-1349

[Bouvet et al. 2007] Bouvet, T., Loubet, B., Wilson, J.D., & Tuzet, A. (2007). Filtering of windborne particles by a natural windbreak. *J. Appl. Meteorol.*, **123**, 481-509

[Businger et al. 1971] Businger, J.A., Wyngaard, J.C., Izumi, Y., & Bradley, E.F. (1971). Flux-Profile Relationships in the Atmospheric Surface Layer *J. Atmos Sci.*, **28**, 181-189

[Cleugh 1998] Cleugh, H.A. (1998). Effects of windbreaks on airflow, microclimate and crop yields. *J. Agrofor. Syst.*, **41**, 55-84

[Dyer & Bradley 1982] Dyer, A.J., & Bradley, E.F. (1982). An alternative analysis of flux-gradient relationships at the 1976 ITCE. *J. Boundary Layer Meteorol.*, **22**, 3-19

[Flesch & Wilson 2004] Flesch, T.K., & Wilson, J.D. (2004). Deducing Ground-to-Air Emissions from Observed Trace Gas Concentrations: A Field Trial. *J. Appl. Meteorol.*, **43**, 487-502

[Francey & Garratt 1981] Francey, R.J., & Garratt, J.R. (1981). Interpretation of flux-profile observations at ITCE (1976) *J. Appl. Meteorol.*, **20**, 603-618

[Fuchs 1964] Fuchs, N.A. (1964). *The Mechanics of Aerosols.* Pergamon Press, Oxford

[Garratt 1992] Garratt, J.R. (1992). *The Atmospheric Boundary Layer.* Cambridge University Press, 316 pp

[Ghahramani 2005] Ghahramani, S. (2005). *Fundamentals of Probability with Stochastic Processes*. Pearson/Prentice Hall, 654 pp

[Gucker 2005] Gucker, C. (2005). Fraxinus pennsylvanica. In: Fire Effects Information System, [Online]. *U.S. Department of Agriculture, Forest Service, Rocky Mountain Research Station, Fire Sciences Laboratory (Producer).* Available: http://www.fs.fed.us/database/feis/ [2012, October 28].

[Hage 1961] Hage, K.D. (1961). On the dispersion of large particles from a 15-m source in the atmosphere. *J. Meteor.*, **18**, 534539.

[Haugen 1959] Haugen, D.A. (1959). Project Prairie Grass, a Field Program in Diffusion. *Geophys. Res. Pap.*, No. **59**, TR-58-235(III) Air Force Cambridge Research Center

[Israel & Ronsner 1982] Israel, R., & Ronsner, D.E. (1982). Use of a Generalized Stokes Number to Determine the Aerodynamic Capture Efficiency of Non-Stokesian Particles from a Compressible Gas Flow. *J. Aerosol Science and Technology*, **2:1**, 45-51

[Kaimal & Finnigan 1994] Kaimal, J.C., & Finnigan, J.J. (1994). *Atmospheric Boundary Layer Flows.* Oxford University Press, 289 pp

[Kays & Crawford 1980] Kays, W.M., & Crawford, M.E. (1980). *Convective Heat and Mass Transfer.* McGraw-Hill, New York

[Laws & Livesey 1978] Laws, E.M., & Livesey, J.L. (1978). Flow through screens. *Ann. Rev. Fluid Mech.*, **10**, 247-266

[McNaughton 1988] McNaughton, K.G. (1988). Effects of windbreaks on turbulent transport and microclimate. *Agri. Ecosyst. Environ.*, **22/23**, 17-39.

[Monin & Obukhov 1954] Monin, A.S., & Obukhov, A.M. (1954). Basic Laws of Turbulent Mixing in the Ground Layer of the Atmosphere *Trudy Geofiz. Inst. Akad. Nauk SSSR*, **151**, 163-187.

[Oke 1987] Oke, T.R. (1987). *Boundary Layer Climates* (2nd edn.) Methuen and Co. Ltd, London, 435 pp

[Pasquill & Smith 1983] Pasquill, F., & Smith, F.B. (1983). *Atmospheric Diffusion*, (3rd edition). Ellis Horwood, 437 pp

[Paulson 1970] Paulson, C.A. (1970). The Mathematical Representation of Wind Speed and Temperature Profiles in the Unstable Atmospheric Surface Layer. J. *Appl. Meteor.*, **9**, 857-861.

[Peters & Eiden 1992] Peters, K., & Eiden, R. (1992). Modelling the dry deposition velocity of aerosol particles to a spruce forest. *Atmos. Environ.*, **26A**, 2555-2564.

[Rao et al. 1974] Rao, K.S., Wyngaard, J.C., & Cote, O.R. (1974). Local advection of momentum, heat, and moisture in micrometeorology. *Boundary Layer Meteorol*, **7**, 331-348

[Raupach et al. 2001] Raupach, M., Woods, N., Dorr, G., Ley, J., & Cleugh, H. (2001). The entrapment of particles by windbreaks. *Atmos. Environ.*, **35**, 3373-3383

[Sawford & Guest 1988] Sawford, B.L., & Guest, F.M. (1988). Uniqueness and Universality of Lagrangian Stochastic Models of Turbulent Dispersion, Extended abstract, 8th Symposium on Turbulence and Diffusion, April 25-29, San Diego, California. AMS.

[Sawford & Guest 1991] Sawford, B.L., & Guest, F.M. (1991). Lagrangian statistical simulation of the turbulent motion of heavy particle. *Boundary Layer Meteorol*, **54**, 147-166

[Stull 1988] Stull, R.B. (1988). *An Introduction to the Boundary Layer Meteorology.* Kluwer Academic Publishers, 666 pp

[Sullivan 1993] Sullivan, J. (1993). Pinus sylvestris. In: Fire Effects Information System, [Online]. *U.S. Department of Agriculture, Forest Service, Rocky Mountain Research Station, Fire Sciences Laboratory (Producer).* Available: http://www.fs.fed.us/database/feis/ [2012, October 28].

[Taylor 1921] Taylor, G.I. (1921). Diffusion by Continuous Movements. *Proc. London Math. Soc., Ser. 2*, **A20**, 196-211.

[Tennekes 1979] Tennekes, H. (1979). The Exponential Lagrangian Correlation Function and Turbulent Diffusion in the Inertial Subrange, *Atmos. Environ.*, **13**, 1565-1567

[Thomson 1987] Thomson, D.J. (1987). Criteria for the selection of stochastic models of particle trjectories in turbulent flows. *J. Fluid Mech*, **180**, 529-556

[Walker 1965] Walker, E.R. (1965). A particulate diffusion experiment. *J. Appl. Meteor*, **4**, 614621.

[Wang et al. 2001] Wang, H., Takle, E.S., & Shen, J. (2001). Shelterbelts and windbreaks: mathematical modeling and computer simulations of turbulent flows. *J. Wind Eng. Ind. Aerodyn*, **21**, 119-154

[Wilson 1985] Wilson, J.D. (1985). Numerical studies of flow through a windbreak. *J. Wind Eng. Ind. Aerodyn*, **21**, 119-154

[Wilson 2000] Wilson, J.D. (2000). Trajectory models for heavy particles in atmospheric turbulence: Comparison with observation. *J. Appl. Meteorol.*, **39**, 1894-1912

[Wilson 2005] Wilson, J.D. (2005). Deposition of particles to a thin windbreak: The effect of a gap *Atmos. Environ.*, **39**, 5525-5531

[Wilson 2008] Wilson, J.D. (2008). Monin-Obukhov Functions for Standard Deviations of Velocity *Boundary Layer Meteorol*, **129**, 353-369

[Wilson et al. 1981] Wilson, J.D., Thurtell, G., & Kidd, G. (1981). Numerical simulation of particle trajectories in inhomogeneous turbulence. iii. Comparison of predictions with experimental data for the atmospheric surface-layer. *Boundary Layer Meteorol*, **21**, 443-463

[Wilson et al. 2009] Wilson, J.D., Yee, E., Ek, N., & D'Amours, R. (2009). Langrangian simulation of wind transport in the urban environment. *Q. J. R. Meterolog. Soc.*, **135**, 1586-1602

[Wyngaard 2010] Wyngaard, J.C. (2010). *Turbulence in the Atmosphere.* Cambridge University Press, 393 pp

[Zhou et al. 2004] Zhou, X.H., Brandle, J.R., Mize, C.W., & Takle, E.S. (2004). Three-dimensional aerodynamic structure of a tree shelterbelt: Definition, characterization and working models. *Agrofor. Syst.* **63**, 133-147.

Appendix A

Count particles on Rotorods

Image pro plus 7.0 was used to count and classify the number of particles on pictures of sampling areas from a Rotorod spore counter. After properly calibrating the image software with Rotorods' dimensions, for each picture of Rotorods as shown in Figure 2.7, first make it grayscale (see Figure A.1), and then quantify the pixel values of the image to highlight the trapped dust particles (Figure A.2).

Areas of low pixel values can be regarded as dust particles. However, the problem is how to distinguish dust particles from shadows. Generally, all dark areas (pixel value $\in$ [0, 70]) are dust particles, but other areas with low pixel values may represent either dust particles or shadows. One method is to use 'hole ratio' to distinguish them. Hole ratio defines the ratio of object area excluding holes to the total area of the object. Suppose each dust particle is a round sphere, its hole ratio should approach 1; on the other hand, shadows usually surround dust particles, and their pixel values are also low on the grayscale pic-

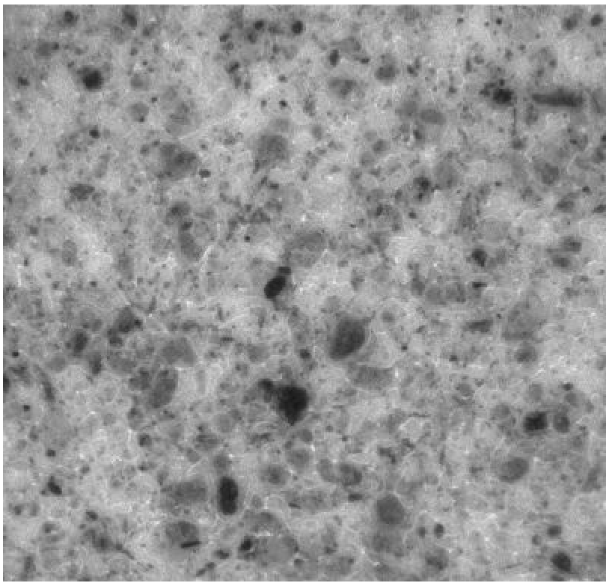

Figure A.1: A grayscale picture of a sampling area from a Rotorod

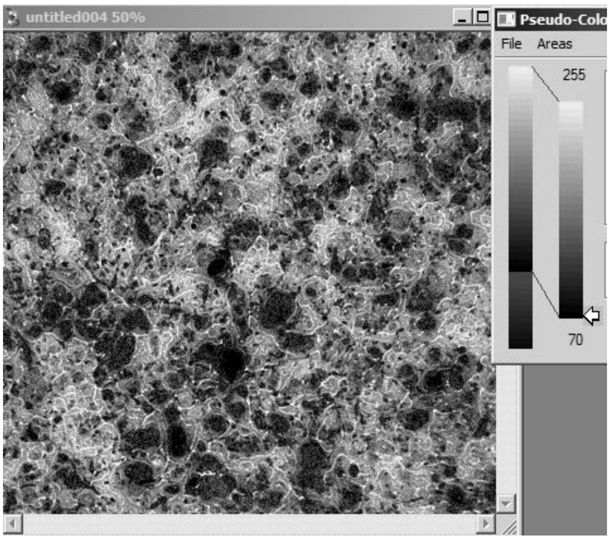

Figure A.2: Quantify the pixel values of the grayscale picture of a sampling area from a Rotorod ture . Dust particles are selected according to the order, pixel value $\in$ [0, 70], pixel value $\in$ [71, 110] and pixel value $\in$ [111, 127] with hole ratios larger than 0.95. Another restriction for selection is the shape of a selected area must not deviate too much from a round object with a uniform radius; specifically, the radius ratio (i.e. ratio between maximum radius and minimum radius) and the roundness defined as $(perimeter^2)/(4\,\pi\,area)$ must be smaller than a threshold value. 5 is chosen arbitrarily for this project. Finally, the diameters of all selected particles are classified into designated size bins from $D = 1\,\mu$m to $100\,\mu$m with equal bin width of $1\,\mu$m. A histogram can show how the number of selected particles is distributed into each size bin. One example is shown in Figure A.3

Systematic errors of Rotorods' counting One way to estimate the systematic error of the number of particles of size k (N_k) counted by Image pro plus for one Rotorod counter is to assume that N_k is a Possion random variable with parameter $\lambda = N_k$. A particle released into the air at the source will either be trapped by the Rotorod or escape the entrapment, which can be regarded as a binomial process. The binomial variable can be regarded as a Poisson variable with $\lambda = np$ when the number of trials is large ($n \to \infty$), the probability of success is small ($p \to 0$), and the average number of successes remains a fixed quantity of moderate value (Ghahramani, 2005). For the field experiment, it is reasonable to assume that each Rotorod only captured

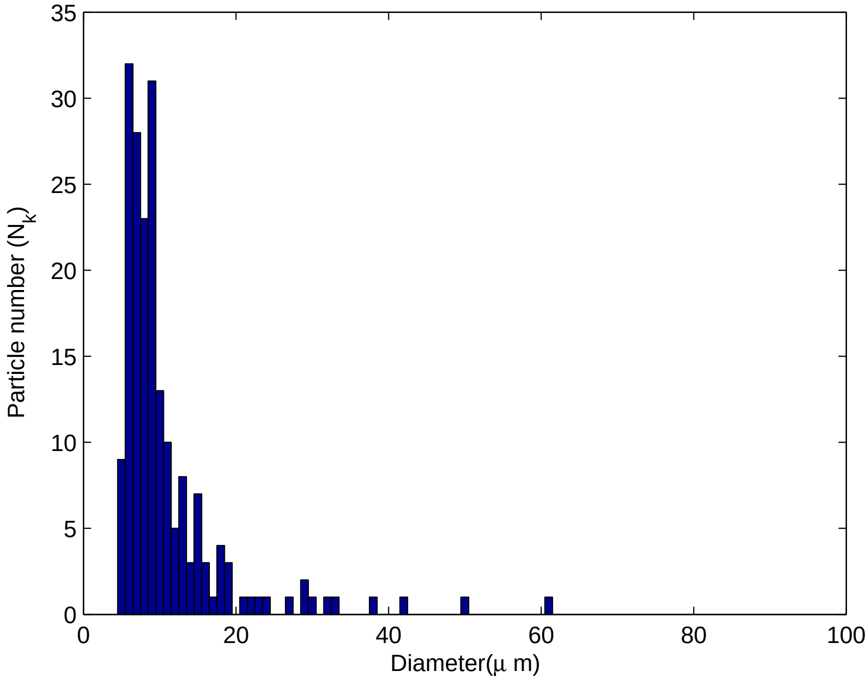

Figure A.3: Distribution of the number of selected particles from a sampling area into size bins.

a small number of dust particles (N_k) comparing to the total number of dust particles(N_{tot}) released at the source, and the probability of success can be approximated by

$$p = \frac{N_k}{N_{tot}};$$

therefore, by the definition of $\lambda = np$, where n can be regarded as N_{tot}, λ can be approximated by N_k. The standard deviation for a Poisson random variable is $\sqrt{\lambda}$, which is $\sqrt{N_k}$ in this case. As a result, the number of dust particles belonging to a size class k can be estimated as

$N_k \pm \sqrt{N_k}$ from counting a Rotorod sample at a measurement location. The error of number of particles for each size calss k captured by the Rotord will be propgated to measured size segregated time average concentration $\overline{c}_k$ at that location as shown by Equation 2.4. I usually omit showing the systematic errors of measurement data in Chapter 2 for simplicity. However, all Rotorod measurements with systematic errors for field days Jul 27th and Aug 23rd are summarized in Figures A.4 and A.5 which show that the number of particles estimated by Image Pro plus for each size bin is converted to number of particles per unit volume (i.e. concentration) by Equation 2.4.

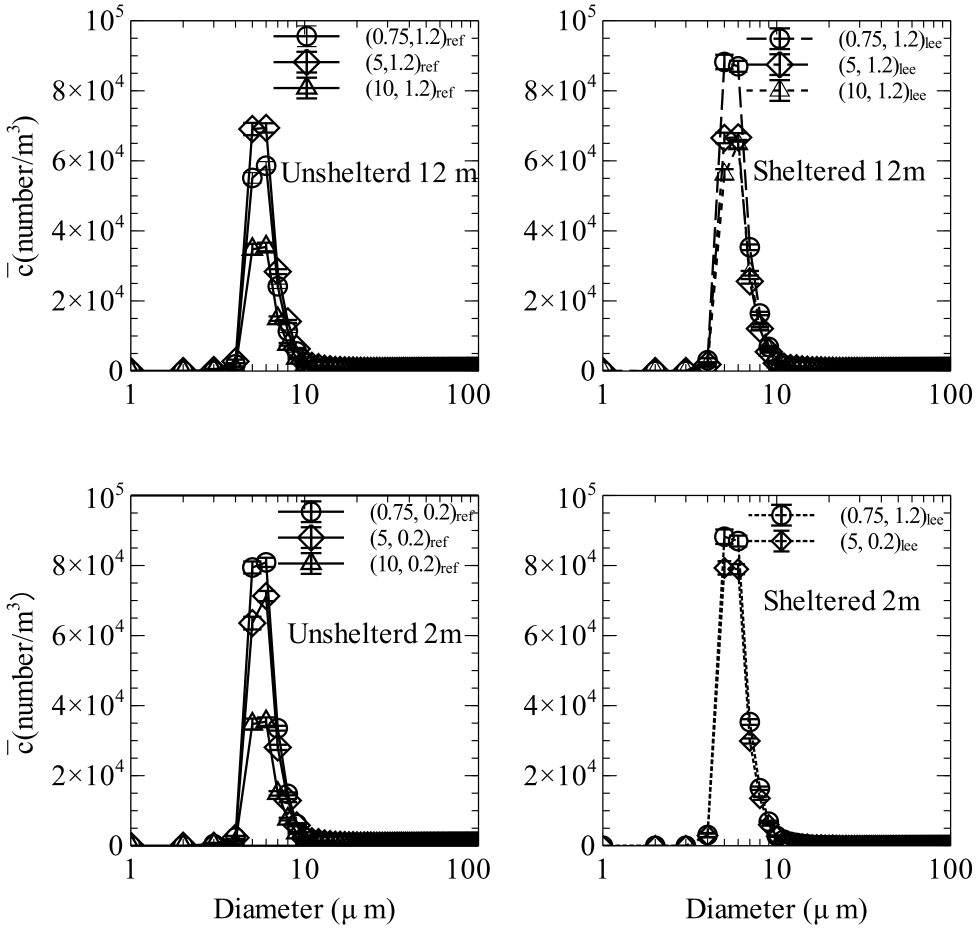

Figure A.4: Jul 27th: Size distribution of concentration (number m^{-3}) with systematic errors for various measurement locations at $z/H = 0.2$ (lower panel) and $z/H = 1.2$ (upper panel).

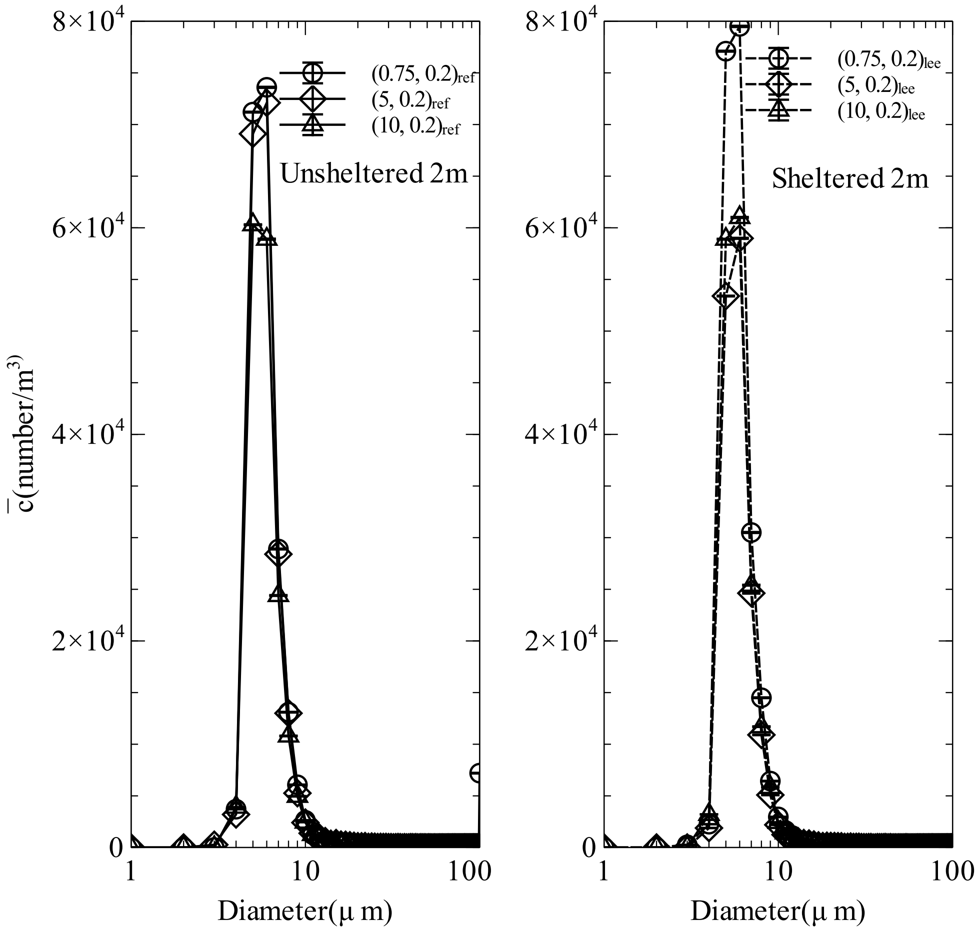

Figure A.5: Aug 23rd: Size distribution of concentration (number m^{-3}) with systematic errors for various measurement locations at $z/H = 0.2$